Measurement of $W + \gamma$ Production in the W to Muon Decay Channel in Proton-Antiproton Collisions at $\sqrt{s} = 1.96$ TeV

March, 2005

Naho Tanimoto

The Graduate School of
Natural Science and Technology
(Doctor Course)
OKAYAMA UNIVERSITY

Measurement of $W + \gamma$ Production in the W to Muon Decay Channel in Proton-Antiproton Collisions at $\sqrt{s} = 1.96$ TeV

March, 2005

51412102 Naho Tanimoto

A dissertation submitted in partial fulfillment of
the requirements for the degree of
Doctor of Science in Physics
in the Graduate School of Natural Science and Technology
of the
OKAYAMA UNIVERSITY, JAPAN

Abstract

The production cross section and the kinematic properties of the decay products of $W\gamma$ in the $W \to \mu\nu$ decay channel from $p\bar{p}$ collisions at $\sqrt{s} = 1.96$ TeV are presented. The measurement use the high p_T muon data from the upgraded Collider Detector at Fermilab(CDF). The data were collected between March 2002 and September 2003. The total integrated luminosities are 192 pb^{-1} with the muon detector which covers the pseudorapidity region of $|\eta| \leq 0.6$ and 175 pb^{-1} with the muon detector covering the region $0.6 \leq |\eta| \leq 1.0$. In the Standard Model the $\mu\nu\gamma$ final states occur due to $W\gamma \to \mu\nu\gamma$ production and via muon Bremsstrahlung, $W \to \mu\nu \to \mu\nu\gamma$. W bosons are selected in their muon decay mode. Additionally, photons with transverse energy above 7 GeV, pseudorapidity in the central region ($|\eta| < 1.1$) and muon-photon angular separation $\Delta R(\mu, \gamma) > 0.7$ are selected. I observe a total of 128 $W\gamma$ candidates, whereas the Standard Model expectation is 142.4±9.5 events. The $W\gamma$ production cross section is found to be

$$\sigma(p\bar{p} \to \mu\nu\gamma) = 16.3 \pm 2.3(\text{stat.}) \pm 1.8(\text{syst.}) \pm 1.2(\text{lum.})[\text{pb}].$$

The theoretical prediction for this cross section is $\sigma(p\bar{p} \to l\nu\gamma) = 19.3 \pm 1.4(\text{th.})[\text{pb}]$. The Standard Model predictions for several kinematic+ variables are compared with data for $E_T^\gamma > 7$ GeV and $\Delta R(\mu, \gamma) > 0.7$. The measured cross section and the photon and W boson production kinematics are found to agree with the Standard Model predictions.

Acknowledgments

The work in this thesis would not have been possible without the valuable guidance and support from my adviser Itsuo Nakano and Reisaburo Tanaka. They got me interested in fundamental physics research. Thanks to them for all the kindness and wisdom they have given me over the years.

I would like to say thank Al Goshaw for his guidance and support. His enthusiasm for the high energy physics, kindness and patience impressed me so much. He asked me the right question at the right time which corrected my trajectory so many times, I was always realized it later. It is a great pleasure working with Beate Heinemann, Michael Kirby and Helen Hayward. We five are great, one of the most active group in the CDF. I am very proud of it.

A special thanks to Taiji Yamanouchi, former Assistant Director in Fermilab. He is the reason why I could keep staying in Fermilab without stepping out. He told me anything I needed, such as basic physics questions, mechanism of the Tevatron accelerators, life in U.S., and even old stories when he was young pioneer of a Japanese physicist. So many things I enjoyed with him as if I was a his daughter. That was a great pleasure for me.

I thank Ulrich Baur for the important contributions to our understanding of theoretical aspects of this analysis. He always supports us with quick and reliable responds.

Many thanks to the CDF Duke group for welcoming me in their group. They gave me a chance to talk in their group meeting as if I was a student of Duke University, and helped me so many times.

I must say many thanks to Isamu Nakamura and Makoto Tomoto. They told me many things not be reluctant to answer my endless questions.

Finally thanks to my family, who have always been there for me.

Contents

List of Tables

List of Figures

Chapter 1

Introduction

The Standard Model (SM) [1–3] is the most successful theory of elementary particles and their interactions we currently have. Its validity has been confirmed in many ways since it was created. For example, one of its biggest triumphs was the prediction, and later experimental observation of the electroweak bosons. It was built by Glashow-Salam-Weinberg as a gauge theory where particles are treated as quanta of fields on which various representations of the gauge group act.

This chapter will briefly describe the Standard Model of Particle Physics. Special emphasis will be placed on the electroweak sector. A discussion of gauge boson self interactions is also included. A review of previous experimental results on trilinear gauge boson couplings is presented. The discussion will be from an experimental point of view rather than a rigorous mathematical one.

1.1 Particles

According to a widely held view in particle physics, there exist two main classes of particles: the *matter constituents*, which include quarks and leptons, and the *interaction quanta*, which include photons and other particles that mediate interactions.

1.1.1 Leptons

Leptons are indivisible particles, devoid of any structure and having in common the property of being completely unaffected by the strong interaction. They all have spin 1/2, obey Fermi-Dirac statistics, and are therefore called *fermions*. A total of six leptons have been experimentally measured; three charged leptons - the electron, the muon and the tau. They differ in the values of their masses. The other three leptons, the *neutrinos*, are all electrically neutral and

Table 1.1: Basic properties of the leptons [7]. The electric charges are given in units of proton charge and the spins are given in units of $\hbar$.

Lepton	Mass	Charge	Spin	Antiparticle
e^-	0.511 MeV/c^2	-1	1/2	e^+
μ^-	105.66 MeV/c^2	-1	1/2	μ^+
τ^-	1776.99 MeV/c^2	-1	1/2	τ^+
ν_e	< 3 eV/c^2	0	1/2	$\bar{\nu_e}$
ν_μ	< 0.19 MeV/c^2	0	1/2	$\bar{\nu_\mu}$
ν_τ	< 18.2 MeV/c^2	0	1/2	$\bar{\nu_\tau}$

have very small mass (See Table 1.1).[1] Every particle has an *antiparticle*. A particle and its associated antiparticle have the same mass, spin, and lifetime. Their electric charge is the same in magnitude but differs in sign. Each charged lepton is associated with a neutrino, the pairs forming three families of leptons: (ν_e, e^-), (ν_μ, μ^-), and (ν_τ, τ^-).

1.1.2 Quarks

Unlike leptons, quarks are not found isolated in nature. They exist bound together with other quarks in objects called hadrons. At present, six different types of quarks are known to exist, called *up* (u), *down* (d), *charm* (c), *strange* (s), *top* (t), and *bottom* (b). They are arranged into three families according to their main modes of interactions: (u, d), (c, s), and (t, b). The quarks, just like the leptons, have spin 1/2 and therefore exist in two spin states, see Table 1.2, but similarities end there. All quarks have a fractional electrical charge: the u, c, and t quarks have a charge of 2/3 while the d, s, and b quarks have a charge of -1/3 (always in units of charge $e > 0$). The corresponding antiquarks have charges of opposite signs, -2/3 for $\bar{\text{u}}$, $\bar{\text{c}}$, and $\bar{\text{t}}$ and 1/3 for $\bar{\text{d}}$, $\bar{\text{s}}$, and $\bar{\text{b}}$.

Table 1.2: Basic properties of the quarks [7]. The electric charge are given in units of proton charge and the spin are given in units $\hbar$.

Quark	Mass	Charge	Spin
u	1.5 - 4.0 MeV/c^2	2/3	1/2
d	4 - 8 MeV/c^2	-1/3	1/2
c	1.15 - 1.35 MeV/c^2	2/3	1/2
s	80 - 130 MeV/c^2	-1/3	1/2
t	174.3 $\pm$ 5.1 GeV/c^2	2/3	1/2
b	4.1 - 4.4 GeV/c^2	-1/3	1/2

[1] There are quite convincing evidences that neutrinos may have small masses reported from Super Kamiokande [4], KamLAND [5], and SNO [6].

1.2 Forces

Table 1.3 summarize the four fundamental forces together with their coupling strengths, ranges, and typical interaction times. Also shown are the masses of the interaction quanta or the particles that carry the forces. The particles are known as the gauge bosons because they have integral spins and their properties are predicted be gauge symmetries The bosons carrying the four fundamental interactions are: the photon (γ) for the electromagnetic force, the $W^{\pm}$ and Z^0 bosons for the weak force, gluons for the strong force and gravitons for transmittion of gravity. The gravitons have spin 2 and have not been experimentally confirmed.

Table 1.3: Fundamental interactions

Interaction	Effective coupling	Boson	Mass [GeV/c^2]	Range [cm]	Typical time [s]
Gravitation	10^{-39}	graviton	0	∞	-
Electromagnetism	1/137	photon	0	∞	10^{-20}
Weak force	10^{-5}	$W^{\pm}$, Z^0	80 - 90	10^{-16}	10^{-10}
Strong force	$\sim$1	gluons	0	$< 10^{-13}$ [a]	10^{-23}

[a] This is the range of the nuclear force, not that of the quark-quark force.

1.3 Electroweak Interaction and QCD

Requiring the Lagrangian to be invariant under local transformations generated by the U(1) group leads to the need for a new interaction field. The force transmitted by this field is the electromagnetic force and the theory is called Quantum Electro Dynamics (QED). This theory is one of the most precisely tested and successful theories in physics. In order to explain the four fermion interaction (Fermi-interaction) in weak decays, a theory based on the groups $\mathrm{SU}(2)_L \times \mathrm{U}(1)_Y$ was developed [1–3, 8–10]. The three bosons arising from the invariance under SU(2) transformations are the W^i_μ bosons, where i =1, 2, 3. The triplet of gauge fields W^i_μ corresponds gauge coupling constants g. $\mathrm{W}^{1,2}$ mix to form the charged W bosons,

$$W^{\pm}_\mu = \frac{1}{\sqrt{2}}(W^1_\mu \mp W^2_\mu), \tag{1.1}$$

that are responsible for weak decays. The remaining W^3 boson does not appear in nature as such. Its superpositions with the boson of the $\mathrm{U}(1)_Y$ group with the gauge field B_μ couples to weak hypercharge with coupling g'. The Z^0 and photon couple to both left- and right-handed fermions and are formed as orthogonal

combinations that give the mass eigenstates for two natural fields

$$Z_\mu = \cos\theta_W W_\mu^3 - \sin\theta_W B_\mu \tag{1.2}$$

$$A_\mu = \sin\theta_W W_\mu^3 + \cos\theta_W B_\mu, \tag{1.3}$$

where $\theta_W (\equiv \tan^{-1}(g'/g))$ is a mixing angle (called Weinberg angle) yet to be determined. The left-handed fermion fields $\psi_i = \begin{pmatrix} \nu_i \\ l_i^- \end{pmatrix}$ and $\begin{pmatrix} u_i \\ d_i' \end{pmatrix}$ of the ith fermion family transform as doublets under SU(2), where $d_i' \equiv \Sigma_j V_{ij} d_j$, and V is the Cabibbo-Kobayashi-Maskawa mixing matrix [11, 12]. As neutrinos have no electric charge, right handed (massless) neutrinos do not take part in any interactions.

The theory describing the strong force, called Quantum Chromodynamics (QCD), is based on the SU(3) group. Quarks have a degree of freedom called *color* that can take three different values. The bosons of the SU(3) group, called gluons, are themselves carriers of color charge. In contrast to electroweak interactions, the strong force gets stronger at on large distance scales. As a consequence, free colored particles can never appear in nature. Quarks form color-neutral objects, either mesons consisting of a quark and an anti-quark (having a color and its anti-color, thus being color neutral) or baryons made out of three quarks (red, blue and green, thus adding up to a color-neutral state). If a $q\bar{q}$ pair is pulled apart, the energy contained in the color-field between the two particles increases linearly with distance. At a given point, the energy of the field exceeds the energy needed to produce a new $q\bar{q}$ pair, and the "string" splits forming two new mesons. In the regime where the coupling parameter of the strong theory is large, perturbation theory cannot be used for calculations and phenomenological models must be used to describe processes like the hadronization of quarks produced in an $e\bar{e}$ or $q\bar{q}$ annihilation. In the limit of small scales or large energies, the strength of the strong force decreases (asymptotic freedom) and perturbative methods can be used to describe the effects of the strong interaction.

1.4 Theory of $W + \gamma$ Production

Many e^+e^- experiments have verified the predictions of electroweak theory using single and pair production of intermediate vector bosons, which may be considered a confirmation of the gauge boson nature. Nevertheless the most direct consequences of the $\mathrm{SU}(2)_L \times \mathrm{U}(1)_Y$ gauge symmetry, a complete experimental survey of the production of non-Abelian self-couplings of the W, Z and γ has not been done. A direct measurement of these vector boson couplings is possible via pair production processes like, $e^+e^- \to W^+W^-$, $Z\gamma$ and $q\bar{q} \to W\gamma$, $Z\gamma$, W^+W^- and WZ. The first and major goal of such experiments will be a confirmation of the SM predictions. A precise and direct measurement of the trilinear and quadratic couplings of the electroweak vector bosons and the demonstration

that they agree with the SM would beautifully corroborate spontaneously broken, non-Abelian gauge theories as the basic theoretical structure describing the fundamental interactions of nature. These interactions are intimately related to the gauge group of the model, and a deviation from the SM would provide important information about a kind of new physics beyond the SM.

The production cross section of $q\bar{q} \to W\gamma$ is the largest among the possible vector boson pair productions in current collider experiment, therefore it can be a crucial test of the Standard Model. The processes that are analyzed in this thesis are

$$p + \bar{p} \to W^{\pm} + \gamma, \quad W^{\pm} \to \mu^{\pm}\nu \tag{1.4}$$

and

$$p + \bar{p} \to W^{\pm} \to \mu^{\pm}\nu\gamma. \tag{1.5}$$

In these processes the virtual and the on-shell W both couple to essentially massless fermions. This together with gauge invariance of the $WW\gamma$ vertex allows the effective Lagrangian [13–15] in terms of four free parameters:

$$\begin{aligned}\mathcal{L}_{WW\gamma} = -ie\big[&(W^{\dagger}_{\mu\nu}W^{\mu}A^{\mu} - W^{\dagger}_{\mu}A^{\nu}W^{\mu\nu}) \\ &+ \kappa W^{\dagger}_{\mu}W_{\nu}F^{\mu\nu} + \frac{\lambda}{M_W^2}W^{\dagger}_{\lambda\mu}W^{\mu}_{\nu}F^{\nu\lambda} \\ &+ \tilde{\kappa}W^{\dagger}_{\mu}W_{\nu}\tilde{F}^{\mu\nu} + \frac{\tilde{\lambda}}{M_W^2}W^{\dagger}_{\lambda}\mu W^{\mu}_{\nu}\tilde{F}^{\nu\lambda}\big]\end{aligned} \tag{1.6}$$

where A^{μ} and W^{μ} are the photon and W^- fields, respectively, $W_{\mu\nu} = \partial_{\mu}W_{\nu} - \partial_{\nu}W_{\mu}$, $F_{\mu\nu} = \partial_{\mu}A_{\nu} - \partial_{\nu}A_{\mu}$, and $\tilde{F}_{\mu\nu} = \frac{1}{2}\epsilon_{\mu\nu\rho\sigma}F^{\rho\sigma}$ where $F_{\mu\nu}$ is the electromagnetic field tensor, e is the charge of the proton, and M_W represents the W boson mass.

The first term in Equation (1.6) arises from minimal coupling of the photon to the $W^{\pm}$ fields and is completely fixed by the charge of the W boson for on shell photons. While the κ and λ terms do not violate any discrete symmetries, $\tilde{\kappa}$ and $\tilde{\lambda}$ terms are P odd and CP violating. Within the Standard Model, at the tree level,

$$\kappa = 1, \quad \lambda = 0, \quad \tilde{\kappa} = 0, \quad \tilde{\lambda} = 0. \tag{1.7}$$

The κ ($\tilde{\kappa}$) and $\lambda(\tilde{\lambda})$ term are related to the magnetic (electric) dipole moment μ_W (d_W) and the electric (magnetic) quadrupole moment Q_W ($\tilde{Q}_W$) of the W^+ :

$$\mu_W = \frac{e}{2M_W}(1 + \kappa + \lambda), \tag{1.8}$$

$$Q_W = -\frac{e}{M_W^2}(\kappa - \lambda), \tag{1.9}$$

$$d_W = \frac{e}{2M_W}(\tilde{\kappa} + \tilde{\lambda}), \tag{1.10}$$

$$\tilde{Q}_W = -\frac{e}{M_W^2}(\tilde{\kappa} - \tilde{\lambda}). \tag{1.11}$$

The variables $\Delta\kappa(=\kappa-1)$, λ, $\tilde{\kappa}$ and $\tilde{\lambda}$ are dimensionless form factors generically written as a_f, where f is a label corresponding to the four anomalous couplings. These momentum dependent variables can be written as [16],

$$a_f(q^2,\bar{q}^2,q_\gamma^2)=\frac{a_{f0}}{(1+\hat{s}/\Lambda_W^2)^n}, \tag{1.12}$$

where a_{f0} is a dimensionless constant (e.g. κ_0-1, λ_0, $\tilde{\kappa_0}$ and $\tilde{\lambda_0}$), $\hat{s}$ is the center of mass energy and Λ_W is the scale of energy where new physics becomes important in the weak boson sector due to a composite structure of the W boson. This form factor $a_f(q^2,\bar{q}^2,q_\gamma^2)$ vanishes when one of the arguments, the square of the four-momentum of one of the W bosons, q^2 or $\bar{q}^2$, or the square of the four-momentum of the photon, q_γ^2, becomes large. For deviations of the three vector boson couplings from the gauge theory value, produced at a scale Λ, one should expect that the form factors stay essentially constant for center of mass energies $\sqrt{s}<\Lambda$ and start decreasing only when the scale Λ is reached or surpassed, very much like the well-known nucleon form factors. Since the energy region covered by the Tevatron is smaller than typically expected for Λ we may assume the form factors $a_f\simeq a_{f0}=\Delta\kappa_0,\lambda_0,\tilde{\kappa_0}$ and $\tilde{\lambda_0}$ to be approximately constant in the followings.

It is possible to relate the anomalous contributions, $\Delta\mathcal{M}_{\beta_\gamma\beta_W}$ (β_γ and β_W are the photon and W helicities [2], respectively), to the $W\gamma$ production amplitudes in terms of the helicity states [16],

$$\Delta\mathcal{M}_{\pm 0}=\frac{e^2}{\sin\theta_W}\frac{\sqrt{\hat{s}}}{2M_W}\left(\Delta\kappa+\lambda\mp i(\tilde{\kappa}+\tilde{\lambda})\right)\frac{1}{2}(1\mp\cos\Theta) \tag{1.13}$$

$$\Delta\mathcal{M}_{\pm\pm}=\frac{e^2}{\sin\theta_W}\frac{1}{2}\left(\frac{\hat{s}}{M_W^2}(\lambda\mp i\tilde{\lambda})+(\Delta\kappa\mp i\tilde{\kappa})\right)\frac{1}{\sqrt{2}}\sin\Theta, \tag{1.14}$$

where Θ denotes the scattering angle of the photon with respect to the quark direction, measured in the $W\gamma$ rest frame, and $\sqrt{\hat{s}}$ is the invariant mass of the W-photon system. Since the structure of the $WW\gamma$ vertex enters Equation (1.4) and (1.5) via the s-channel exchange of a W boson, only the four helicity combinations in Equation (1.13) and (1.14) are affected by anomalous couplings. The helicity combinations $(\beta_\gamma,\beta_W)=(+,-)$ and $(-,+)$ are forbidden by angular momentum conservation because they have the photon and W spins aligned along the photon momentum direction and hence have angular momentum $J\geq 2$.

From Equation (1.13) and (1.14) we can see the several important contributions: the cross section increase the square of the anomalous coupling parameters; the sensitivity to λ_γ will be higher than for $\Delta\kappa_\gamma$, because of the factor $\hat{s}/M_W^2$ multiplying λ_γ in Equation(1.14).

[2] The definition of helicity for a particle is $\beta=(\mathbf{J}\cdot\mathbf{p})/|\mathbf{p}|$.

1.5 Characteristics of $W\gamma$ Events

At the parton level, the reaction $p\bar{p} \to W^{\pm}\gamma$ proceeds via the Feynman graphs shown in Figure 1.1. The first two diagrams of Figure 1.1 (a)(b) are the u-channel and t-channel, respectively, and are associated with initial state radiation from one of the incoming quarks. Figure 1.1(c) represents the s-channel decay and is the most interesting because it contains the trilinear gauge coupling or vector boson self-interaction. Figure 1.1(d) represents final state radiation and is known as radiative W decay.

The $W\gamma$ processes shown in Figure 1.1 are produced with different kinematics. The radiation from initial state radiation diagrams tends to peak along with the initial direction of the quark/antiquark. The final state radiation tends to peak around the decay lepton. However, in contrast to these two processes, the photons from s-channel diagram are not correlated with the incoming quarks or decay lepton. All of these processes produce a photon transverse energy spectrum, E_T^{γ}, sharply peaked at low transverse energy and which falls steeply with increasing E_T^{γ}.

All $W\gamma$ kinematic distributions are sensitive to anomalous couplings, but the most sensitive is the photon transverse energy spectrum with the shape and slope of the spectrum being the steepest for standard model values of the couplings [17]. The photon spectrum for different values of anomalous couplings is shown in Figure 1.2 and it shows that the presence of anomalous couplings will produce an excess of high E_T photons. Limits on the anomalous couplings can be extracted by fitting this spectrum.

Figure 1.3 shows the lepton-photon separation for $W\gamma$ production with different values of anomalous couplings. Radiative events have small lepton-photon separation and little sensitivity to anomalous couplings. Events with larger lepton-photon separation are from s-channel $W\gamma$ production and are more sensitive to anomalous couplings. The presence of anomalous couplings would produce an excess of $W\gamma$ events with a large lepton-photon separation.

The production cross section of $W\gamma$ is sensitive to anomalous couplings as well shown in Figure 1.4.

1.6 Previous Results

There are several experimental approach to test the $WW\gamma$ vertex. One is to measure the cross section times branching ratio for $W\gamma$ production, the other to set limits on the couplings, and finally to look for the radiation amplitude zero [17, 18].

At LEP2, the trilinear gauge boson coupling parameters are measured above the W-pair production threshold using W-pair ($e^+e^- \to W^+W^- \to qqqq$, $qql\nu$, $l^+\nu l^-\bar{\nu}$) [19–41], single W ($e^+e^- \to e\nu W$) [30, 31, 33–41] and single photon

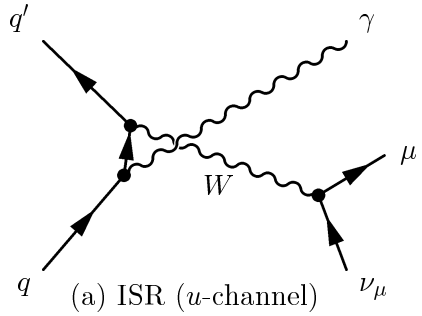

(a) ISR (u-channel)

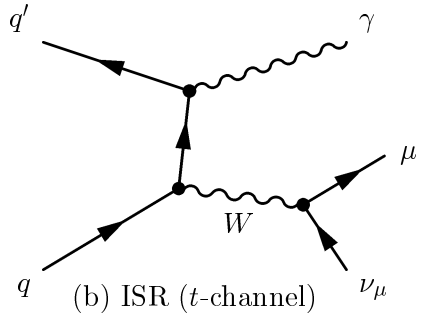

(b) ISR (t-channel)

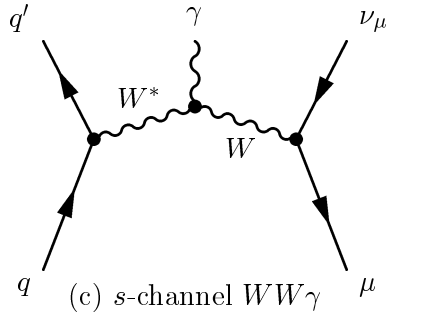

(c) s-channel $WW\gamma$

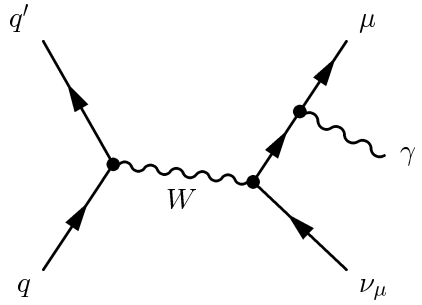

(d) FSR

Figure 1.1: Feynman graphs for the parton level processes contributing to $p\bar{p} \to W\gamma$, $W \to \mu\nu$ and $p\bar{p} \to W \to \mu\nu\gamma$. First two diagrams, (a) and (b), represent initial-state radiation from the incoming quarks. Diagram (c) represents direct $W + \gamma$ production and contains the vector boson self-interaction. Last diagram (d) represents final state radiation or inner bremsstrahlung from the muon and is known as radiative W decay.

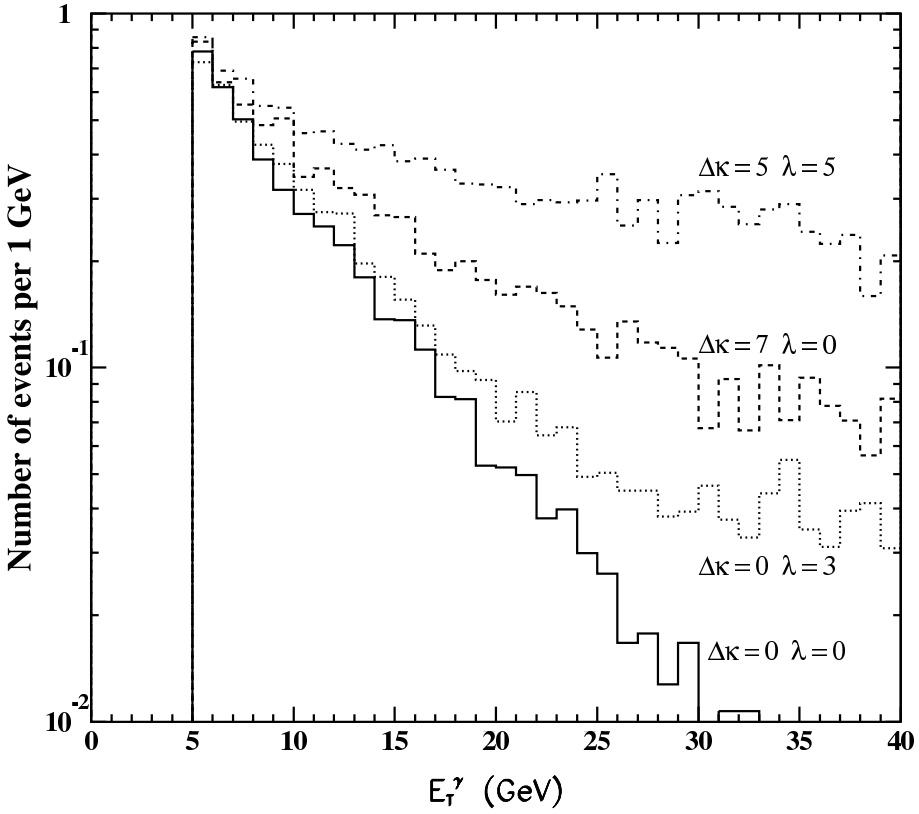

Figure 1.2: The photon E_T spectrum in $W\gamma$ production for different values of anomalous couplings. The shape and slope of the spectrum is steepest for the standard model vales of the anomalous couplings. Any anomalous couplings produce an excess of photons with a high transverse energy.

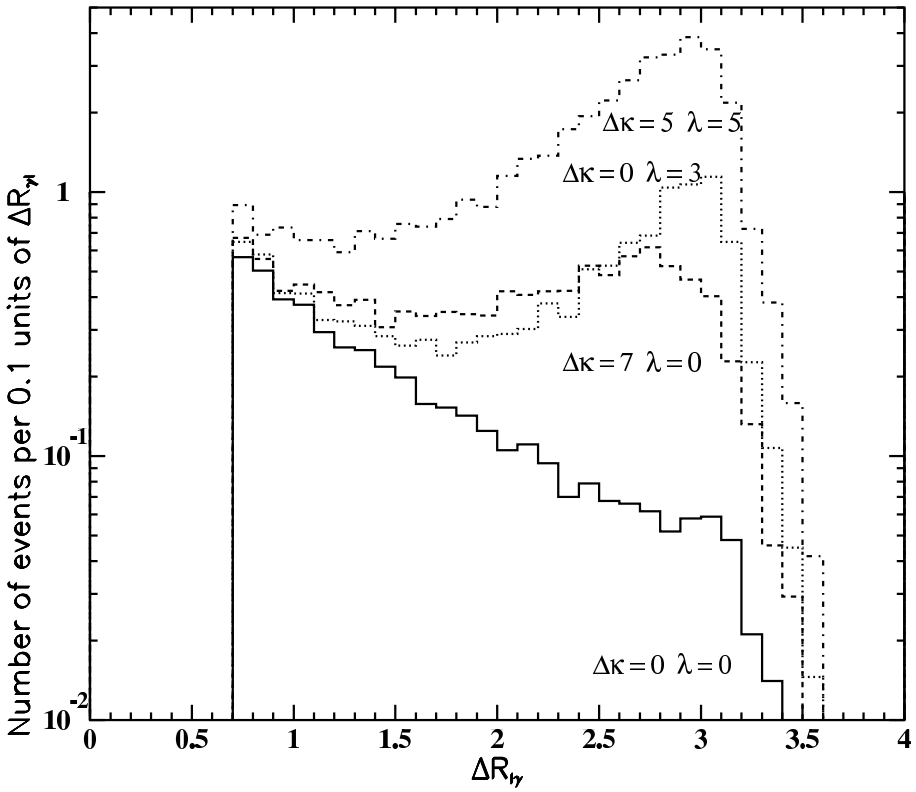

Figure 1.3: The lepton-photon separation in $W\gamma$ production for different values of anomalous couplings. Radiative events populate the smaller lepton-photon region. Any anomalous couplings produce an excess of events with large lepton-photon separation.

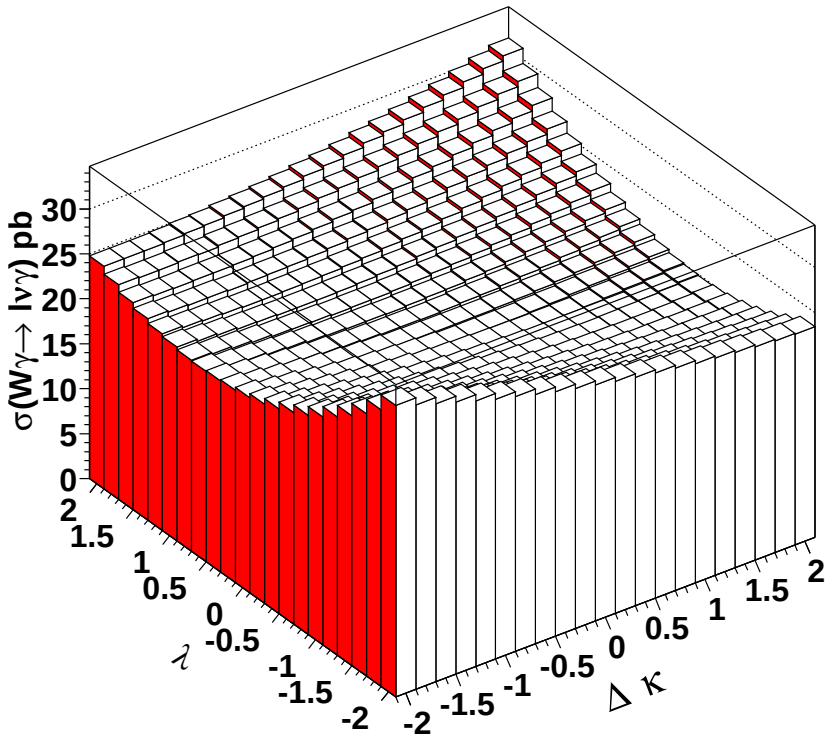

Figure 1.4: The production cross section of $W+\gamma$ for different values of anomalous couplings. $E_T^{\gamma} > 7$ GeV and $\Delta R(l,\nu)$ >0.7 are required. There is a large increase in the cross section away from the Standard Model values of $\Delta\kappa = \lambda = 0$.

Table 1.4: The 95% confidence interval of the trilinear gauge couplings from LEP and Tevatron. In order to extract the value of one TGC the others are generally kept fixed to their SM values.

Experiments	$\Delta\kappa_\gamma$	λ_γ	Δg_1^Z
ALEPH	$0.022^{+0.119}_{-0.115}$	$0.040^{+0.054}_{-0.052}$	$0.023^{+0.059}_{-0.055}$
OPAL	$-0.12^{+0.09}_{-0.08}$	$-0.060^{+0.034}_{-0.033}$	$-0.013^{+0.034}_{-0.033}$
L3	$0.11^{+0.19}_{-0.18} \pm 0.10$	$0.116^{+0.082}_{-0.086} \pm 0.068$	$0.35^{+0.10}_{-0.13} \pm 0.08$
DELPHI	$0.25^{+0.21}_{-0.20} \pm 0.06$	$0.05 \pm 0.09 \pm 0.01$	$-0.02 \pm 0.07 \pm 0.01$
Combined LEP	$-0.009^{+0.022}_{-0.021}$	$-0.016^{+0.042}_{-0.047}$	$-0.016^{+0.021}_{-0.023}$
CDF	$-0.11 < \kappa < 2.27$	$-0.81 < \lambda < 0.84$	
DØ	-0.08 ± 0.34	$0.00^{+0.10}_{-0.09}$	

$(e^+e^- \to \nu\bar{\nu}\gamma)$ [30, 31, 33–41] production.[3] Anomalous TGCs affect the angular distributions of the produced W bosons and their decay products, as well as the total W-pair cross section. They perform two- and three-dimensional fits, where two or all three TGC parameters are allowed to vary in the fits. The results published in 2004 are shown in Table 1.4. Limits on TGCs also exist from studies of di-boson production at the Tevatron with Run I data shown in Table 1.4 [42–47]. CDF has measured the limits on $WW\gamma$ and WWZ couplings using Run Ia data. DØ performed a simultaneous fit to the $W\gamma$, $WW \to$ dilepton, $WW/WZ \to e\nu jj$, $WW/WZ \to \mu\nu jj$, and $WZ \to$ trilepton data samples. DØ has measured the $W\gamma$ production cross section for $E_T^\gamma > 10$ GeV/c and $\Delta R_{l\gamma} > 0.7$ using Run I data. They measured $\sigma(p\bar{p} \to W\gamma) \times BR(W \to l\nu) = 11.8^{+1.7}_{-1.6} \pm 1.6(\text{syst.}) \pm 1.0(\text{lum.})[\text{pb}]$ compared to the Standard Model expectation of 12.5 ± 1.0[pb].

1.7 Outline of the Thesis

The outline of this thesis is as follows. Chapter 2 describes the experimental apparatus, the Tevatron accelerator and CDF detector. The muon channel W event selection including the trigger and event selection are discussed in Chapter 3. Chapter 4 explains central photon identification and $W + \gamma$ event selection. Monte Carlo studies are addressed in Chapter 5. Chapter 6 describes backgrounds to $W + \gamma$ production. The efficiencies and their corrections for muons and photons are summarized in Chapter 7. The results are shown in Chapter 8. Finally, I summarize this analysis in Chapter 9.

[3] The symbol "l" refers to electrons or muons.

Chapter 2

The Experimental Apparatus

The detector used for this analysis is the Collider Detector at Fermilab(CDF) located at the Fermi National Accelerator Laboratory (Fermilab) in Batavia, Illinois(USA). This detector provided data for a general purpose experiment designed to study proton-antiproton collisions at $\sqrt{s}$ =1.96 TeV. The data were collected in March 2002 until September 2003, a period known as Run II. Until the Large Hadron Collider is completed at CERN, the Tevatron is the highest energy collider in the world. In this chapter the Tevatron and CDF are described, and their recent perf-ormance is illustrated.

2.1 The Tevatron Accelerator Chain

The Tevatron is filled with beams of high energy protons and antiprotons in a series of steps shown schematically in Figure 2.1. This process and the chain of accelerators required are outlined below.

2.1.1 Producing and Accelerating Protons

The process of proton acceleration begins as a collection of H^- ions produced by ionizing hydrogen gas [48]. The ions are electrostatically accelerated to a kinetic energy of 750 keV with a Cockcroft-Walton preaccelerator. Subsequently the ion beam is transmitted to a 150 m long linear accelerator (called Linac) consisting of a series of drift tubes [49–52] with radio-frequency (RF) cavities. There H^- are accelerated through AC electromagnetic waves, and as a consequence, the continuous beams are separated into several bunches. A bunch is a collection of particles that are collectively handled by the accelerating, cooling or storing systems. The lengths of the drift tubes gradually increase as the H^- are accelerated, so that the ions are always in the tubes when the direction of the electric field is opposite to the acceleration direction, and they are accelerated only when they are in the gaps between the tubes and the electric field has the forward direction. At the end of the Linac, the H^- beam passes through a carbon

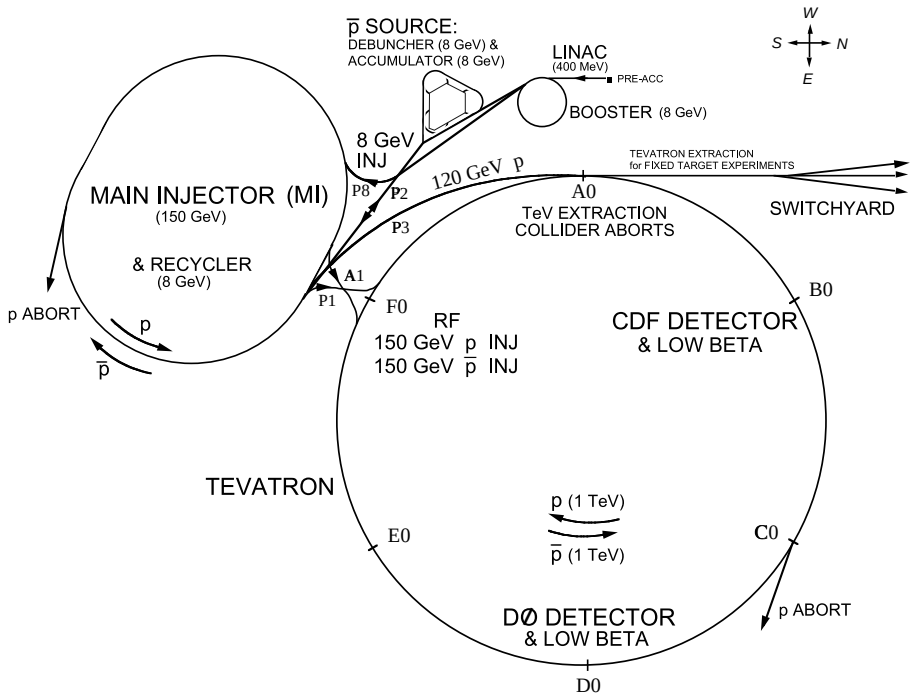

Figure 2.1: A schematic drawing of the Tevatron Accelerator chain at Fermilab.

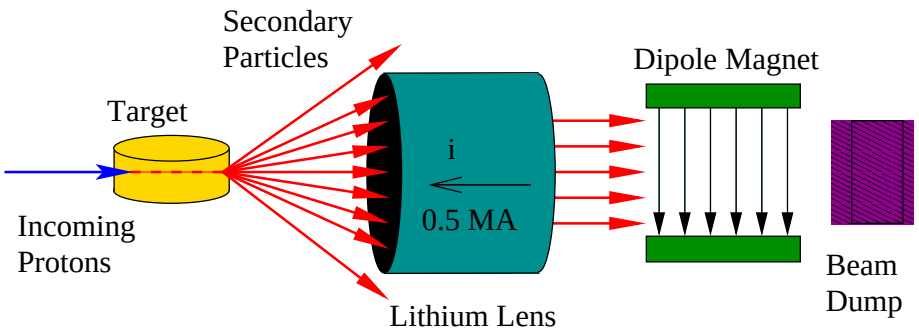

Figure 2.2: Schematic of antiproton production. Antiprotons are produced by the collision of a 120 GeV proton beam with a nickel target. The resulting antiprotons are focused by lithium lens and separated with a pulsed magnet.

foil which removes the electrons leaving bare protons at a kinetic energy of 400 MeV. The energy of the Linac leads to increase proton intensity, and reduces the beam emittance degradation in the Booster accelerator following the Linac and this increases the total intensity of the antiprotons. The Booster [53–55] is an alternating gradient synchrotron with a 475 m circumference, which accelerates the protons to 8 GeV and then directs them into the Main Injector.

2.1.2 Main Injector and Antiproton Production

The main injector is a large synchrotron 3 km in circumference. Its rapid cycling was designed specifically to address the fundamental limitations inherent in the Main Ring used in Run I. The main injector subjects 8 GeV protons to two possible fates: the protons are either accelerated up to an energy of 150 GeV for transfer to the adjacent Tevatron, or their energy is increased to 120 GeV and they are transferred to the antiproton source.

The 120 GeV antiprotons [56] collide with a nickel target, and in these events many secondary particles are produced (Figure 2.2). In approximately one out of every 10^5 collisions, an antiproton is produced. The resulting spray of particles is focused by a cylindrical lithium lens with an 0.5 MA pulsed axial current. The particles are then filtered by a pulsed dipole magnetic spectrometer resulting in an 8 GeV beam of antiprotons.

The beam of antiprotons is directed to the debuncher [57], one of two rounded triangular synchrotrons which make up the antiproton source. The antiprotons are temporarily stored in the accumulator until enough ($\approx 10^{11}$) have been collected to fill the Tevatron. The accumulator uses stochastic cooling [58,59] to reduce the emittance of the beam. Stochastic Cooling is based on the principle of sampling a particle's motion with a pickup and correcting the motion with a kicker. These antiprotons are then bunched and inserted into the Main Injector. They are accelerated to an energy of 150 GeV for insertion into the Tevatron.

2.1.3 The Tevatron

The Tevatron [60] receives 36 proton and 36 antiproton bunches with a minimum spacing of 392 ns at an energy of 150 GeV from the Main Injector (a "shot") and accelerates them to their final energy of 0.98 TeV. The Tevatron is a circular accelerator of about 1 km of radius which collides bunch of protons and antiprotons accelerated to a total center of mass energy of 1.96 TeV. The protons and antiprotons share the same rings but move to opposite direction, the protons travel clockwise and the antiprotons travel counter-clockwise. The protons and antiprotons are bent by superconducting magnets so that they will not collide inside the ring except in two interaction points: $B0$ where the CDF detector is located, and DØ.

Assuming that the proton and antiproton beams collide head-on without a crossing angle and with optimal alignment, the luminosity of the Tevatron can be written as

$$L = \frac{f n_b N_p N_{\bar{p}}}{2\pi\sqrt{\sigma_p^2 + \sigma_{\bar{p}}^2}} F(\frac{\sigma_l}{\beta^*}) \tag{2.1}$$

where f is the revolution frequency, n_b is the number of bunches per beam (36), N_p and $N_{\bar{p}}$ are the number of protons and antiprotons in each bunch respectively, σ_p and $\sigma_{\bar{p}}$ are the proton and antiproton transverse beam sizes at the interaction point, F is a form factor that depends on the length of the bunches (σ_l) and the beta function (β^*) at the interaction point.

The luminosity at the Tevatron is proportional to the product of the phase space density of the proton bunches and the number of antiprotons in the collider for a particular store.[1] The number of events N collected for a process of cross section σ and generated in a time interval ΔT is given by the relation,

$$N = \sigma \int_{\Delta T} L \; dt = \sigma \mathcal{L}. \tag{2.2}$$

The quantity $\mathcal{L}$ is called the "integrated luminosity" and is usually defined for all the period of data collection of the experiment and "instantaneous luminosity" L, which is the luminosity determined by measuring the number of inelastic proton and antiproton interactions per second.

Figure 2.3 shows the integrated luminosity given in units of pb^{-1} from the definition in Equation (2.2). [2]

[1] A store consists of the colliding proton and antiproton particle beams.

[2] The cross sections and luminosities will be given in sub-multiples of barns (b), where 1 b=10^{-28}m^2 = 10^{-24}cm^2.

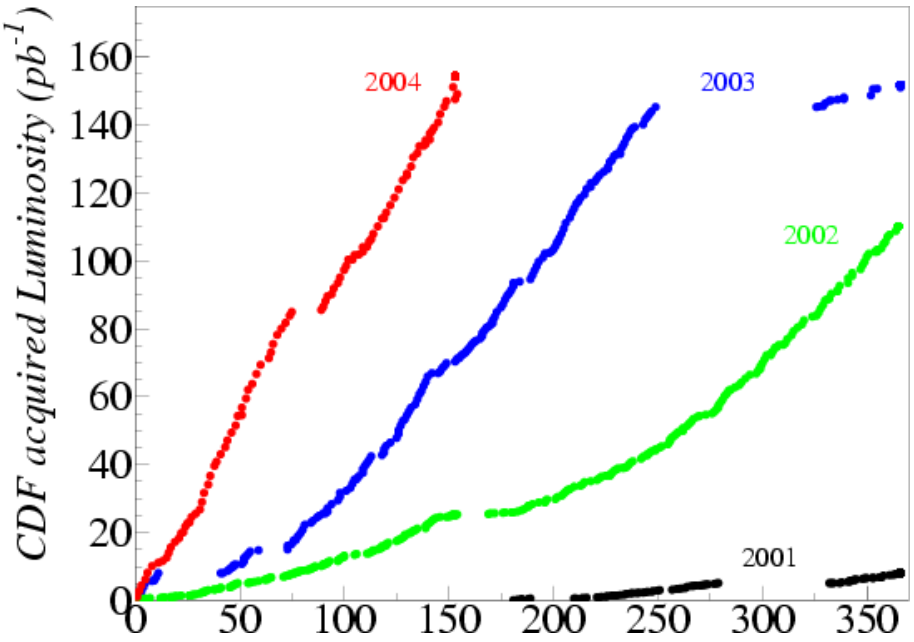

Figure 2.3: Total integrated luminosity effectively recorded on tape by CDF.

2.2 The Collider Detector at Fermilab

The Collider Detector at Fermilab (CDF) is a general purpose detector designed to make precise position, momentum, and energy measurements of particles originating from the proton and antiproton collisions [61]. An elevation view of the detector is illustrated in Figure 2.4, and a cut-away diagram in Figure 2.5. It is cylindrically symmetric around the beam axis and forward-backward symmetric about the interaction region. This section describes the CDF detector, focusing on the systems that were vital to this analysis.

2.2.1 The CDF Coordinate System

In the CDF detector, a right handed coordinate system is used. The z-axis of the detector coincides with the direction of the proton beam and defines the polar angle θ of the laboratory frame. The x-axis is oriented horizontally away from the detector and y-axis is vertical pointing up-wards. The high energy collisions occurring at the center of the detector produce particles that are uniformly distributed in the azimuthal angle ϕ, shown in Figure 2.6.

In $p\bar{p}$ machines one can use the image that two "bags" of elementary particles (quarks, antiquarks and gluons) collide. One is usually interested in events where two of these elementary particles undergo a so-called "hard-scattering" interaction, where their annihilation produces new particles at high transverse momentum. The center of mass system (CMS) of this hard interaction usually

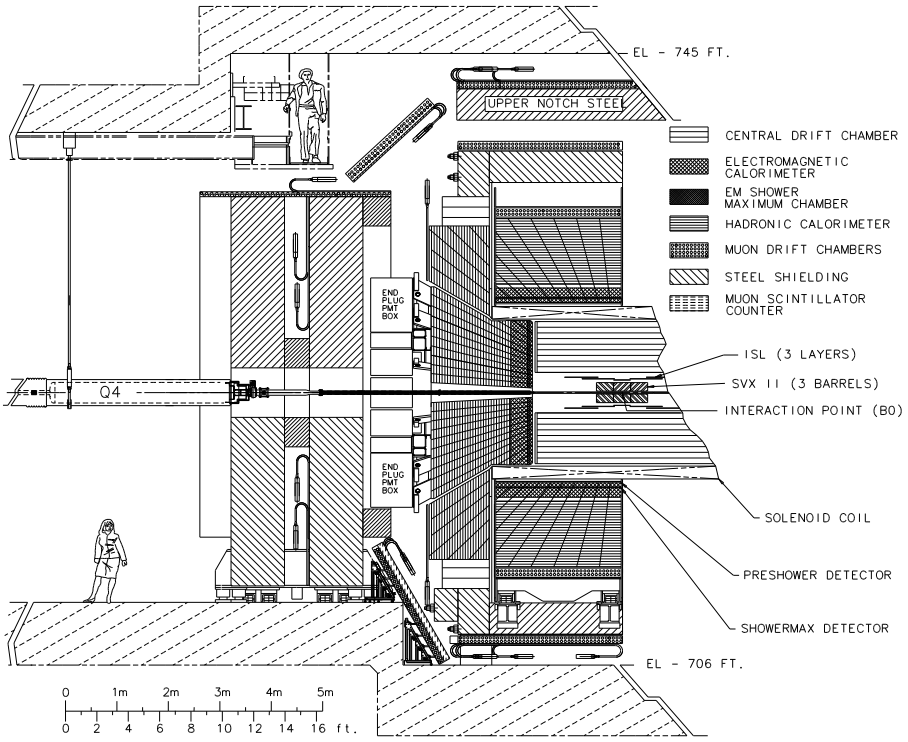

Figure 2.4: Elevation view of one half of the CDF II detector.

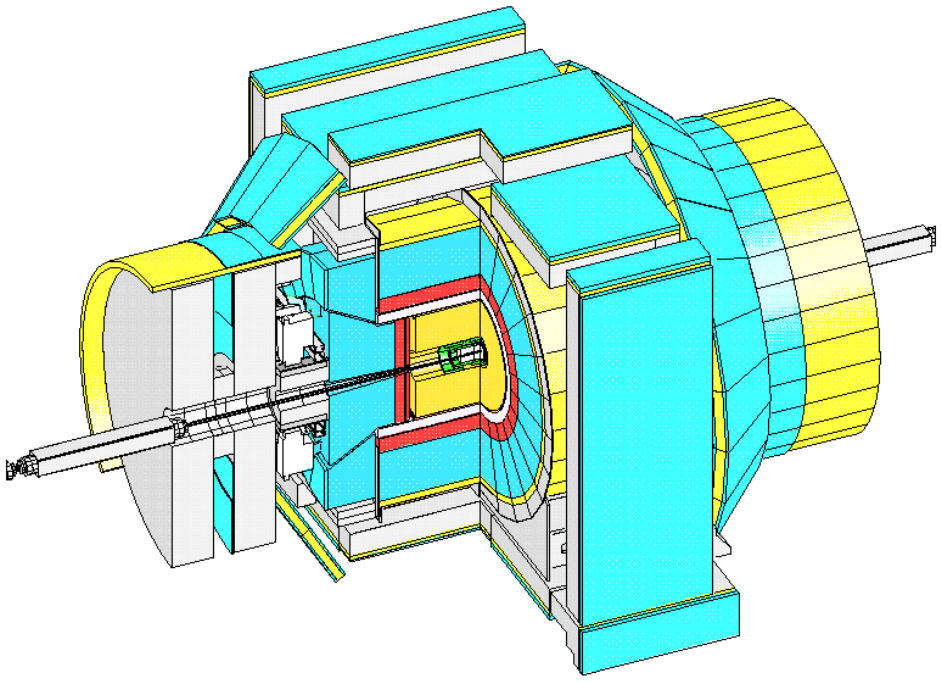

Figure 2.5: Cut away view of the CDF Run II detector.

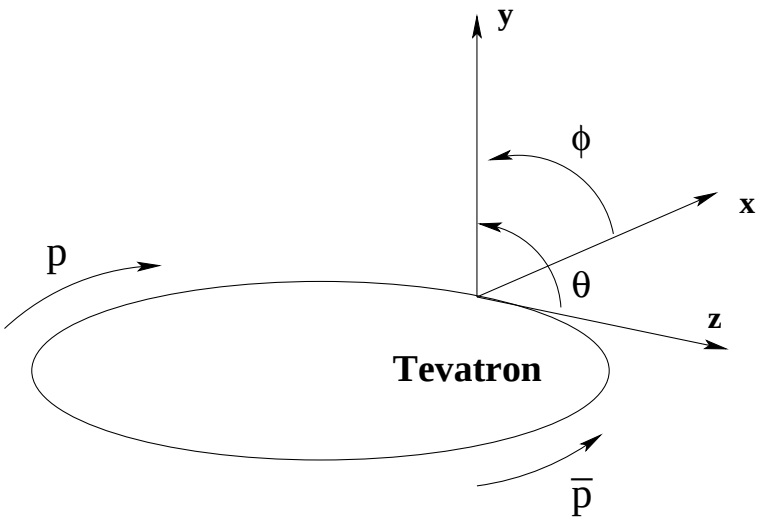

Figure 2.6: Coordinate system used at CDF.

has a boost along the z-axis. Many of the particles produced in the collision, i.e. the remnants of the proton not participating in the hard scattering interaction, escape down the beam pipe. Hence the longitudinal boost of the CMS of the hard scattering partons cannot be measured. The transverse momentum p_T of the particles that escape down the beam pipe is negligible, making it possible to apply the conservation of energy and momentum in the transverse plane. This makes the transverse energy/momentum E_T/p_T ($E\sin\theta/p\sin\theta$) and the missing transverse energy $\not\!\!E_T$, defined as the transverse energy imbalance, extensively used variables for hadron collider physics. The missing transverse energy of this analysis is detailed in Section 3.3.2. It is natural to use the rapidity y at hadron colliders as the multiplicity of high energy particles (dN/dy) is covariant under Lorentz transformation along the z axis. The rapidity of a particle is defined as

$$y \equiv \frac{1}{2}\ln\left(\frac{E+p_z}{E-p_z}\right), \tag{2.3}$$

where E is the energy of the particle and p_z is its longitudinal momentum. For highly boasted particles, where $m/E \to 0$, this can be approximated by pseudorapidity

$$\eta = -\ln\left(\tan\frac{\theta}{2}\right). \tag{2.4}$$

2.2.2 Charged Particle Tracking Systems

Charged particle tracking plays a major role in almost every physics analysis done with the CDF detector. The tracking system in CDF, shown in Figure 2.7, consists of an open cell drift chamber, the Central Outer Tracker(COT), which covers the region $|\eta| < 1$, and the "silicon inner tracker" system, which provides full coverage up to $|\eta| < 2$. These tracking systems are immersed in a magnetic field of 1.4 Tesla, produced by a superconducting solenoid of length 4.8 m and radius 1.5 m. The coils are made of an aluminum-stabled niobium-titanium alloy. The magnetic field enables measurements of charge and momentum via the tracking detectors.

Silicon Detectors

The silicon inner tracker consists of three concentric silicon micro-strip device which provides precise r, ϕ and z tracking information close to the interaction point. The $r-\phi$ view of the silicon detectors are shown in Figure 2.8.

The innermost one, Layer 00 (L00) [62, 63], is a single-sided, radiation-hard silicon layer located at 1.35 cm radius, just outside the beampipe, which is located between the radii of 0.83 and 1.25 cm.

The Silicon Vertex Detector (SVX) [64], placed immediately outside L00 at the radius of 1.6 cm, is composed of three cylindrical barrels with a total length of 96 cm, as shown in Figure 2.9. They extended about 45 cm in the z direction

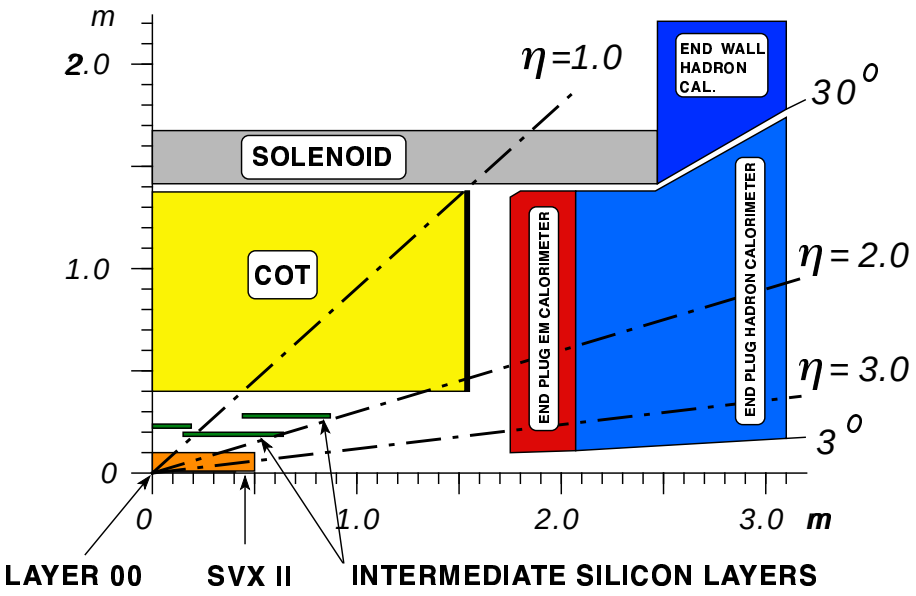

Figure 2.7: Longitudinal view of the CDF tracking system, representing a quarter of the detector.

on each side of the interaction point. Each barrel is divided into 12 wedges in ϕ, and each wedge supports five layers of double-sided silicon microstrip detectors between the radii of 2.4 and 10.7 cm from the beam line, to cover the region $-2 < \eta < 2$. Three of the layers combine the $r - \phi$ measurement on one side with a 90° stereo measurement on the other. The remaining two layers combine the $r - \phi$ measurements on one side, with a small stereo angle of 1.2° on the other. The stereo angle information from all the layers is combined to form a three dimensional track. A highly parallel fiber-based data acquisition system reads out the entire detector in approximately 10 μs. Table 2.1 shows the design parameters of the SVX.

The Intermediate Silicon Layers (ISL) use a similar technology to that of SVX, from the silicon itself, through the readout electronics. In the central region, a layer of double sided silicon is placed at a radius of 22 cm, while in the forward region, $1.0 \leq |\eta| \leq 2.0$, two layers of double sided silicon are placed at radii of 20 cm and 28 cm, where the coverage from the COT is incomplete or missing. Precision space point measurements at these radii will enable three dimensional track finding in the forward region. The best position resolution acheved is 9 μm which is for two-strip clusters in SVX II. The average offline tracking efficiency, defined as placing three silicon hits on a track that passes through three active layers of silicon, is 94%. The SVT (silicon track trigger) online tracking efficiency is over 80%.

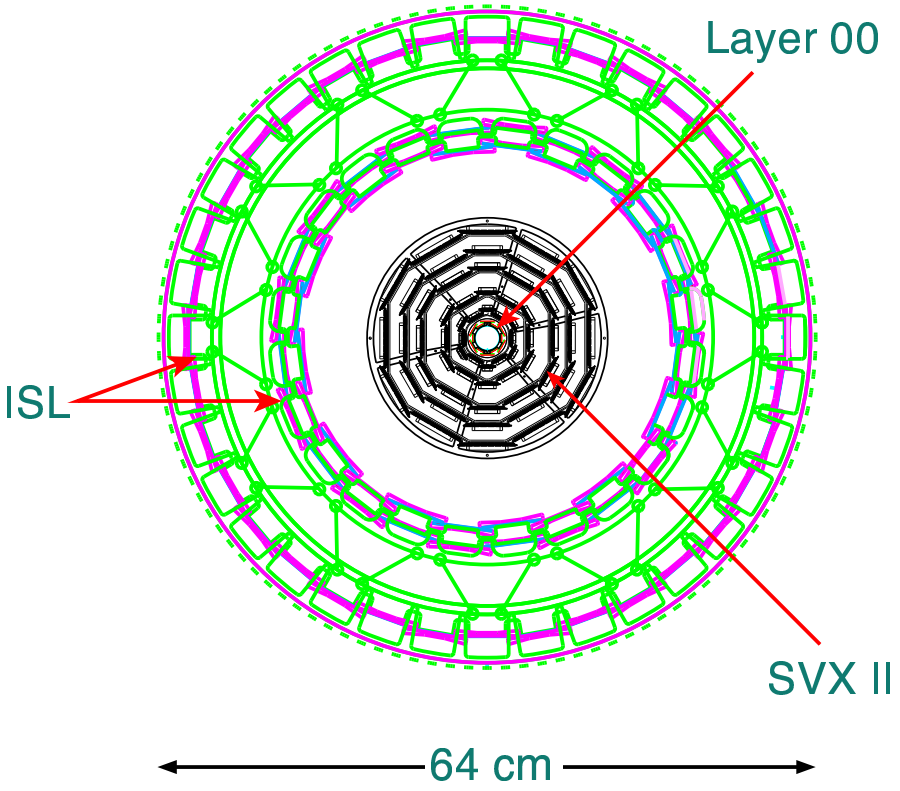

Figure 2.8: $r - \phi$ view of the silicon detectors.

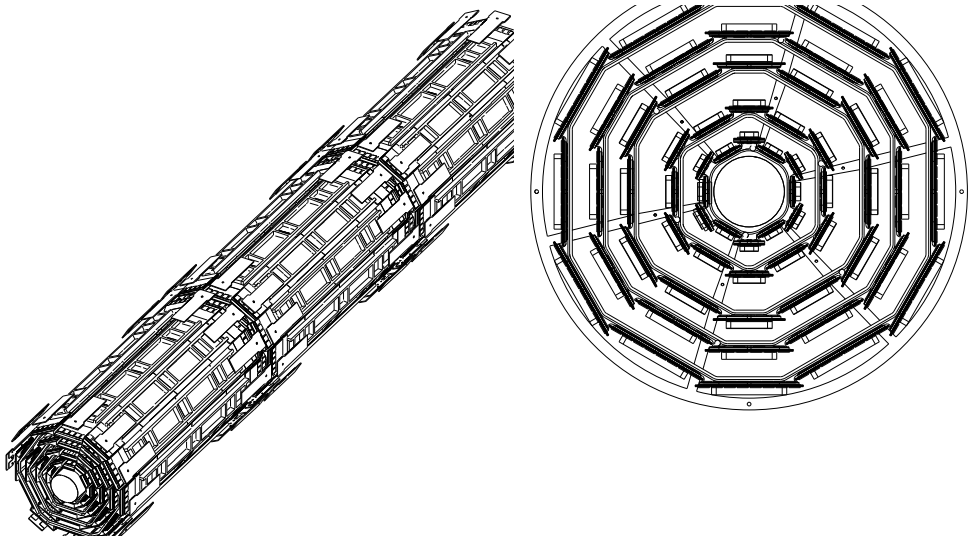

Figure 2.9: On the left, view of the three barrels of the SVX silicon detector. On the right, end view of one barrel showing the 12 wedges with the 5 layers.

Table 2.1: Design parameters of the SVX detector at CDF.

SVX	
Readout coordinates	$r-\phi$; $r-z$
Number of barrels	3
Number of layers per barrel	5
Number of wedges per barrel	12
Ladder length	29.0 cm
Combined barrel length	87.0 cm
Layer geometry	staggered radii
Radius innermost layer	2.44 cm
Radius outermost layer	10.6 cm
$r-\phi$ readout pitch	60; 62; 60; 60; 65 μm
$r-z$ readout pitch	141; 125.5; 60; 141; 65 μm
Length of readout channel ($r-\phi$)	14.5 cm
$r-\phi$ readout chips per ladder	4; 6; 10; 12; 14
$r-z$ readout chips per ladder	4; 6; 10; 8; 14
$r-\phi$ readout channels	211,968
$r-z$ readout channels	193,536
Total number of channels	405,504
Total number of readout chips	3,168
Total number of detectors	720
Total number of ladders	180

Central Outer Tracker

The Central Outer Tracker (COT) [65] has played a major role in charged particle tracking at CDF. It is an open-cell drift chamber which provides coverage for the region $|\eta| < 1$ as shown in Figure 2.7. The COT contains 30,240 sense wires in total that run the length (in z) of the chamber between two end plates, located from r=40 to 137 cm. The COT contains 96 sense wire layers in radius that are grouped into eight "superlayers", as inferred from the end plate section showed in Figure 2.10. Four of the superlayers are axial (run along the z direction) and the other four are stereo with stereo angles $\pm 2°$. The superlayers are alternated starting with a stereo superlayer. A cathode "field panel" which is gold on a 0.25 mil thick Mylar sheet is used instead of field wires. To adjust the electrostatics for the cell taper, the COT adjusts the voltage on the sense and potential wires within the cell (Figure 2.11). With a solid sheet for the cathode, the drift field and cathode surface field are the same, which allows for a much higher drift fields. A summary of the COT characteristics is given in Table 2.2. To ensure the operation of the COT detector, the maximum drift time is required to be less than the 396 ns bunch spacing in 36 bunch operation. A maximum drift time of about 177 ns is achieved in the COT, which has a maximum drift distance of 0.88 cm, when using a fast drift velocity gas mixture such as Argon / Ethane in the proportion of 50:50.

In this analysis the momenta of the tracks associated with the electrons are measured using the COT alone.

Table 2.2: Design parameters of the COT detector at CDF.

COT	
Number of Layers	96
Number of Superlayers	8
Stereo Angle(°)	+2, 0, -2, 0, +2, 0, -2, 0
Layers per Superlayer	12
Rapidity Coverage	$\|\eta\| < 1$
Drift field	2.5 keV/cm
Maximum Drift Distance	0.88 cm
Maximum Drift Time	177 ns
Number of Channels	30,240
Material Thickness	1.6% X_0

2.2.3 Calorimeters

Located outside the solenoid, the calorimetry system is used to measure the energy of charged and neutral particles, which covers the region $|\eta| < 3.0$. The calorimeter is divided into two physical sections, central ($|\eta| < 1$) and plug

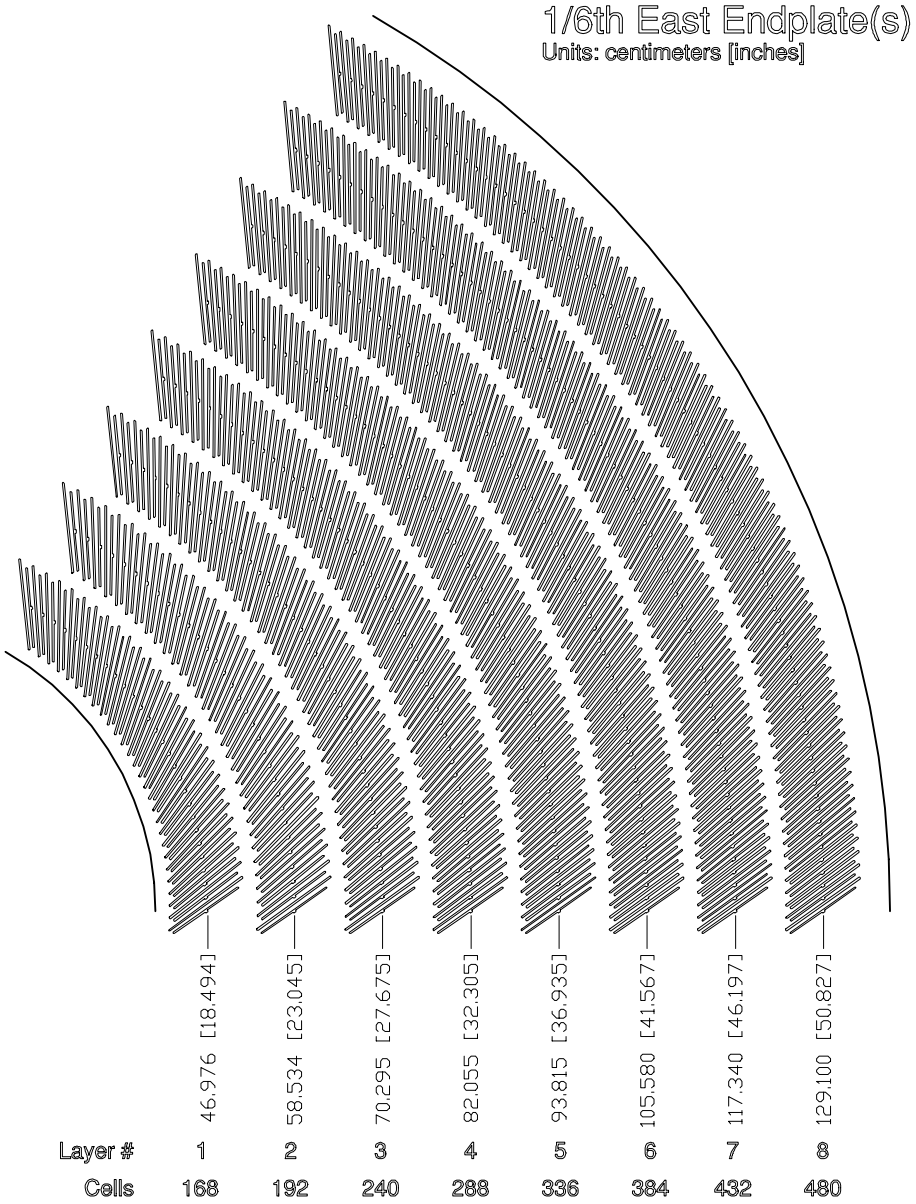

Figure 2.10: 1/6 section of the COT end plate. For each superlayer is given the total number of supercells, the wire orientation (axial or stereo), and the average radius.

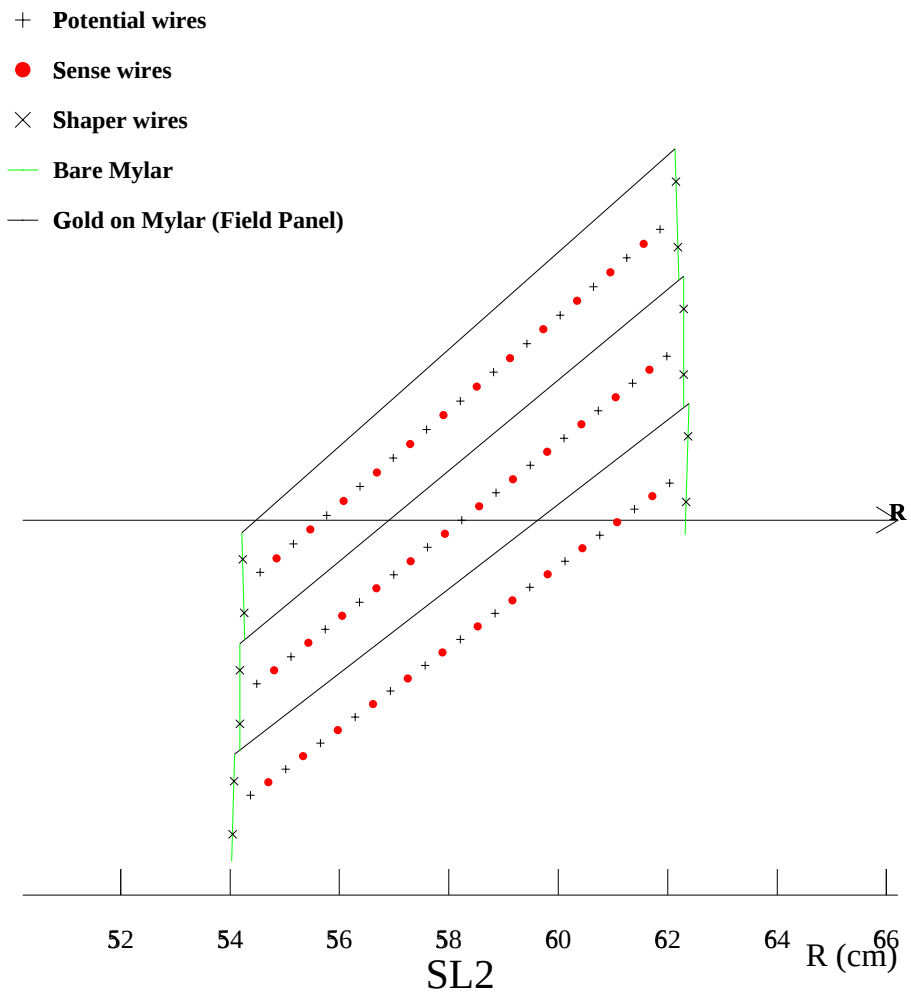

Figure 2.11: Three supercells in superlayer 2 looking along the beam (z) direction.

detector ($1.1 < |\eta| < 3.6$). Each sections is subdivided into an electromagnetic (CEM, PEM) and hadronic (CHA, PHA). The endwall hadronic calorimeter (WHA) covers a gap between the central and plug hadronic sections, as shown in Figure 2.7.

The Central Electromagnetic Calorimeter (CEM) [66] is a sampling calorimeter made of lead sheets interspersed with polystyrene scintillator. It detects electrons and photons and measures their energy. While other particles that interact electromagnetically may also deposit some of their energy in the CEM, electrons and photons deposit almost all of their energy in the calorimeter. The CEM total thickness is 18 radiation length (32 cm), to make sure that 99.7% of the elctrons energy will be deposited. The shower topology information allows us to distinguish an electron or a photon from a light hadron (π or K) or muon signals that may also shower in the calorimeter, since the transverse development of the showers is different for these particles. While passing through the calorimeter, particles interact with the material producing 'showers' of photons, electrons and positrons depending on their nature. Electrons and photons will start showering earlier and their showers will be almost constrained to the EM sections, while hadrons (such as pions) in the form of hadronic jets will start later releasing a significant fraction of their energy in the hadronic portions.

As shown in Figure 2.12, a proportional strip chamber (CES) is inserted into the stacks between the 8th layer of lead and the 9th layer of scintillator. The location is at a depth of six radiation lengths, and corresponds to the longitudinal shower maximum. A detailed view of a CES chamber is shown in Figure 2.13. The chambers consist of crossed anode wires and cathode strips. The wires run along z spaced at 1.45 cm and measure the azimuthal position of the electromagnetic shower within the CEM wedge. The cathode strips run in the ϕ direction and measure the z position of the shower. The cathode spacing is 1.67 cm in towers zero through four, and 2.01 cm in towers five through nine. The CEM has an average energy resolution

$$\left(\frac{\sigma(E)}{E}\right)^2 = \left(\frac{13.5\%}{\sqrt{E_T}}\right)^2 + (2\%)^2, \tag{2.5}$$

where E_T is the transverse energy of the detected particle in GeV. The position resolution is 2 mm at 50 GeV. A second set of proportional chamber, the Central Preradiator (CPR) detector is placed in between the front face of the EM calorimeters and the magnet coil. This chamber can be very useful in the pion-photon separation and in the identification of the electrons.

The CHA is an iron-scintillator sampling calorimeter, approximately 4.5 λ_0 (interaction lengths) in depth, and has

$$\left(\frac{\sigma(E)}{E}\right)^2 = \left(\frac{50\%}{\sqrt{E_T}}\right)^2 + (3\%)^2. \tag{2.6}$$

The WHA is also an iron-scintillator sampling calorimeter, spanning a range in pseudorapidity of $0.7 < |\eta| < 1.3$. The WHA has a depth of about 4.5 λ_0,

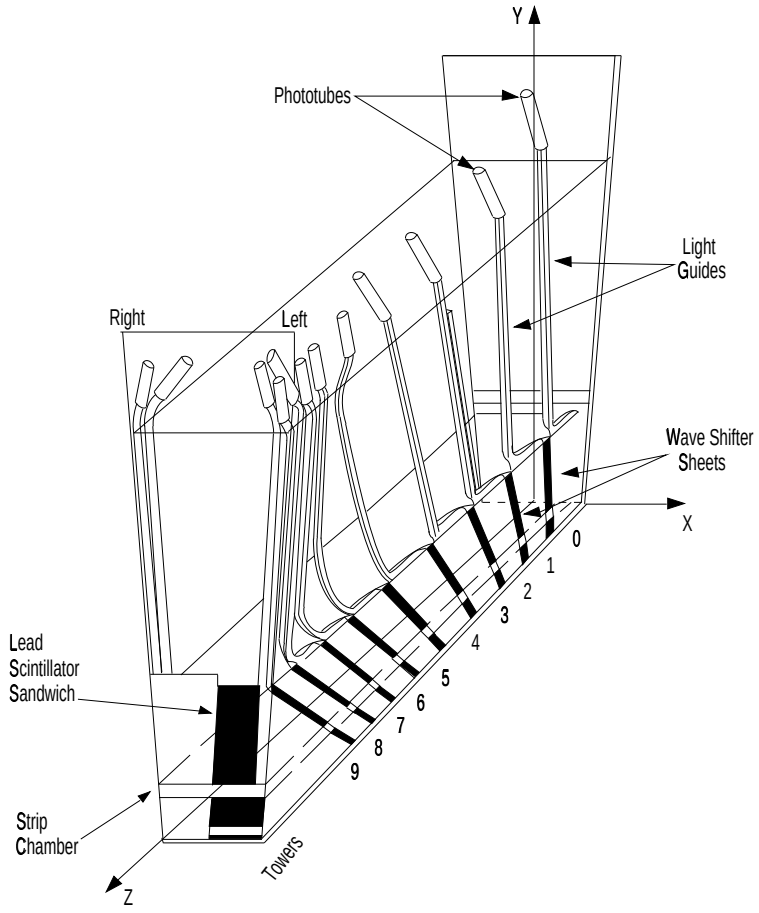

Figure 2.12: A diagram of a single CEM wedge. The ten towers are labeled 0 through 9, and the location of the CES strip chambers is also shown.

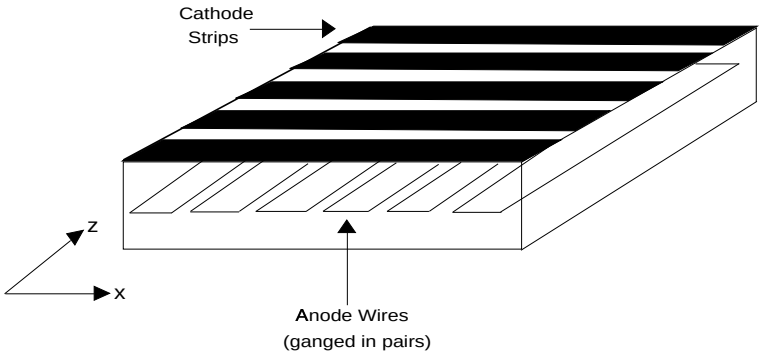

Figure 2.13: A portion of the central electromagnetic strip chamber.

similar to the CHA, however it has worse energy resolution,

$$\left(\frac{\sigma(E)}{E}\right)^2 = \left(\frac{75.5\%}{\sqrt{E_T}}\right)^2 + (4\%)^2. \tag{2.7}$$

The plug upgrade calorimeter covers the polar angle region from 3° to 37° ($1.1 < |\eta| < 3.6$). The top half of one plug is shown in cross section in Figure 2.14. Each plug wedge spans 15° in azimuth, however from $1.1 < |\eta| < 2.11$ (37° to 14°) the segmentation in ϕ is doubled, and each tower spans only 7.5°. There is an electromagnetic section (PEM) with a shower position detector (PES), followed by a hadronic section (PHA).

The PEM calorimeter is a lead/scintillator sampling type, with unit layers composed of 4.5 mm lead and 4 mm scintillator. There are 23 layers in depth for a total thickness of about 21 X_0 (radiation length) at normal incidence. The PEM has an energy resolution of

$$\left(\frac{\sigma(E)}{E}\right)^2 = \left(\frac{16\%}{\sqrt{E_T}}\right)^2 + (1\%)^2. \tag{2.8}$$

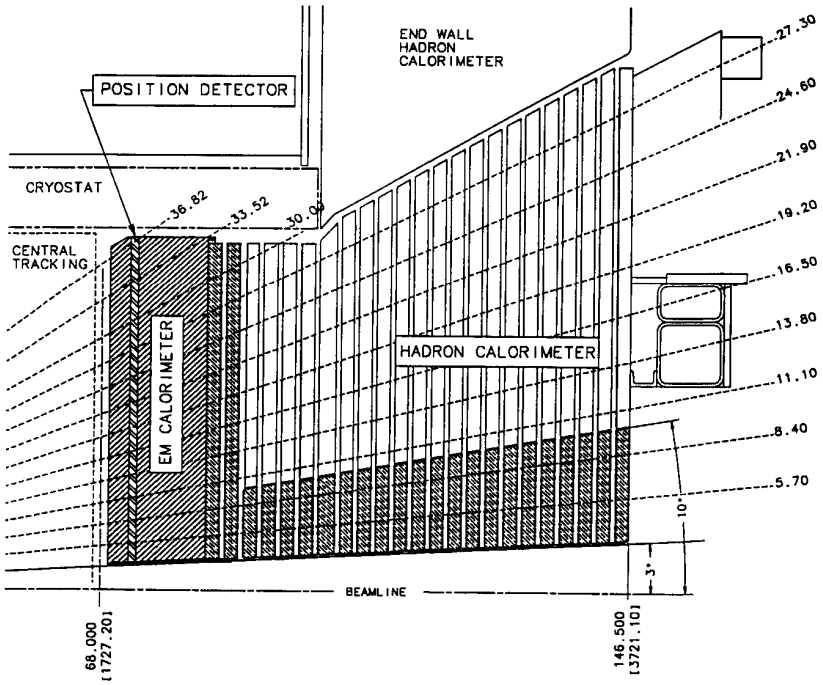

Figure 2.14: The Cross section of upper part of the end plug calorimeter.

The PHA is an iron-scintillator sampling calorimeter, approximately 7 λ_0 in depth, and has an energy resolution of

$$\left(\frac{\sigma(E)}{E}\right)^2 = \left(\frac{80\%}{\sqrt{E_T}}\right)^2 + (5\%)^2. \tag{2.9}$$

The PEM shower maximum detector is located about 6 λ_0 deep within the PEM, and is constructed of two layers (donated 'U' and 'V') of scintillating strips. The strips are 5 mm wide, and roughly square in cross section. Position resolution of the PES is about 1 mm.

2.2.4 Muon Chambers

Muons penetrate the tracking systems and the calorimeters leaving very little energy. The reason is muons produce much less bremsstrahlung than electrons and therefore do not produce electromagnetic showers, due to their larger mass. The CDF muon systems [67] use this property by placing detectors behind enough material. Muons deposit minimum ionizing energy in the calorimeters matched with a track in the COT. The momentum of these muons is measured by their bend in the solenoidal field using the COT. The central muon system is capable of detecting muons with transverse momentum $p_T \geq 1.4$ GeV, through their interaction with the gas and subsequent drift on the produced electrons toward the anode wires. The detection of high p_T muons is very important because their most probable source is a vector boson decay.

The muon systems consist of four separate subsystems: the central muon chambers (CMU), the central muon upgrade (CMP), the central muon extension (CMX), and the barrel muon detector (BMU). The BMU detector was not fully integrated in time for the analysis, but will eventually provide triggerable coverage between $1.0 < |\eta| < 1.5$. Figure 2.15 shows a plot of the effective muon detector coverage in $\eta - \phi$ space for this analysis. Table 2.3 shows design parameters of the detectors.

The CMU detector located directly outside of the central hadron calorimeter, 35 m from the interaction point, and covers the region of $|\eta| \leq 0.6$. It is divided into 24 east and 24 west 15°-wedges. Each wedge contains three muon chambers and each muon chamber consists of four layers of four rectangular drift cells staggered in order to eliminate hits position ambiguities. A stainless steel sense wire with a diameter of 50 μm is located in the center of each cell. By comparing the drift times for alternating layers, we resolve the ambiguity of which side of sense wires the muon passed. Figure 2.16 shows a CMU chamber drift cells. A muon object is created by forming a stub[3] from hits in the muon chambers matching it to an extrapolated COT track.

The CMP consists of a second set of muon chambers behind additional 60 cm of steel in the region $55° \leq \theta \leq 90°$. The chambers are fixed length in z and form

[3]We will call the short tracks reconstructed in the muon chambers "stubs" to distinguish them from tracks reconstructed in the central tracker.

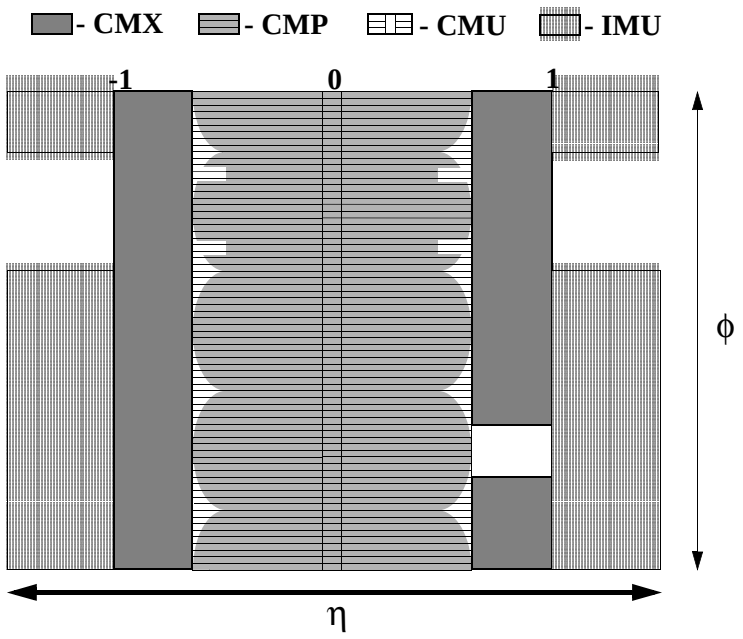

Figure 2.15: Muon detector coverage.

Table 2.3: Design parameters of the muon detectors at CDF. Pion interaction lengths and multiple scattering are computed at a reference angle of $\theta = 90°$ in CMU and CMP/CSP, at an angle of $\theta = 55°$ in CMX/CSX, and show the range of values for the BMU.

	CMU	CMP/CSP	CMX/CSX	BMU
Coverage	$\|\eta\| \leq 0.6$	$\|\eta\| \leq 0.6$	$0.6 \leq \|\eta\| \leq 1.0$	$1.0 \leq \|\eta\| \leq 1.5$
Drift tube cross section	2.68×6.35 cm	2.5×15 cm	2.5×15 cm	2.5×8.4 cm
Drift tube length	226 cm	640 cm	180 cm	363 cm
Max drift time	800 ns	1.4 μs	1.4 μs	800 ns
Total drift tubes	2304	1076	2208	1728
Scinti. counter thickness		2.5 cm	1.5 cm	2.5 cm
Scinti. counter width		30 cm	30 - 40 cm	17 cm
Scinti. counter length		320 cm	180 cm	180 cm
Total counters		269	324	864
Pion interaction length	1.5	7.8	6.2	6.2 - 20
Minimum detectable muon p_T	1.4GeV/c	2.2GeV/c	1.4GeV/c	1.4-2.0GeV/c
Multiple scattering resolution	12 cm/p	15 cm/p	13cm/p	13-25cm/p

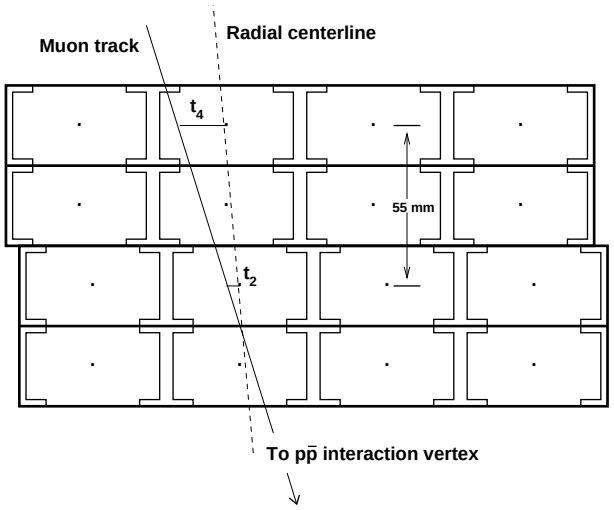

Figure 2.16: The cross-sectional view of drift tubes in a muon chamber. A stub is formed from the trajectory of a muon passing through the chamber, and the stub is matched to a track to become a reconstructed muon.

box around the central detector. The pseudorapidity coverage thus varies with azimuth as shown in Figure 2.15. The inner and outer surfaces of the detector are lined with scintillator planes (CSP) to provide timing information for the trigger system.

The central extension consists of conical section of drift tubes (CMX) and scintillation counters (CSX) located at each end of the central detector and extending in polar angle from 42° to 55° ($0.6 \leq |\eta| \leq 1.0$).

2.2.5 Luminosity Monitors

CDF monitors the instantaneous luminosity of the Tevatron using a Cherenkov Luminosity Counter (CLC) [68–70]. There are two CLC detector modules in the CDF detector installed in a '3-degree holes' inside the CDF end plug calorimeter, which covers the region $3.7 \leq |\eta| \leq 4.7$. Each CLC module consists of 48 thin, long, conical, gas-filled, Cherenkov counters.

2.3 DAQ and Trigger Systems

The CDF electronics systems have substantially been altered to handle run II accelerator conditions. The increased instantaneous luminosity requires a similar increase in data transfer rates and the reduced separation between accelerator bunches a new architecture for the readout system.

In this section, I begin with a brief description of the front end electronics for the silicon detector, calorimeter and muon systems. I then describe the data

aquisition system (DAQ) and trigger systems.

2.3.1 Front-End Electronics

The silicon signals are readout by on-board, radiation hardened CMOS custom integrated circuits which are mounted on an electrical hybrid on the surface of the silicon detectors. Including both sides of the detectors there are 44 chips in a wedge with 12 wedges per barrel end and six barrel ends in total. Each readout chip set (SVX3) has 128 channels, each with a charge-sensitive amplifier, a 42-cell dual-ported pipeline with four additional cells for buffers, and an ADC. The chips from each wedge are read out over five high density interconnects (HDI), one per layer. The HDI's from each wedge are connected to a port card (PC) with a high density copper cable located around the periphery of the barrel ends. The PC decodes the control signals from the fiber interface board (FIB). Also at the PC, the analog data, already in digital form, are converted from electrical to optical signals by dense optical interface modules (DOIM's). Each DOIM drives a ribbon of optical fibers at 53 MHz approximately 10 m to VME crates located on the side of the CDF detector. This highly parallel readout permits the entire detector to be read out in approximately 10 μs.

The calorimeter ADC readout is based on the QIE (Charge Integrating and Encoding) chip [71], a custom multi-ranging circuit. A VME based front-end board carries the QIE, a commercial ADC, and FPGA based circuits to perform pipeling, buffering, and the creation of transverse-energy sums for the trigger. A simplified version of the QIE design is used for all shower maximum and preshower detectors.

The gain of the CMU system is reduced and the chambers operate in proportional regime for the high luminosity running of run II. In order to implement this pre-amplifiers was installed to the end of the CMU chambers. The output of the pre-amps drive amplifier-shaper-discriminator (ASD) cards, followed by TDC's.

The hadron calorimeters, scintillators, muon chambers, and the central drift chamber all require TDC's for recording signal times.

2.3.2 DAQ

The data acquisition system is responsible for collecting data fragments from front-end electronics systems for events satisfying the Level-2 trigger and sending them to the Level-3 trigger subsystem. There complete events are built and more sophisticated algorithms classify events and determine whether they should be saved. Events passing the Level-3 trigger criteria are sent to mass storage. The online computing system provides processes that control and monitor the functioning of the detector and data acquition system.

2.3.3 Trigger Systems

The trigger plays an important role in hadron collider experiments because the collision rate is much higher than the rate at which data can be stored on tape. The crossing rate of the Tevatron under 36 on 36 bunch operation is 7.6 MHz, corresponding to 396 ns collision separation. The role of the trigger is to effectively extract the most interesting physics events from the large number of minimum bias events. For Run II, CDF employs a three-level trigger system to selectively capture interesting events. The levels are denoted simply as 'L1', 'L2' and 'L3', with each subsequent level making more complicated decisions and requiring successively longer processing times. Figure 2.17 shows schematic of the CDF trigger system.

The L1 trigger operates with 5.5 μs latency to allow enough time for data transfer and decision making, implying that buffering capacity for 42 crossing must be build into the system in order for L1 to remain "deadtime-less". The input to the L1 hardware comes from calorimeters, tracking chamber, and muon detectors. The decision to retain an event for further processing is based on the number and energies of electron, muon, and jet candidates, as well as the missing transverse energy (See section 3.3.2) in the event. The COT information is first processed by the 'XFT' (eXtremely Fast Tracker) before being sent to the trigger, thus for the first time there is tracking information available at L1.

If an event is accepted at L1, it is transferred to one of four L2 buffers. All of the information used in the L1 decision is available to the L2 system, but with higher precision. In addition, data from the central calorimeter showermax detector allows improved identification of electrons and photons. Jet reconstruction is provided by the L2 cluster finder; secondary vertex information is produced by the SVT (Silicon Vertex Tracker) [72]. A L2 accept initiates full detector readout for the event.

The L3 trigger subsystem is composed of two main components, the Event Builder (EVB) and the L3 Farm. The L1 and L2 subsystems need to make their decisions at a very high rate which makes it impossible to fully reconstruct each event. While L1 and L2 are making their decision, the event pieces are stored in the buffers of numerous Front End (FE) crates. After a L2 decision is made, the Event Builder assembles all event fragments from the Front End crates into one data block. The L3 farm receives a single and complete but disordered block of data from the event builder. The L3 farm reconstructs an event and applies a software trigger, then make a decision whether or not to permanently store it. L3 accepts events with a rate of approximately 75 Hz. Data from the L3 computer farm are monitored in real time by dedicated Linux PCs in the CDF control room. Events which pass the L3 trigger are sent to the Feynman Computing Center at a maximum rate of about 40 Hz. From there the data are written to tape and stored for further processing.

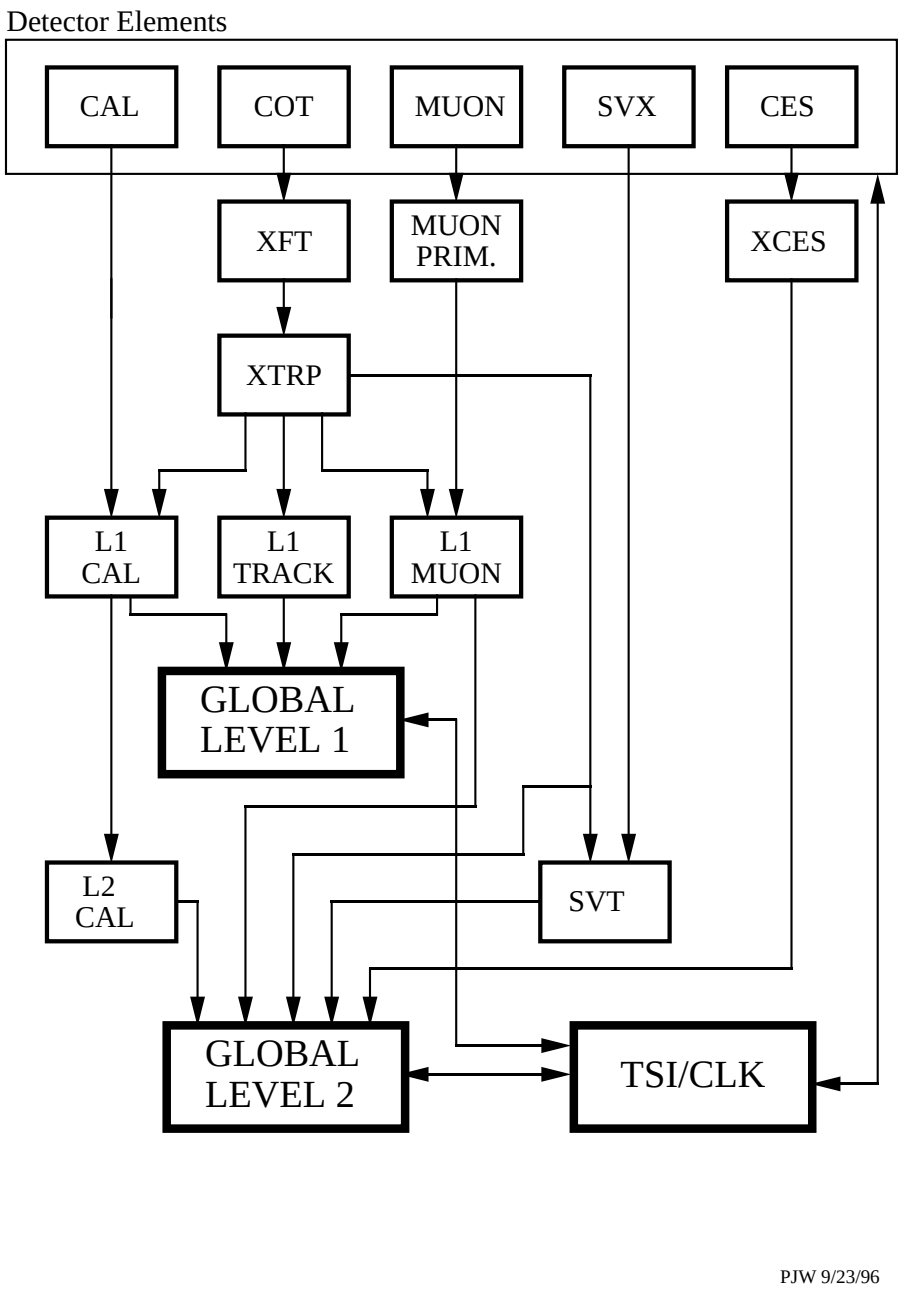

Figure 2.17: Block diagram of the CDF II trigger system.

Chapter 3

Muon Channel W Event Selection

The $W + \gamma$ analysis first selects an inclusive sample of W bosons using their muon decay modes, then identifies centrally produced photons. $W \to \mu\nu$ events are selected by requiring a high quality, isolated muon and large missing energy. In the end, I found 56558 CMUP $W \to \mu\nu$ candidates and 31216 CMX $W \to \mu\nu$ candidates for a grand total of 87774 W boson candidates.

The data samples used in this analysis are described in Section 3.1. The procedure for identifying muons and neutrinos, and the W boson selection criteria are described in Sections 3.2 through 3.3. The backgrounds in the inclusive $W \to \mu\nu$ events is categorized in Section 3.4. W event distributions are shown in Section 3.5, and the acceptance is discussed in Section 3.6. Finally, the $W \to \mu\nu$ cross section is presented in Section 3.7.

3.1 Data Samples

3.1.1 Central Muon Triggers

The data for this analysis is selected from the inclusive high p_T muon triggered dataset using the good runs (detailed in Section 3.1.2) recorded from March 23rd, 2002 until September 6th, 2003. This includes run numbers between 141544 and 168889. The high p_T muon triggered dataset fires the `MUON_CMUP18` or `MUON_CMX18` trigger paths. The specific trigger requirements for the `MUON_CMUP18` path are

Level 1 L1_CMUP6_PT4. This requires matched hits with arrival times within 124 ns of each other on one of two projective wire pairs within a single CMU stack, a matched XFT track with $p_T > 4$ GeV/c, and a matching pattern of projective hits in 3/4 CMU layers.

Level 2 L2_AUTO_L1_CMUP6_PT4, L2_TRK_L1_CMUP6_PT4 (runs 141544 - 152616, runs 152669 - 168889). No requirement for early run period and

requirement of at least one XFT track with $p_T > 8$ GeV/c (no muon stub matching) for later runs.

Level 3 L3_MUON_CMUP18. This requires a reconstructed muon track with CMU and CMP stubs and $p_T > 18$ GeV/c. The CMU (CMP) stub is required to be within 10 (20) cm of the extrapolated COT track in the $r - \phi$ plane, $|\Delta X_{\rm CMU}| < 10$ cm ($|\Delta X_{\rm CMP}| < 20$ cm).

The specific trigger requirements for the `MUON_CMX18` path are

Level 1 L1_CMX6_PT8, L1_CMX6_PT8_CSX (runs 141544 - 152616, 152669 - 168889). This requires matched hits with arrival times within 124 ns of each other on one of two projective wire pairs within a single CMX stack, a matched XFT track with $p_T > 8$ GeV/c, and for later runs an in-time, matching scintillator hit on 1/2 CSX layers.

Level 2 L2_AUTO_L1_CMX6_PT8, L2_AUTO_L1_CMX6_PT8_CSX (runs 141544 - 152616, runs 152669 - 168889). No additional requirements.

Level 3 L3_MUON_CMX18. This requires a reconstructed muon track with a CMX stub and $p_T > 18$ GeV/c. The CMX stub is required to be within 20 cm of the extrapolated COT track in the $r - \phi$ plane, $|\Delta X_{\rm CMX}| < 20$ cm.

The Level 3 trigger dataset for high p_T muons described above are identified as **bhmu08** and **bhmu09**, which uses the cdf software of offline version 4.8.4 to perform reconstruction.

3.1.2 Good Run List

All runs used in this analysis are required to satisfy a minimal set of requirements and maintained as a 'Good Run List' database which contains the amount of luminosity written to tape and the status of all detector components. This analysis includes all periods of continuous data taking with more than 10 nb^{-1} of data written to tape. The parts of a run where any detector component other than the silicon vertex detector were not properly functioning are excluded.

3.1.3 Luminosity Measurement

The total integrated luminosity is derived from the rate of the inelastic $p\bar{p}$ events measured with the luminosity monitor Cherenkov Luminosity Counters (CLC)(see Section 2.2.5).

The integrated luminosities corresponding to the period from March 23rd 2002 until September 6th 2003 are 192 pb^{-1} for muons in the CMU and CMP (denoted CMUP) detector region $|\eta| < 0.6$ and 175 pb^{-1} for muons in the CMX detector region $0.6 < |\eta| < 1.0$. The lumonosity uncertainty is 6%, of which 4.5% comes from the acceptance of the lumonosity monitor and 5% comes from the estimate of the total $p\bar{p}$ cross section [73].

3.2 Central Muon Variables and Correction

In this section the variables and cut values used to select muons are summarized.

Trigger requirement All $W \to \mu\nu$ events are required to satisfy either the CMUP or CMX trigger paths used to collect events for this analysis.

Track momentum p_T Track transverse momentum associated with muon is greater than 20 GeV/c. The track is selected as the beam-constrained COT track with the highest momentum pointing to the muon stub.

Track impact parameter The impact parameter, d_0, is corrected for the measured position of the beam. If the muon track has silicon hits('SVX') a cut is applied with $|d_0| < 0.02$ cm and if it doesn't have silicon hits('COT') $|d_0| < 0.2$ cm. This cut is the most powerful for rejecting cosmic rays background.

COT exit radius ρ_{COT} To ensure that each reconstructed muon in my sample pass through all eight COT superlayers having high efficiency for triggering the event, a cut on the exit radius of a track at the end-plates of the COT $\rho_{\mathrm{COT}} > 140$ cm is applied.

$$\rho_{\mathrm{COT}} = \frac{\eta}{|\eta|} \cdot \frac{Z_{\mathrm{COT}} - Z_0}{\tan(\lambda)} \tag{3.1}$$

where

$$\lambda = \frac{\pi}{2} - \theta, \quad \text{and} \quad \theta = 2 \cdot \tan^{-1}(e^{\eta}). \tag{3.2}$$

$\boldsymbol{E_{\mathrm{EM}}}$ Energy deposited to the central electromagnetic calorimeter (CEM).

$\boldsymbol{E_{\mathrm{HAD}}}$ Energy deposited to the central hadron calorimeter (CHA).

$\boldsymbol{z_0}$ The z vertex position of the high p_T muon track extrapolated to the beamline.

Isolation Fraction The isolation of the muon is computed from the sum of all calorimeter energy found in a cone of R(=radius) < 0.4 around the muon divided by the transverse momentum of the muon. The energy assigned to the muon track is not included in this sum.

$\boldsymbol{|\Delta X_{\mathrm{CMU}}|}$ Track and stub matching in the CMU, $|\Delta X_{\mathrm{CMU}}| < 3$ cm (CMUP).

$\boldsymbol{|\Delta X_{\mathrm{CMP}}|}$ Track and stub matching in the CMP, $|\Delta X_{\mathrm{CMP}}| < 5$ cm (CMUP).

$\boldsymbol{|\Delta X_{\mathrm{CMX}}|}$ Track and stub matching in the CMX, $|\Delta X_{\mathrm{CMX}}| < 6$ cm (CMX).

CMP Bluebeam Veto Sections of the 'bluebeam' region of the CMP detector were not functional for all of the runs in the sample. I reject reconstructed muons with the stubs formed from hits in the region. This detector section is also turned off in the simulation used to calculate the acceptance.

CMX Mini-Skirt/Keystone Veto Sections of the 'Mini-skirt/Keystone' region of the CMX detector were not functional as well. I reject reconstructed muons with the stubs formed from hits in the region.

The series of selection criteria used for $W \rightarrow \mu\nu$ events can be found in Table 3.1. Table 3.2 shows the number of events in data sample that survive

Table 3.1: Selection requirements for $W \rightarrow \mu\nu$ events.

Quantity	Purpose
$\geq$1 CMUP/CMX fiducial muons	Muon chamber active regions
Trigger bit	Enforce online trigger
$p_T^\mu > 20$ GeV	High trigger efficiency
$\lvert\Delta X_{\rm CMU}\rvert < 3$ cm	Good track - CMU match
$\lvert\Delta X_{\rm CMP}\rvert < 5$ cm	Good track - CMP match
$\lvert\Delta X_{\rm CMX}\rvert < 6$ cm	Good track - CMX match
$E_{\rm EM} < \max(2, 2 + 0.0115 \cdot (p - 100))$ GeV	Minimum ionization
$E_{\rm HAD} < \max(6, 6 + 0.0280 \cdot (p - 100))$ GeV	Minimum ionization
$\lvert z_0^\mu\rvert < 60$cm	Calorimeter projectively
Exit radius of track $\rho_{\rm COT} < 140$ cm (CMX)	Good quality track
$\lvert d_0\rvert < 0.02$ cm (SVX) or < 0.2 cm (COT)	Cosmic ray rejection
3 axial segments with at least 7 COT hits	Good quality track
3 stereo segments with at least 7 COT hits	Good quality track
Isolation fraction < 0.1	QCD rejection
Cosmic tagger veto	Cosmic ray rejection
$Z \rightarrow \mu\mu$ rejection	Background rejection
$\not\!\!E_T > 20$ GeV	Background rejection
$30 < M_T < 120$ GeV	Background rejection

each step in the selection process.

For 30% of the runs in the data sample the silicon detector was switched off. To equalize the events in the runs with and without the silicon detector on, I removed all silicon hits from the tracks. Then refit the track with the COT hits using the measured beamline as an additional constraint in the fit. The resulting beam-constraint COT-only tracks are used in all the subsequent analysis work here except for the impact parameter of the track.

The beam-constrained tracking may introduce a p_T curvature bias. The p_T of the tracks are corrected as

$$\frac{q}{p_T(\text{corrected})} = \frac{q}{p_T(\text{uncorrected})} - 0.00037 - 0.00110 \cdot \sin(\phi + 0.28), \quad (3.3)$$

where q is the charge of the track and ϕ is the azimuthal angle of the track.

As mentioned above, there is one case where I use the silicon hit information on the track when it is available: To calculate the impact parameter of the track

Table 3.2: Number of events surviving each step in the $W \rightarrow \mu\nu$ selection process.

Cuts	CMUP	CMX
$\geq$1 CMUP/CMX fiducial muons	1181570	536669
`MUON_CMUP18`/`MUON_CMX18` trigger	1129718	506322
$p_T > 20$ GeV/c	660233	231594
$\lvert\Delta X_{\rm CMU}\rvert < 3$ cm	467949	231594
$\lvert\Delta X_{\rm CMP}\rvert < 5$ cm	375337	231594
$\lvert\Delta X_{\rm CMX}\rvert < 6$ cm	375337	185110
$E_{\rm EM} < \max(2, 2 + 0.0115 \cdot (p - 100))$GeV	327629	147970
$E_{\rm HAD} < \max(6, 6 + 0.0280 \cdot (p - 100))$GeV	312515	137224
$\lvert z_0\rvert < 60$ cm	211534	127361
Exit radius of track $\rho_{\rm COT} < 140$ cm	211530	115389
3+ Axial and Stereo segments with 7+ hits	170892	81143
$\lvert d_0\rvert < 0.02$ cm (silicon), 0.2 cm (no silicon)	116756	63997
Isolation fraction < 0.1	82880	44348
Cosmic tagger veto	78784	43783
$Z \rightarrow \mu\mu$ rejection criteria	71591	39824
$\not\!\!E_T > 20$ GeV	57488	31867
$30 < M_T < 120$ GeV	56558	31216

(d_0). When the silicon information present, I constrain the track to go through the beamline given by the silicon. It there is no silicon information available, the track is constrained to go through the beam given by the COT. I apply a different cut value for the d_0 parameter depending on whether or not tracks contain any silicon hit information shown in Table 3.1.

3.3 W Boson Criteria

The fiducial and kinematic criteria for selection of $W \rightarrow \mu\nu$ candidate events are as follows:

Cosmic ray rejection Cosmic tagger veto (Section 3.3.1).

Missing Energy $\not\!\!E_T > 20$ GeV/c (Section 3.3.2).

Transverse Mass $30 < M_T(\mu, \nu) < 120$ GeV (Section 3.3.2).

Z **rejection** Events with a second energetic track which pass these requirements listed below are rejected as a potential background from $Z \rightarrow \mu^+\mu^-$ detailed in Section 3.4.1.

- $p_T > 10$ GeV/c
- $E_{\rm EM} < max(3, 3 + 0.0140 \cdot (p - 100))$
- $E_{\rm HAD} < max(6, 6 + 0.0420 \cdot (p - 100))$

3.3.1 Cosmic Ray Contamination

Energetic cosmic ray muons traverse the detector at a significant rate, leaving hits in both muon and COT chambers and passing the high p_T muon trigger requirements. Thus the original muon data set is heavily contaminated with cosmic ray events.

A cosmic muon, passing through the detector, represents itself as a combination of incoming and outgoing legs relative to the beam line of the detector. To be recorded in the data, at least one such leg should form a good COT track with muon stubs linked to it. Often the other leg also gets reconstructed as a track or muon. The majority of events triggered by cosmic muons have much lower tracking multiplicity in comparison to hits from collision events. On the other hand, the fraction of events in which the cosmic muon hits the detector during the collision is quite significant.

Muons from cosmic rays are generally very isolated and easily pass the muon identification cuts listed in Table 3.1. When only one cosmic leg is reconstructed, the event can imitate the W signature. Therefore, an effective cosmic tagging technique is required to reduce cosmic background.

The cosmic ray tagging algorithm utilizes the timing information from the COT hits. The core of this method is a multi-parameter fit over the set of

hits left by the incoming and outgoing cosmic legs. The leg belonging to the reconstructed muon serves as the seed track for the fit. The other leg is referred to as the opposite track. The algorithm performs in the following steps:

- Hits belongs to the seed track are refitted with the five helix parameters and the global time shift.
- Based on the best value of the fit, incoming or outgoing hypothesis is assigned to the seed track.
- The refitted seed track is used to find the other cosmic leg by defining a "road" in which hits are searched for.
- If enough hits are found, a similar fit is performed to produce the opposite track.
- For the seed and the opposite tracks a simultaneous fit is performed to combine all hits into a single helix.

The final decision of the cosmic tagger depends on the assigned direction of the legs. If one leg is recognized as incoming and the other as outgoing, then the event is tagged as cosmic ray. For a pair of tracks coming out of a real beam collision, both legs should be categorized as outgoing.

3.3.2 Missing E_T Calculation

$W \to \mu\nu$ events are selected based on the requirement of large missing transverse energy ($\not\!\!E_T$) which arises from the energy carried away by undetected neutrino in the event.

The missing E_T is the vector which points opposite the vector sum of all calorimeter energy,

$$\not\!\!E_T{}^x = -\sum_i E_T^i \cos\phi^i, \tag{3.4}$$

where the sum extends over all towers, E_T^i is the transverse energy of the ith tower, and ϕ is the azimuthal angle. A similar expression holds for the y-component. The sum involves all towers with total energy (hadronic and electromagnetic) above 0.1 GeV within the region $|\eta| < 3.6$, corresponding to all central and plug calorimeter tower. By default, $\not\!\!E_T$ in the calorimeter is calculated assuming that the interaction point is located at $z = 0.0$ cm, therefore I corrected the $\not\!\!E_T$ for the position of the event vertex using the z_0 of the muon track. Corrections are made for identified muon, which do not deposit much energy in the calorimeters.

$$\not\!\!E_T{}^x(\text{corrected}) = \not\!\!E_T{}^x - (p_T^\mu - E_T^{EM(\mu)} - E_T^{HAD(\mu)}) \cdot \cos(\phi_\mu) \tag{3.5}$$

$$\not\!\!E_T{}^y(\text{corrected}) = \not\!\!E_T{}^y - (p_T^\mu - E_T^{EM(\mu)} - E_T^{HAD(\mu)}) \cdot \sin(\phi_\mu), \tag{3.6}$$

where $E_T^{EM(\mu)}$ and $E_T^{HAD(\mu)}$ are the electromagnetic and hadronic transverse energies measured in calorimeters towers directly along the path of the muon. ϕ_μ is the azimuthal angle of the muon.

I compute the transverse mass of each candidates as the longitudinal component of the neutrino momentum cannot be measured:

$$M_T \equiv \sqrt{p_T \not{E}_T - (p_x \not{E}_T^x \text{ (corrected)} + p_y \not{E}_T^y \text{ (corrected)})}, \tag{3.7}$$

where $p_T = |\vec{p_T}|$ is the absolute value of muon transverse momentum, p_x and p_y are resolved the p_T into x and y components.

3.4 W Backgrounds

In this section I estimate the contribution of the four main backgrounds to $W \to \mu\nu$ candidates. The backgrounds to be estimated are $Z \to \mu^+\mu^-$, $W \to \tau\nu$, QCD processes and cosmic rays. The sum of all these contributing background processes yields a total fraction of background events in the W sample of

$$b_W = 9.50 \pm 0.44(\%) \tag{3.8}$$

for CMUP $W \to \mu\nu$ muons and

$$b_W = 9.27 \pm 0.44(\%) \tag{3.9}$$

for CMX $W \to \mu\nu$ muons.

3.4.1 Electroweak Processes

$Z \to \mu^+\mu^-$ process can contribute to the sample of W candidates. In cases when a hard photon is radiated along the second muon or when the second track is not found with the Z veto due to the failure to filter out $Z \to \mu^+\mu^-$ decays.

$W \to \tau\nu$ can contribute the sample of W candidates when, for example, decay $\tau \to \mu\nu\bar{\nu}$ happens. In case when muon from tau decay has $p_T > 20$ GeV, the event will appear in my W sample, given that $\not{E}_T > 20$ GeV.

The size of these background processes is calculated using electroweak Monte Carlo samples. The fraction of these background events will be found to be:

$$b^W_{Z\to\mu\mu} = 5.55 \pm 0.24(\%) \text{ and } b^W_{W\to\tau\nu} = 3.13 \pm 0.07(\%) \tag{3.10}$$

for CMUP $W \to \mu\nu$ muons and

$$b^W_{Z\to\mu\mu} = 5.33 \pm 0.23(\%) \text{ and } b^W_{W\to\tau\nu} = 3.18 \pm 0.16(\%) \tag{3.11}$$

for CMX $W \to \mu\nu$ muons.

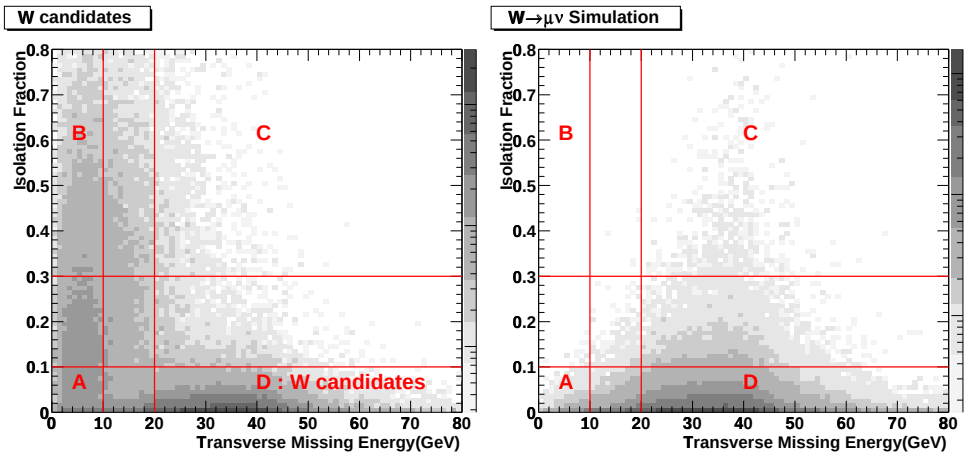

Figure 3.1: Distribution of transverse missing E_T versus isolation fraction for the $W \rightarrow \mu\nu$ candidate events and $W \rightarrow \mu\nu$ simulation.

3.4.2 QCD Backgrounds

Hadronic jets producing real or fake muons in the detector can contribute to the sample of W candidates. In order for these events to be accepted into my candidate sample, there must be a significant event energy mis-measurement to reproduce the $\not\!\!E_T$ signature. Because of this fact, these events tend to sit in odd regions of parameter space and are particularly difficult to model. The main method to estimate QCD backgrounds contamination is to extrapolate the number of background events from a region away from the W signal into the W signal region. Contrary to electroweak processes, the majority of these QCD background events have relatively small missing transverse energy and large isolation ratio. For that reason I choose to look at the isolation fraction versus $\not\!\!E_T$ ratio distributions to determine the number of the background events shown in Figure 3.1. The $W \rightarrow \mu\nu$ signal events are visible in the region of isolated muon with large missing energy. This method is based on the assumption that there is no correlation between isolation fraction and $\not\!\!E_T$ in QCD background events.

In the isolation fraction versus $\not\!\!E_T$ parameter space, these four regions are defined as follows:

- Region A : Isolation fraction < 0.1 and $\not\!\!E_T < 10$ GeV
- Region B : Isolation fraction > 0.3 and $\not\!\!E_T < 10$ GeV
- Region C : Isolation fraction > 0.3 and $\not\!\!E_T > 20$ GeV
- Region D : Isolation fraction < 0.1 and $\not\!\!E_T > 20$ GeV

Region D is the $W \rightarrow \mu\nu$ signal region and the others contain mostly QCD background events. Based on the assumption of no correlation between isolation and

$\not\!\!E_T$ in the QCD background, the background contribution to the signal region estimated to be

$$\frac{W \text{ Background}}{\#\text{ events in Region C}} = \frac{\#\text{ events in Region A}}{\#\text{ events in Region B}}. \tag{3.12}$$

This technique can be further improved by accounting for the fact that in addition to QCD background events these other regions also contain signal events and events from other background processes such as $Z \to \mu\mu$ and $W \to \tau\nu$. Removing the non-QCD contributions to the event observed in the region A, B, and C, the corrected QCD background estimates are $0.71 \pm 0.36(\%)$ for CMUP events and $0.65 \pm 0.33(\%)$ for CMX events.

3.4.3 Cosmic Background

The signature of W event can be imitated by a cosmic ray when only one leg of the cosmic is reconstructed. Such an event may pass both Z veto and $\not\!\!E_T$ cut due to the transverse momentum imbalanced. The fraction of events due to cosmic rays which slipped through cosmic tagger is measured to be $0.10 \pm 0.07(\%)$ uncertainty using cosmic rich data samples.

3.5 $W \to \mu\nu$ Candidate Distributions

Figures 3.2 and 3.3 show the distributions of muon p_T versus $\not\!\!E_T$ in the CMUP and CMX candidate event samples. The $W \to \mu\nu$ signals appear along the diagonal. Figure 3.4 is the two dimensional distribution for muon track ϕ versus η for all $W \to \mu\nu$ candidates (CMUP + CMX). The events map out the geometrical volumes of the muon detectors used in this analysis.

Figures 3.5, 3.6 and 3.7 show the comparison of the the distributions of muon p_T, $\not\!\!E_T$ and M_T between data and simulation for events passing W selection requirements. The spectrum in $W\gamma \to \mu\nu\gamma$ Monte Carlo is shown with 100 times magnified. Since the final state radiation from the muon is the major contribution in $W+\gamma$ processes and muon p_T is greater than 5 GeV in generation (see Section 5.1), the muon p_T spectrum of $W\gamma$ simulation is shift to lower than that of $W \to \mu\nu$ simulation. Figure 3.8 shows the yield of $W \to \mu\nu$ candidates per inverse picobarn as a function of time. The drop at run 152616 is due to the L1 XFT trigger requirement. The L1 trigger efficiency changed before and after this run from $99.2 \pm 1.0(\%)$ to $96.5 \pm 0.6(\%)$.

3.6 W Acceptance×Efficiency Calculation

The acceptance is measured by applying the kinematical and geometrical selection criteria to the Monte Carlo event generator plus CDF detector simulation for the inclusive $W \to \mu\nu$ candidates. But for the $W\gamma$ Monte Carlo case, I have

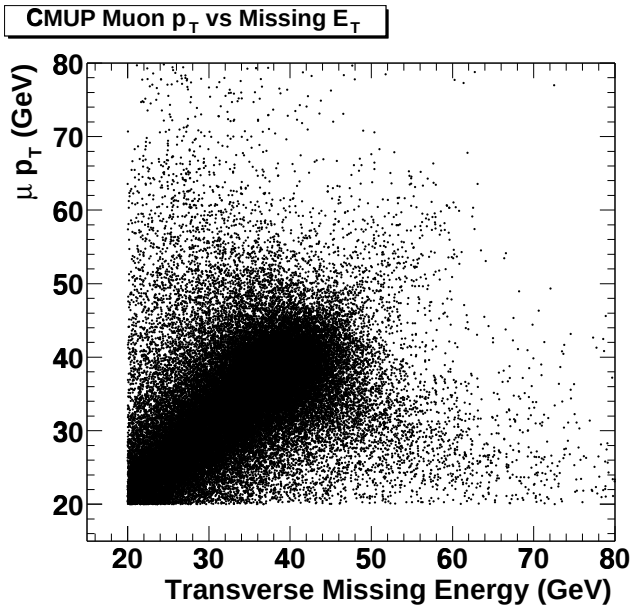

Figure 3.2: Muon p_T versus $\not\!\!E_T$ distributions for CMUP and $W \to \mu\nu$ candidate events. The $W \to \mu\nu$ signals appear along the diagonal.

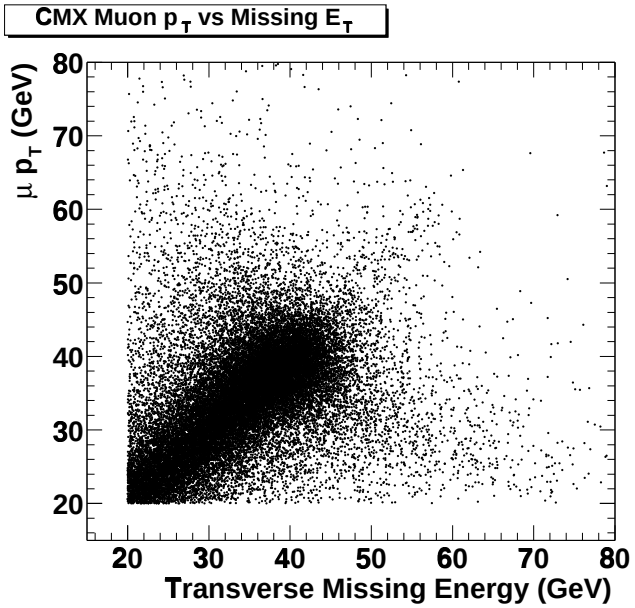

Figure 3.3: Muon p_T versus $\not\!\!E_T$ distributions for CMX and $W \to \mu\nu$ candidate events. The $W \to \mu\nu$ signals appear along the diagonal.

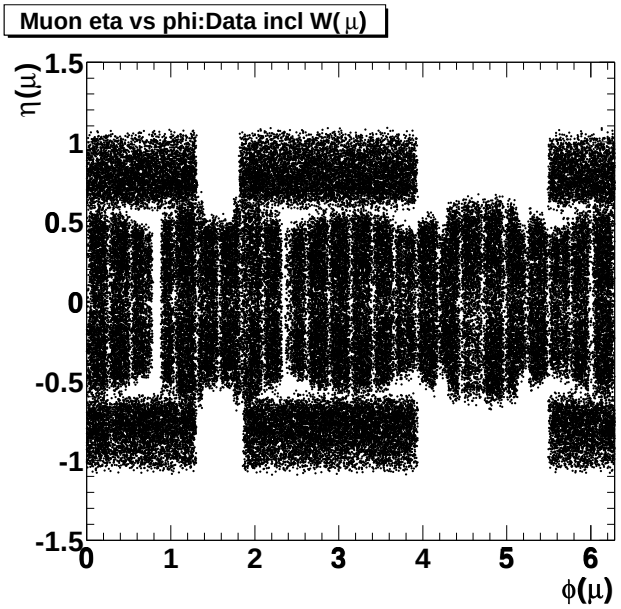

Figure 3.4: Muon track ϕ versus η distributions for CMUP and CMX $W \to \mu\nu$ candidate events.

to require kinematical cuts, $E_T^\gamma > 7$ GeV and $\Delta R(\mu,\gamma) > 0.7$,[1] for the final $W\gamma$ production cross section in order to avoid the divergence in the collinear region. I defined the 'acceptance×efficiency' $(A \cdot \epsilon)$ which is derived from all the cuts including the particle ID criteria as a numerator. The denominator is the number of the MC samples, but requires $|z_0| < 60$ cm cut due to the difficulty of measuring of $|z_0|$ efficiency for the plug electron W. Hence, the correction factor, the ratio of the efficiencies measured with Data to MC samples, are used to calculate the cross section of inclusive W and $W\gamma$, detailed in Chapter 7. $(A \cdot \epsilon)$ for inclusive W is compared with that for $W\gamma$ MC samples in Table 3.3.

3.7 $W \to \mu\nu$ cross section

I measured the $W \to \mu\nu$ cross section using 200 pb^{-1} of Run II data and compared it with a previous measurement using 72 pb^{-1} of Run II data [74]. The cross section is

$$\sigma \cdot B(p\overline{p} \to W \to \mu\nu) = \frac{N_W - N_{BG}}{(A \cdot \epsilon)_W \cdot \epsilon_{trig} \cdot \epsilon_{corr} \cdot \int \mathcal{L}\, dt}\ , \qquad (3.13)$$

where N_W is the number of $W \to \mu\nu$ candidate events and N_{BG} is the estimated number of background events. $(A \cdot \epsilon)_W$ is the kinematic and geometric acceptance

[1] Separation in $\eta - \phi$ plane between muon and photon defined in Section 4.3.

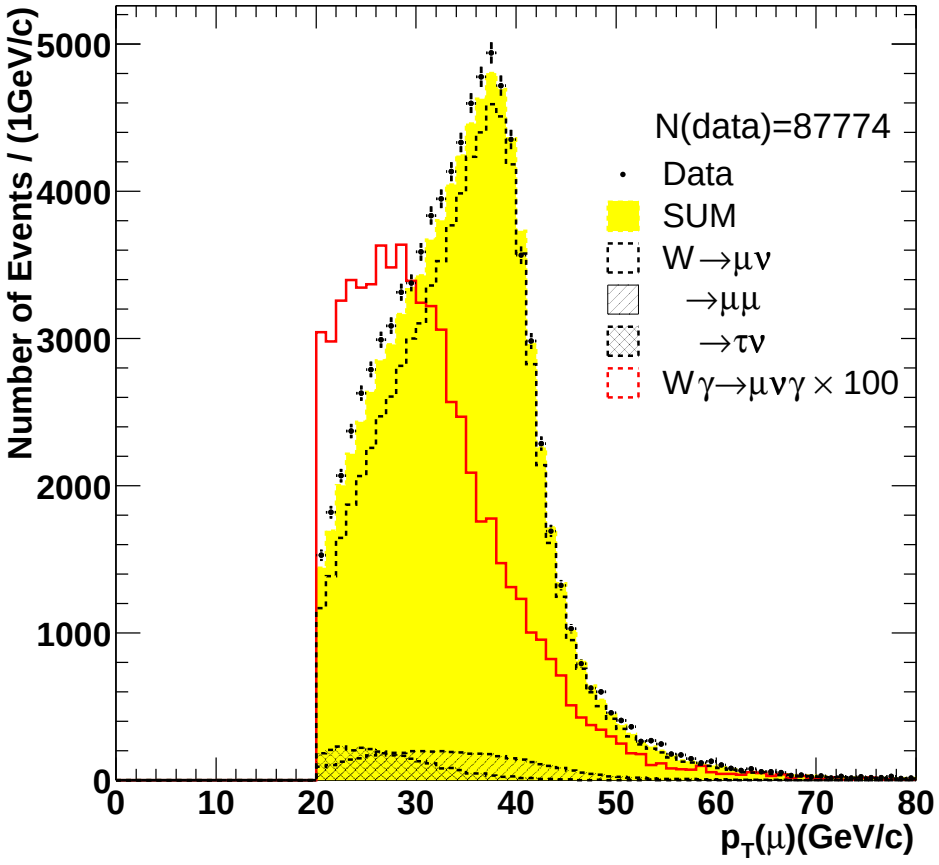

Figure 3.5: Muon p_T distributions in data (points), signal Monte Carlo (dashed line), backgrounds (hatched histogram) for $W \to \mu\nu$ events. The spectrum in $W\gamma$ Monte Carlo (red line) is magnified 100 times.

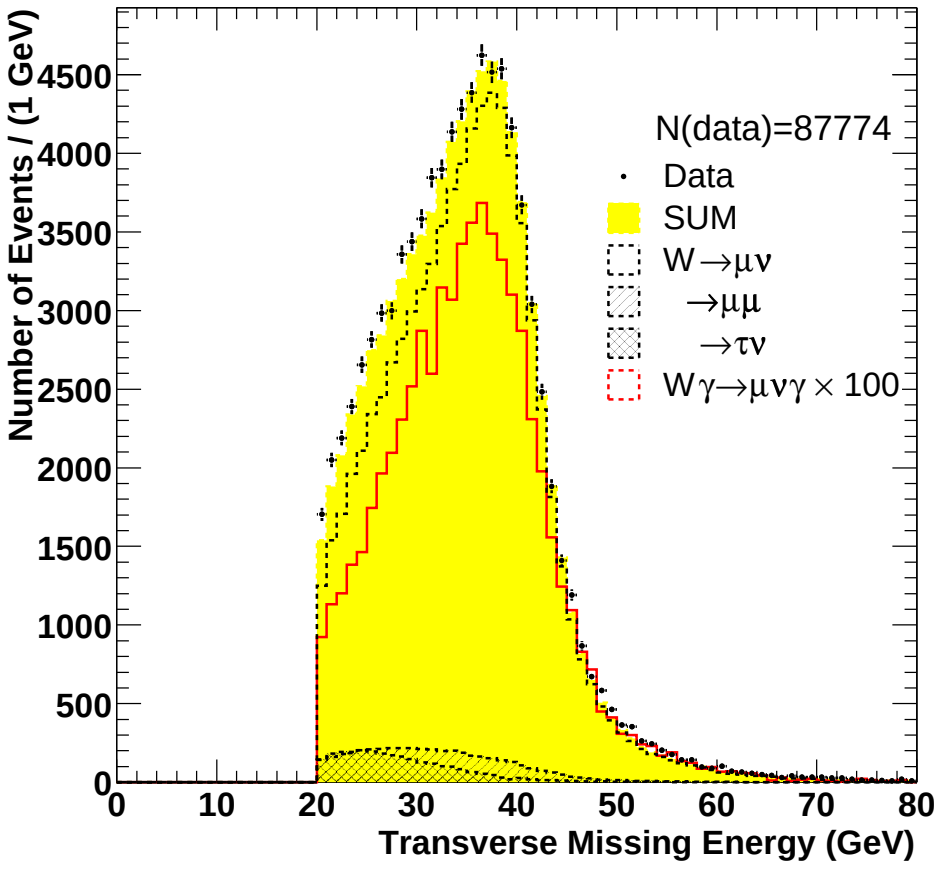

Figure 3.6: Transverse missing E_T distributions in data (points), signal Monte Carlo (dashed line), backgrounds (hatched histogram) for $W \to \mu\nu$ events. The spectrum in $W\gamma$ Monte Carlo (red line) is magnified 100 times.

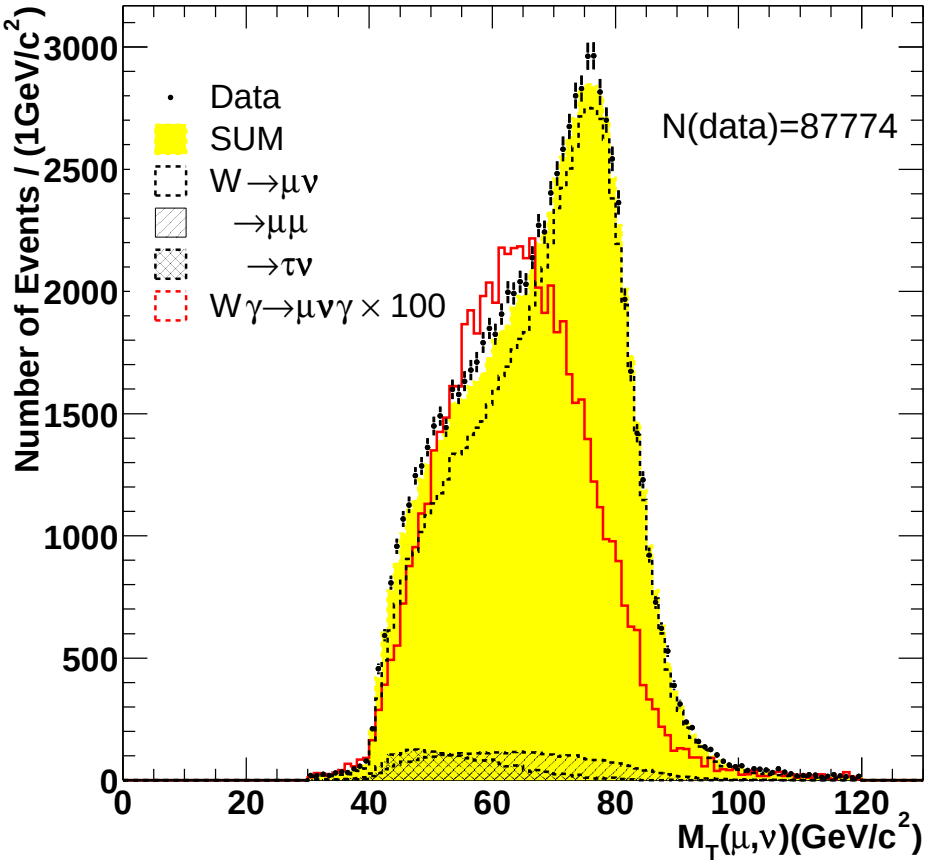

Figure 3.7: The transverse mass spectrum in data (points), signal Monte Carlo (dashed line), backgrounds (hatched histogram) for $W \to \mu\nu$ events. The spectrum in $W\gamma$ Monte Carlo (red line) is magnified 100 times.

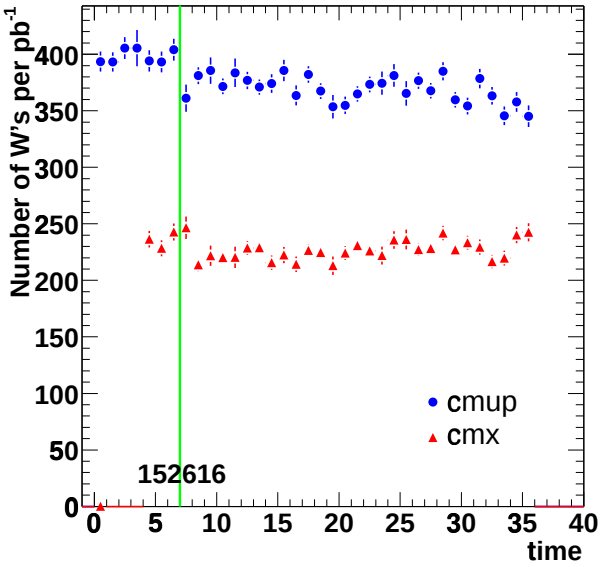

Figure 3.8: The yield of $W \rightarrow \mu\nu$ candidates per pb^{-1} as a function of time.

Table 3.3: Acceptance $\times$ efficiency $(A \cdot \epsilon)$ of the inclusive W and $W\gamma$ measured with inclusive W Monte Carlo and $W\gamma$ Monte Carlo samples. The statistical error only is taken into account. 'Muon' means the event fraction which has reconstructed muon, '$\not\!\!E_T$' passes the missing $E_T > 20$ GeV requirement. '$30 < M_T < 120$' is required to be the transverse mass within that region, and that makes $(A \cdot \epsilon)_W$ for the inclusive W selection. 'Photon ID' means the event required photon ID selection after finding W boson and the sepatation '$\Delta R > 0.7$' is required in addition. That makes $(A \cdot \epsilon)_{W\gamma}$ for the $W\gamma$ production.

Samples	inclusive W MC		$W\gamma$ MC	
Cut	CMUP(%)	CMX(%)	CMUP(%)	CMX(%)
Muon	13.87 $\pm$ 0.03	6.82 $\pm$ 0.02	7.21 $\pm$ 0.05	3.53 $\pm$ 0.03
$\not\!\!E_T > 20$ GeV	13.00 $\pm$ 0.03	6.42 $\pm$ 0.02	6.63 $\pm$ 0.05	3.26 $\pm$ 0.03
$30 < M_T < 120$	12.94 $\pm$ 0.03	6.39 $\pm$ 0.02	6.58 $\pm$ 0.05	3.24 $\pm$ 0.03
photon ID	-	-	1.70 $\pm$ 0.02	0.69 $\pm$ 0.02
$\Delta R > 0.7$	-	-	1.09 $\pm$ 0.02	0.49 $\pm$ 0.01

taken from Monte Carlo. ϵ_{trig} is the muon trigger efficiency and ϵ_{corr} is the scale factor of the detecting the muon from W decays using the event criteria detailed in Section 7.1 and 7.2. $\int \mathcal{L}\ dt$ is the integrated luminosity. Table 3.4 shows the input numbers for this equation and the associated errors.

Table 3.4: Summary of measured input parameters for the inclusive $W \to \mu\nu$ cross section calculations.

	CMUP	CMX
$(A \cdot \epsilon)_W$	0.129±0.0003	0.0639±0.0002
ϵ_{trig}	0.887±0.007	0.954±0.006
ϵ_{corr}	0.841±0.012	0.955±0.012
$\int \mathcal{L}\ dt$ [pb^{-1}]	192	175
N_W	56558	31216
b_W	9.50±0.44(%)	9.27±0.44(%)

For the CMUP candidates I measure

$$\sigma \cdot B(p\overline{p} \to W \to \mu\nu) = 2.77 \pm 0.01(\text{stat.}) \pm 0.07(\text{syst.}) \pm 0.18(\text{lumi.})[\text{nb}] \quad (3.14)$$

and for the CMX candidate I measure

$$\sigma \cdot B(p\overline{p} \to W \to \mu\nu) = 2.78 \pm 0.02(\text{stat.}) \pm 0.07(\text{syst.}) \pm 0.18(\text{lumi.})[\text{nb}]. \quad (3.15)$$

The $e + \mu$ combined W inclusive cross section using 72 pb^{-1} Run II data is,

$$\sigma \cdot B(p\overline{p} \to W \to \mu\nu) = 2.775 \pm 0.010(\text{stat.}) \pm 0.053(\text{syst.}) \pm 0.167(\text{lumi.})[\text{nb}]. \quad (3.16)$$

All measurements are consistent and are in agreement with the NNLO prediction of 2.687 ± 0.054[nb] [75].

Chapter 4

$W + \gamma$ Event Selection

After inclusive W bosons are selected, I require an additional isolated photon with $E_T > 7$ GeV in the event. The isolated photon variables in the central detector region are listed in Section 4.1, and the photon energy scale calibration is discussed in Section 4.2. In order to avoid collinear $W + \gamma$ events I applied a separation cut between the μ and γ as described in Section 4.3. After applying all requirements, I found 128 $W + \gamma$ candidate events. The event displays with the highest E_T^{γ} candidate are shown in Section 4.4.

4.1 Central Photon Selection Variables

The photon identification is similar to the electron identification except for the tracking requirements. The photons are identified in terms of 1) isolation in the Electromagnetic Calorimeter, 2) no track pointing at the cluster and 3) the shape in the chamber detector (CES) to reject π^0 backgrounds. For the photons in the barrel region with $|\eta| < 1.0$, I required the electromagnetic cluster to satisfy the followings:

Transverse energy The electromagnetic energy is required to have at least $E_T > 7$ GeV deposited in the central calorimeter. It is calculating as the electromagnetic cluster energy multiplied by $\sin\theta$, where the θ is measured using the polar angle between the cluster and z-vertex position of high p_T muon track extrapolated to the beam line. An electromagnetic cluster is made from a seed EM tower and at most one more shoulder tower in the same wedge. This is defined by two towers in pseudorapidity($\Delta\eta \simeq 0.3$) and one tower in azimuth ($\Delta\phi \simeq 15°$).

$E_{\mathrm{HAD}}/E_{\mathrm{EM}}$ The ratio of the total energy deposited in the hadron calorimeter to the total energy in the electromagnetic calorimeter. E_{HAD} must be relatively small.

Fiduciality The location of the electromagnetic cluster is required to be in a

good fiducial region of the central calorimeter, as defined by the position determined from CES shower information:

- The photon must lie within 21 cm of the tower center in the $r - \phi$ view in order for the shower to be fully contained in the active region. This corresponds to the cut $|X_{\rm CES}| < 21$ cm, where $|X_{\rm CES}|$ is the local coordinate of the calorimeter.
- The photon should not be in the regions $|Z_{\rm CES}| < 9$ cm, where the two halves of the central calorimeter meet, and $|Z_{\rm CES}| > 230$ cm, which corresponds to the outer half of the last CEM tower (tower 9), prone to leakage into the hadronic part of the calorimeter.

Isolation This variable defined as the ratio $E_T^{\rm iso}/E_T^{\rm cluster}$, here $E_T^{\rm iso} = E_T^{0.4} - E_T^{\rm cluster}$, where $E_T^{\rm iso}$ is the energy in a cone of radius $\Delta R = \sqrt{\Delta\eta^2 + \Delta\phi^2} \leq 0.4$ around the photon cluster excluding the photon cluster, and $E_T^{\rm cluster}$ is the energy in the photon cluster. ΔR is defined between the cluster centroid and the center of a candidate tower. The sum of the transverse energy within $\Delta R < 0.4$ around the photon candidate is typically higher for the background than for the signal, since the background is usually produced as part of a jet.

N3D : Number of associated charged tracks The number of tracks reconstructed in three dimension that point to the electromagnetic cluster is required to be essentially zero. Taking into account of the activity of the minimum bias energy, at most one track pointing at the photon cluster, whose track $p_T < 1 + 0.005 \times E_T$ GeV, is allowed.

Track Isolation This variable defined as the sum of the tracks p_T in a cone of radius $\Delta R \leq 0.4$ around the photon cluster centroid is less than $2.0 + 0.005 \times E_T$ GeV.

Average of CES $\chi^2_{\rm strip}$ and $\chi^2_{\rm wire}$ The pulse height shape in the CES detector is compared to the one obtained with test-beam data using a χ^2 test. The variable $\chi^2_{\rm strip}$ is the χ^2 test of the fit between the energy deposited on each of the 11 strips in z in the CES shower and the shape obtained using test beam data. An energy dependent correction is used in the calculation of the χ^2. A similar variable $\chi^2_{\rm wire}$ tests the energy deposition on the wires in the $r - \phi$ views.

The absence of 2nd CES strip/wire cluster This requires the absence of the secondary highest E_T electromagnetic cluster near the photon measured in both the wire and strip CES detectors. This suppress π^0 and multi-photon backgrounds.

$$E^{2nd}_{\rm CES} \times \sin\theta < 0.14 \times E_T \qquad \text{if } E_T < 18 \text{ GeV} \tag{4.1}$$

$$< 2.4 + 0.01 \times E_T \qquad \text{if } E_T > 18 \text{ GeV}. \tag{4.2}$$

I summarize the photon selection requirements in Table 4.1.

Figure 4.1 - 4.2 shows 'N-1' photon distributions, i.e., applying all photon ID cuts and $\Delta R(\mu,\gamma) > 0.7$ cuts except for the specific cut. Dots represent data and yellow histograms $W\gamma$ Monte Carlo scaled by the expected luminosity.

Table 4.1: A series of Photon Identification Cuts

Quantity	Purpose
$E_T > 7$ GeV	Good quality EM object
$E_{\rm HAD}/E_{\rm EM}$ <0.125×E $\|\|$ < 0.055 + 0.00045×E	Good quality EM object
$\|X_{\rm CES}\| < 21.0$ cm	Good fiducial region
$9.0 < \|Z_{\rm CES}\| < 230.0$ cm	Good fiducial region
Isolation $< 2.0 + 0.02 \times (E_T - 20.0)$ GeV (if E_T >20 GeV)	QCD rejection
Isolation $< 0.1 \times E_T$ GeV (if $E_T < 20$ GeV)	QCD rejection
N3D $\leq$1 (if N3D = 1, $p_T < 1 + 0.005 \times E_T$ GeV)	QCD rejection
Track Isolation $< 2.0 + 0.005 \times E_T$ GeV	QCD rejection
$\langle\chi^2_{\rm CES}\rangle = \left(\chi^2_{\rm wire} + \chi^2_{\rm strip}\right) / \ 2 < 20$	QCD rejection
2nd CES cluster E$\times \sin\theta < 0.14 \times E_T$ (if $E_T < 18$ GeV)	QCD rejection
2nd CES cluster E$\times \sin\theta < 2.4 + 0.01 \times E_T$ (if $E_T > 18$ GeV)	QCD rejection

4.2 Calibration

The energy of the photon is measured directly from the calorimeter response, and it will affect the $(A \cdot \epsilon)_{W\gamma}$. Therefore it is important to calibrate the resolution of the E_T^γ.

The energy scale of the photons using the $W\gamma$ Monte Carlo simulation program and a full simulation on the CDF detector is tuned using $Z \to ee$ events: Fitting the Gaussian function to the $Z \to ee$ invariant mass then determines the best value of the scaling factor shown in Figure 4.3. The energy of the photons in the Monte Carlo is scaled by 0.996± 0.03. Time dependency of the Z mass peak were checked in Figure 4.4. As they distribute about 91 GeV all around the run period, I didn't apply any run dependent calibration factors.

4.3 $W + \gamma$ Event Selection

After all photon selection cuts were applied, I made an additional cut:

Separation : $\Delta R(\mu,\gamma)$ An angular separation between the W decay lepton and the photon of $\Delta R(\mu,\gamma) = \sqrt{\Delta\eta^2 + \Delta\phi^2} > 0.7$. This cut is designed to suppress the contribution from radiative W decays.

93 CMUP muon $W\gamma$ candidate events and 35 CMX muon $W\gamma$ candidate events passed all the above requirements.

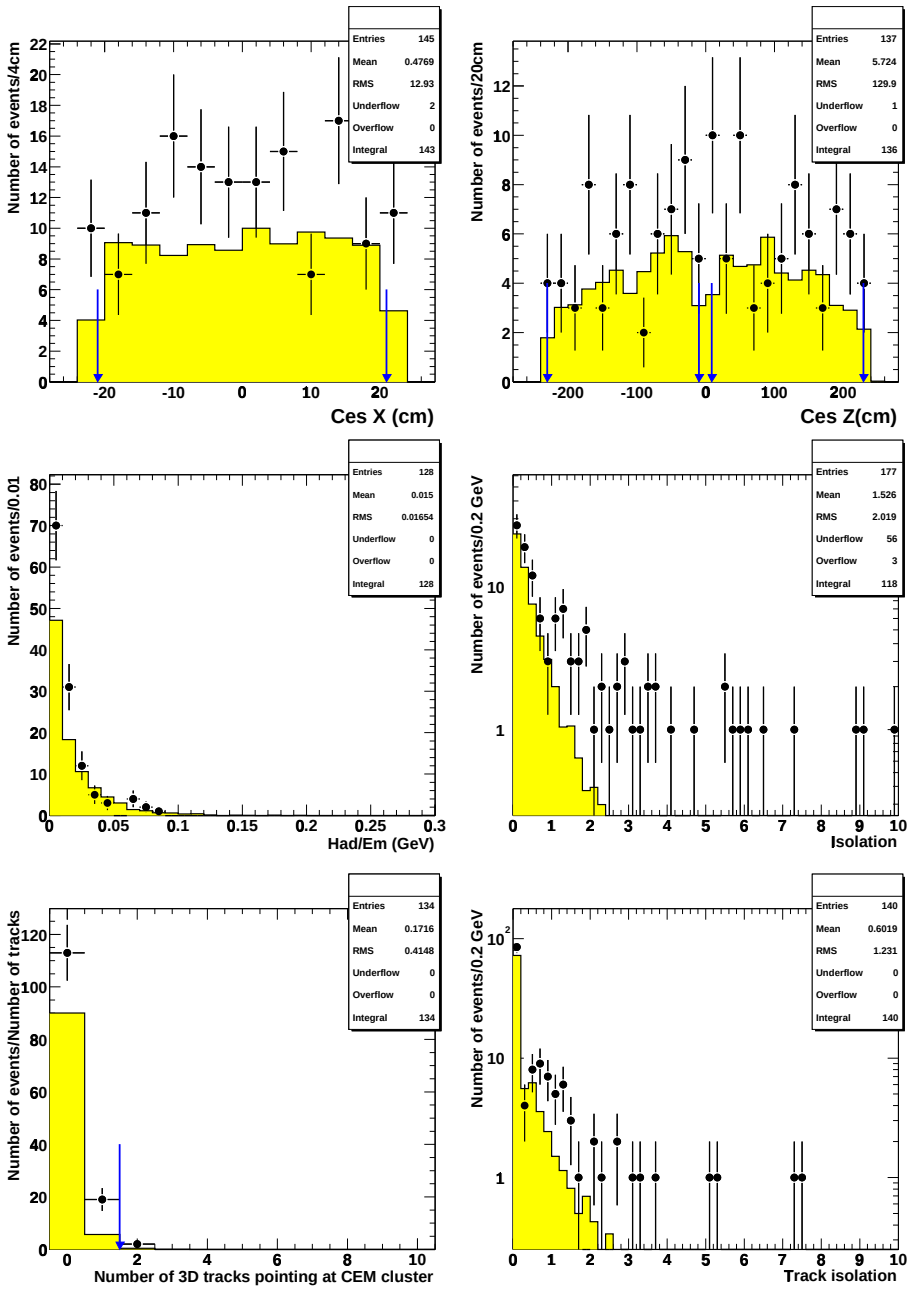

Figure 4.1: The photon variables used for the selection of the events. The photon in $W\gamma$ muon candidates (dots) and in the signal Monte Carlo (solid histogram) are used; for each variable all the selection criteria, but the one including the variable itself, are applied. The number of Monte Carlo events is normalized to the corresponding luminosity. The arrows show the value at which it has been cut to obtain the sample. For HAD/EM, Isolation, and track isolation, the cuts are sliding cut that depends on the energy of the cluster, and thus are not shown.

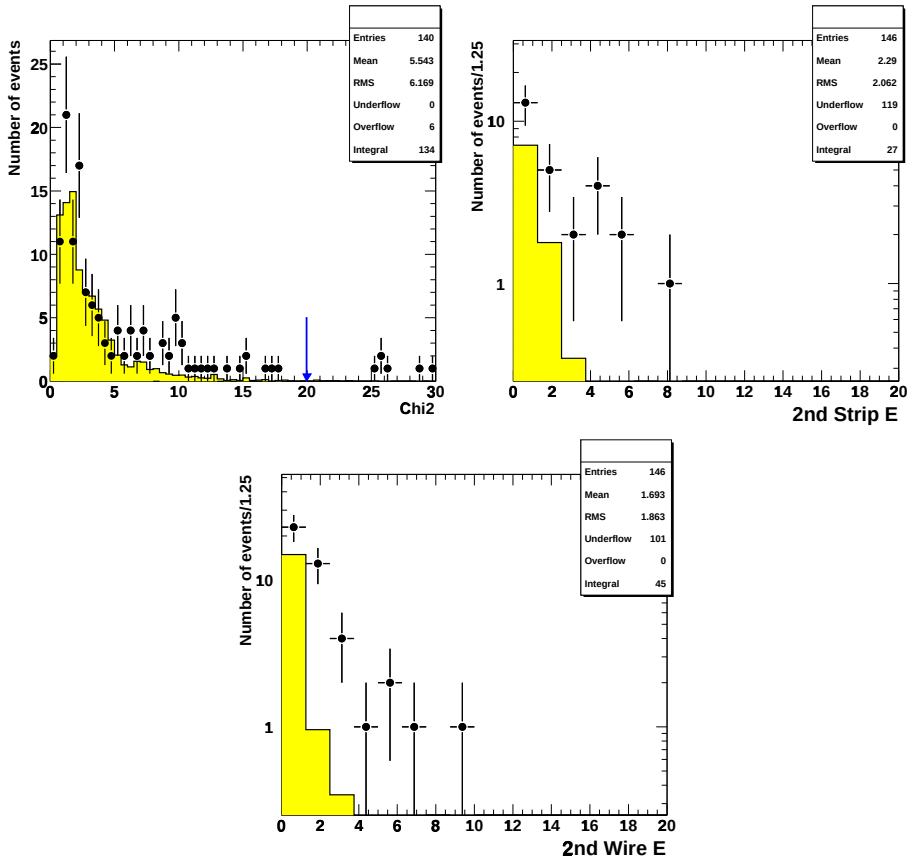

Figure 4.2: The photon variables used for the selection of the events. The photon in $W\gamma$ muon candidates (dots) and in the signal Monte Carlo (solid histogram) are used; for each variable all the selection criteria, but the one including the variable itself, are applied. The number of Monte Carlo events is normalized to the corresponding luminosity. The arrows show the value at which it has been cut to obtain the sample. For the 2nd strip/wire energies, the cuts are sliding cut that depends on the energy of the cluster, and thus are not shown.

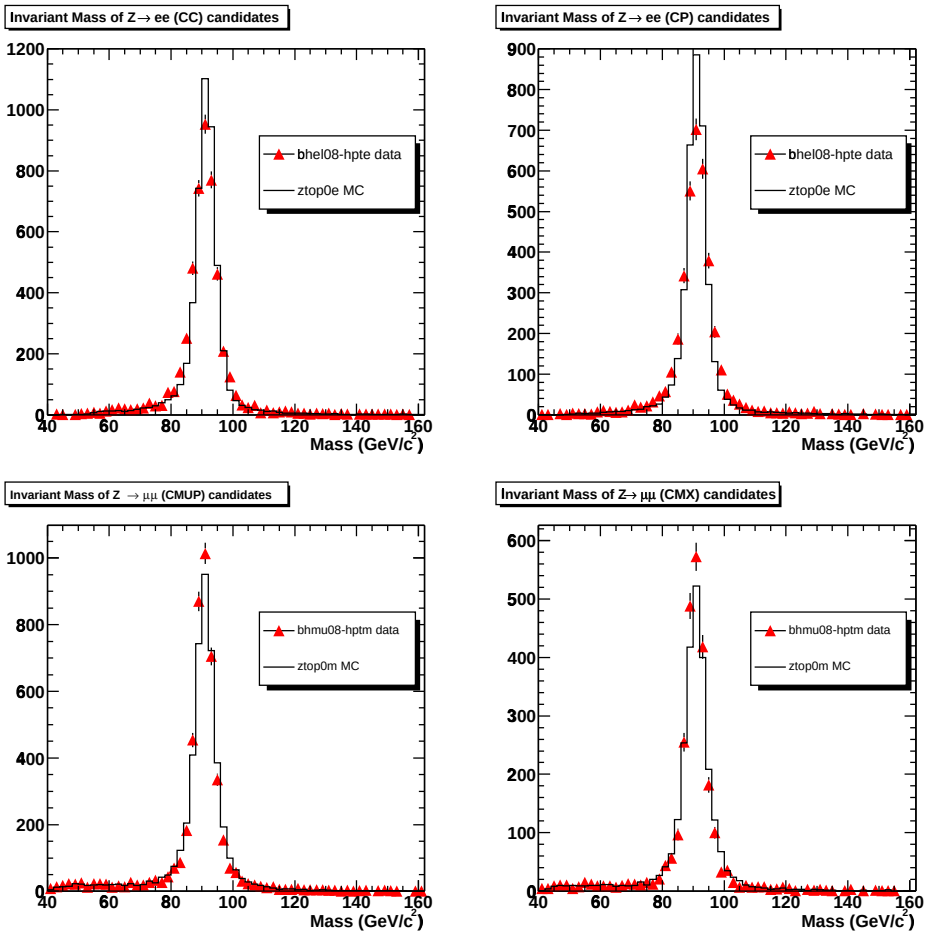

Figure 4.3: The invariant mass of the different Z decay channels using data and Monte Carlo simulation. Upper left is the central and central electron decay channel, upper right is the central and plug electron decay channel, lower left is the CMUP $Z \rightarrow \mu\mu$ decay channel and lower right is the CMX decay channel, respectively. Red triangles represent data and open histogram Z Monte Carlo simulation.

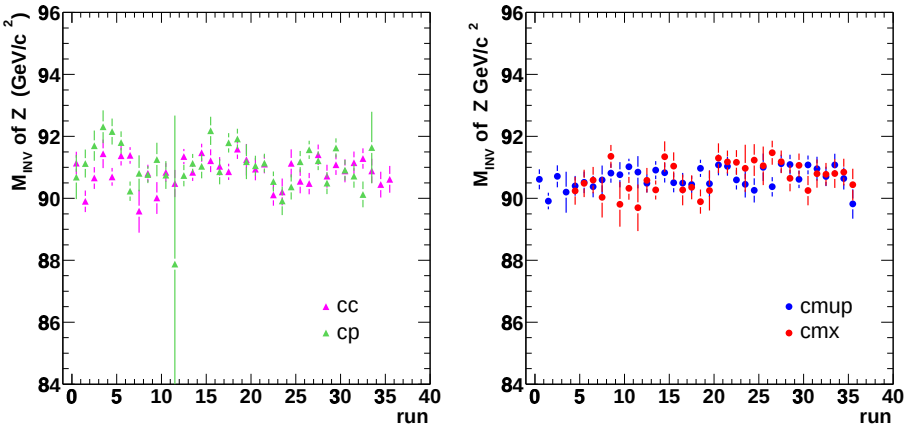

Figure 4.4: Time dependency of the invariant mass of $Z \to ee$ candidate events (left) and $Z \to \mu\mu$ candidate events(right). Drop in $Z \to ee$ distribution is due to the small statistics (accidentally I chose ~ 3 pb^{-1} for this bin).

4.4 Event Display for the highest $E_T(\gamma)$ Event

Figures 4.5 - 4.7 show the $W + \gamma$ event displays for the highest $E_T(\gamma)$ event in the CDF detector. This event has a high p_T muon (p_T = 52.9 GeV, ϕ = 151.1, η = -0.71), large missing E_T ($\not\!\!E_T$ = 36.8 GeV, ϕ = 335.1°) and a high E_T photon (E_T = 55.5 GeV, ϕ = 131.5°, η = -0.44), which construct the transverse mass of 66.5 GeV and the cluster transverse mass (See Section 4.5) of 146.6 GeV. The distance between the muon and photon is well separated with $\Delta R(\mu, \gamma) = 2.41$.

4.5 Cluster Transverse Mass

All the $W + \gamma$ production diagrams shown in Figure 1.1 interfere each other. These individual processes can not be rigorously separated, but using the cluster transverse mass we can considerably reduce the contamination of the final state radiation diagram and enhance s-channel diagram contribution.

The cluster transverse mass or so-called minimum invariant mass, $M_T(l\gamma, \nu)$, of the $W\gamma$ system is defined by [76],

$$M_T^2(l\gamma; \not\!\!E_T) = [(M_{l\gamma}^2 + |\mathbf{p}_{T\gamma} + \mathbf{p}_{Tl}|^2)^{1/2} + \not\!\!E_T]^2 - |\mathbf{p}_{T\gamma} + \mathbf{p}_{Tl} + \not\!\!E_T|^2. \quad (4.3)$$

This is the three-body mass of the $W\gamma$ system evaluated at the minimum value of the neutrinos longitudinal momentum with

$$\frac{\partial M(l, \gamma, \nu)}{\partial p_Z^\nu} = 0, \qquad \text{at} \quad p_{Z0}^\nu. \quad (4.4)$$

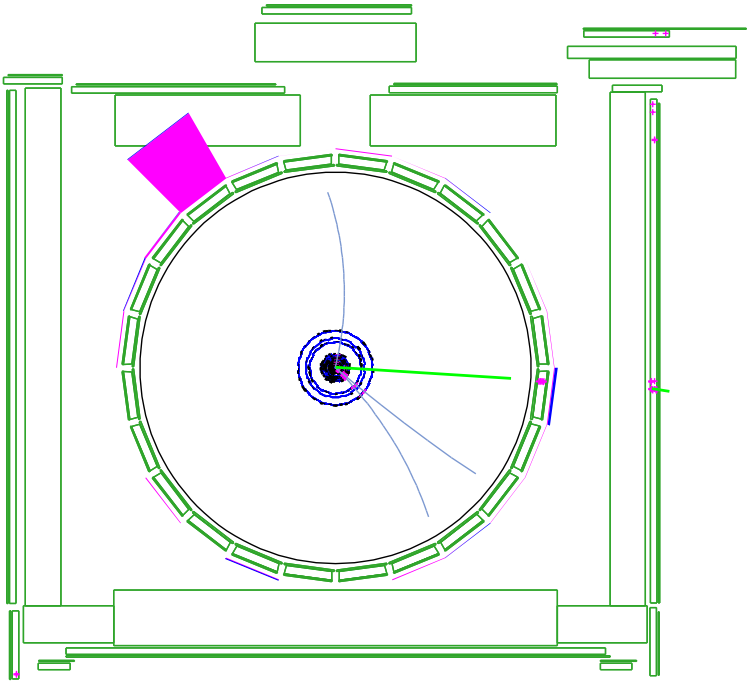

Figure 4.5: A COT event display of a muon $W\gamma$ event. Crosses in the right side on the picture represent hit in CMU and CMP chamber with a track pointing to the center of the detector ($p_T^{\mu} = 52.9$ GeV). A photon can be seen in the upper left as a red block on the outer circle ($E_T = 55.5$ GeV). The missing E_T is measured to the direction of lower left ($\not\!\!E_T = 36.8$ GeV).

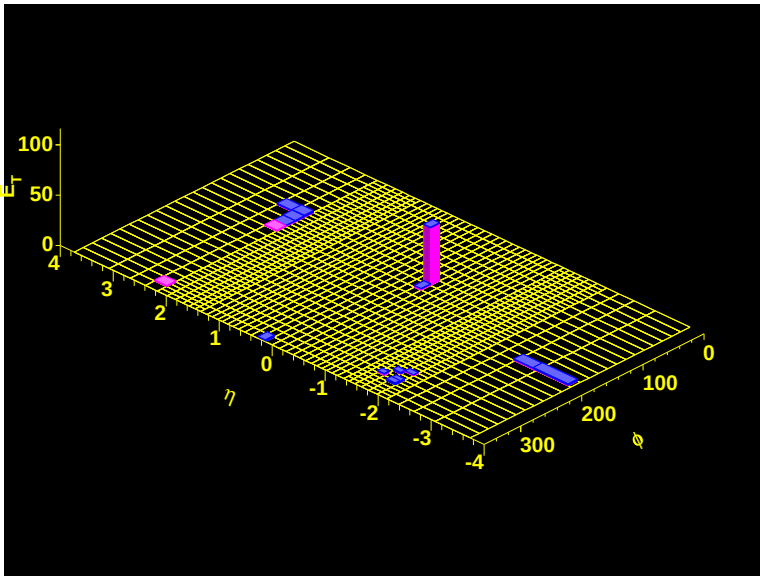

Figure 4.6: A LEGO event display of a muon $W\gamma$ event. This is an (η, ϕ) projection of the central calorimeter. The height of the block corresponding to the photon is directly related to its energy (E_T^{γ}=55.5 GeV).

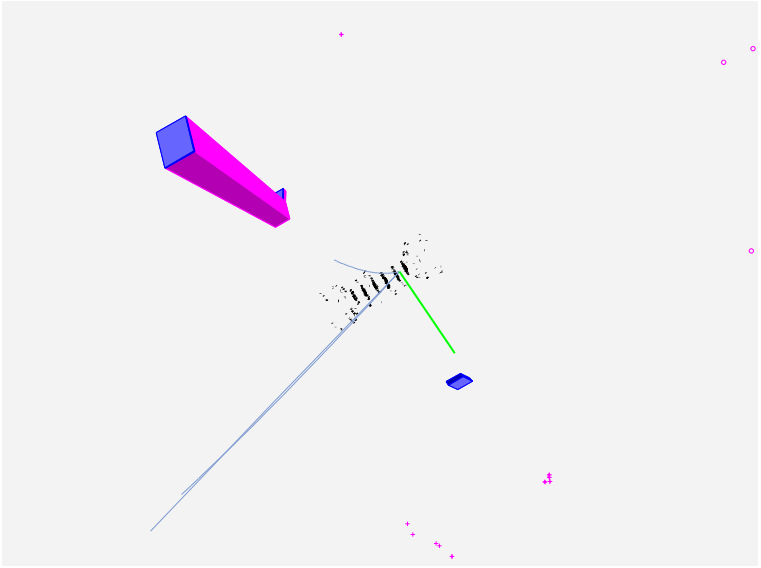

Figure 4.7: A 3D event display of a muon $W\gamma$ event. The crossses in the lower right side on the picture represent hit in CMP chamber with a track pointing to the center of the detector. The photon can be seen in the upper left as a red block. The black dots represent hit in the silicon detectors.

In other words, it is the transverse mass between the missing E_T and the sum of the 4-vector of the lepton and photon.

I categorize the $W + \gamma$ diagrams into two groups, 'A' and 'B', using parton level information from the `WGAMMA` Monte Carlo event generator as shown in Table 4.2. If I require $M(l, \nu) < M_W$ and $M(l, \nu, \gamma) \sim M_W$, I can say most of the events come from FSR $W\gamma$ diagrams. [1] On the other hand, if I require $M(l, \nu) \sim M_W$ and $M(l, \nu, \gamma) > M_W$, most of the events come from ISR and s-channel $W\gamma$ diagrams. The first scatter plot in Figure 4.8 shows the transverse mass of lepton and ν versus the cluster transverse mass of lepton, γ and ν system. The entries passing 'A' fulfillments denotes blue, and 'B' denotes red. The lower distribution in Fugure 4.8 is the projection of the upper distribution towards the y-axis, which can be separated at 90 GeV to get the events with higher purity of the s-channel diagram in the rough.

In this analysis, this variable has not been used in the selection of the $W\gamma$ sample due to the limit of the statistics of data, but it can be excellent cut parameter with high integrated luminosity in the future.

Table 4.2: The categories of the tree level $W + \gamma$ diagrams in terms of the invariant masses.

Category	M(l, ν)	M(l, ν, γ)	Diagrams	Illustrated in Figure 1.1
'A'	$< M_W$	$\sim M_W$	FSR	(d)
'B'	$\sim M_W$	$> M_W$	ISR, s-channel	(a), (b), (c)

[1] M_W is the mass of the W boson, 80.4 GeV.

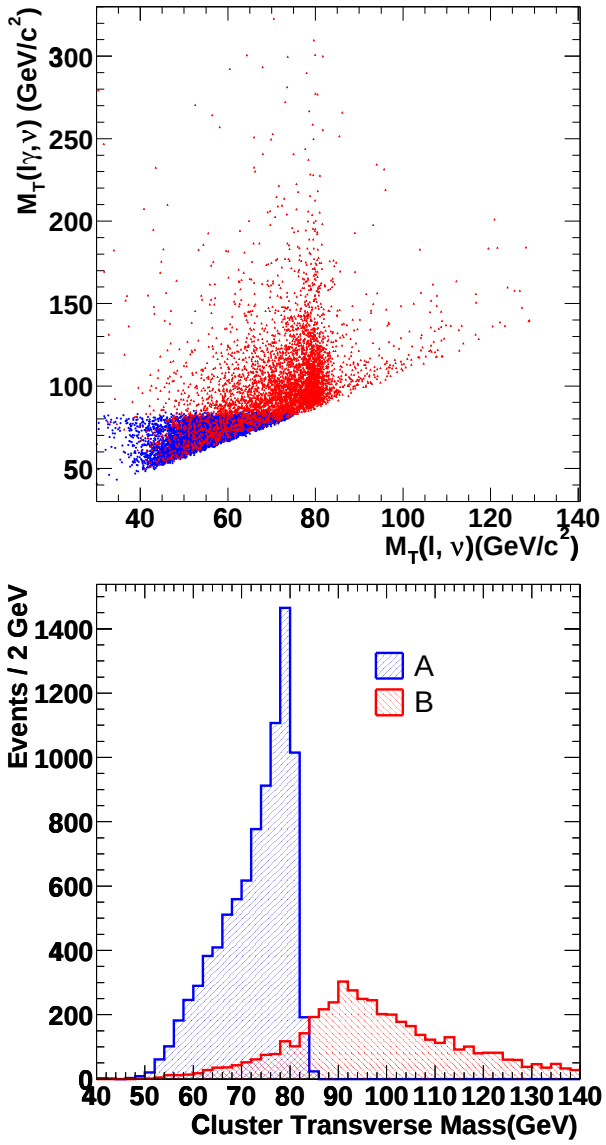

Figure 4.8: The scatter plot of the transverse mass of the lepton and ν system versus the cluster transverse mass of the lepton, γ and ν system (upper), and the lower spectrum is the cluster transverse mass which is the projection of the upper plot. Both of them are reconstructed with the parton-level Monte Carlo generator information. The requirement for the 'A' region (blue) is $M(l,\nu) < M_W$ and $M(l,\nu,\gamma) \sim M_W$, and for the 'B' region (red) is $M(l,\nu) \sim M_W$ and $M(l,\nu,\gamma) > M_W$.

Chapter 5

Monte Carlo Studies for $W\gamma$ Production

In this chapter Monte Carlo samples used to understand the data are described. The Baur's $W + \gamma$ and $Z + \gamma$ event process generators were used to predict the signal and background, and calculate the geometrical acceptance for the signal. There are other generators which can produce full or partical $W(Z) + \gamma$ production. Baur's $W + \gamma$ and $Z + \gamma$ generators are validated with them.

5.1 $W + \gamma$ Process Generators

Monte Carlo was used to estimate the detector acceptance and background contributions to $W+\gamma$ production. I used Baur's `WGAMMA` event generator, which is a matrix element generator provided by U. Baur and E.L. Berger [16]. It performs complete helicity calculations of all the tree level Feynman diagrams shown in Figure 1.1. It has the ability to decay the W boson into the electron, muon and tau channels. An analogous program, `ZGAMMA` is available for the generation of $Z + \gamma$ production with radiative Z boson decays [77].

The kinematic phase space integration is preformed with `VEGAS` [78] adaptive multidimensional integration code. Since `WGAMMA` and `ZGAMMA` return "weighted" events, they need to convert to "unweighted" events with the simple acceptance-rejection method [79]. During 10 passes through the available phase space, the integration grid is allowed to map the peaks in the cross section. Areas with higher cross section are given a higher density of grid points. The grid is then frozen for additional passes, and during event generation further calls are made to the integration routine with the frozen grid. During the event generation, all events are recorded and the maximum weight for the sample of events is determined. Finally, a subset of events with unit weights are selected by comparing individual event weights to the maximum weight. An event is stored if its weight, w, satisfies

$$w/w_{\max} > \mathcal{R}[0, 1], \tag{5.1}$$

where $\mathcal{R}$ [0, 1] denotes a random number uniformly distributed between 0 and 1.

The WGAMMA and ZGAMMA program includes mechanisms for introducing the anomalous coupling terms, $\Delta\kappa_\gamma$ and λ_γ for WGAMMA and h^i_{j0} for ZGAMMA , where i=[γ, Z] and j=[1, 4].

There are other Monte Carlo generators which can produce full or partial $W + \gamma$ production in $p\bar{p}$ collider listed below:

- The WGRAD program is a full NLO electroweak calculation of inclusive W boson production $q\bar{q}' \to W^\pm \to l^\pm\nu$, including the real photon contribution $q\bar{q}' \to l^\pm\nu\gamma$ [80]. In the latter case, both initial state radiation (ISR) from the incoming quarks, final state radiation (FSR) from the charged lepton, and interference terms are included. WGRAD includes no QCD corrections to W production and decay. Anomalous coupling terms can not be introduced into the WGRAD calculation. This program was written by U. Baur *et al.* and implemented in cdf software package [81]. ZGRAD is an analogous NLO electroweak program for inclusive Z boson production.

  The WGRAD calculation includes the real photon emission diagrams of WGAMMA, but is accurate down to low photon momenta. The program includes a photon collinearity cut, which is made on the angle between the charged fermion and the emitted photon in the parton-parton center of mass frame.

- The PYTHIA [82] Monte Carlo generator program for $W\gamma$ production includes matrix elements with the tree level u, t and s-channel diagrams and their interference terms, but does not properly include the inner bremsstrahlung diagram (See Figure 1.1), that means the final state radiation off the W or Z boson decay particles can be introduced, but the correct interference terms are not included. PYTHIA does not have a provision for introducing anomalous W and Z boson coupling terms.

- The CompHEP is a package for automatic calculations of elementary particle decay and collision properties in the lowest order of perturbation theory [83]. CompHEP contains all the terms for $W\gamma$ production in the Standard Model.

5.1.1 Consistency of Generators at the Parton Level

I compared WGAMMA generator with other $W + \gamma$ event generators and see the consistency of the WGAMMA Monte Carlo.

1. PYTHIA versus WGAMMA : As it is said in previous section, the FSR of $W + \gamma$ diagram can be turned off in PYTHIA generator. Figure 5.1 shows the scatter plot of two body invariant mass of μ and ν versus three body invariant mass of μ, ν and γ system in PYTHIA and WGAMMA . Comparing these two plots it is obvious that how FSR diagram works in $W+\gamma$ production. There

are no significant entries of $M(\mu, \nu, \gamma)$ around $M_W = 80$ GeV in PYTHIA . The reason is, the value of three body invariant mass of $M(\mu, \nu, \gamma)$ close to M_W in FSR $W\gamma$ diagram. On the other hand, in ISR and s-channel diagram, the value of two body invariant mass of $M(\mu, \nu)$ close to M_W, discussed in Section 4.5. This difference suggests that $\mu\gamma\not{E}_T$ events originating from radiative W decays can be separated by a $M(\mu\nu\gamma)$ cut from $W\gamma$ events which result in the same final state, but because of the invisibility of the neutrino, the cluster transverse mass works as a cut parameter instead.

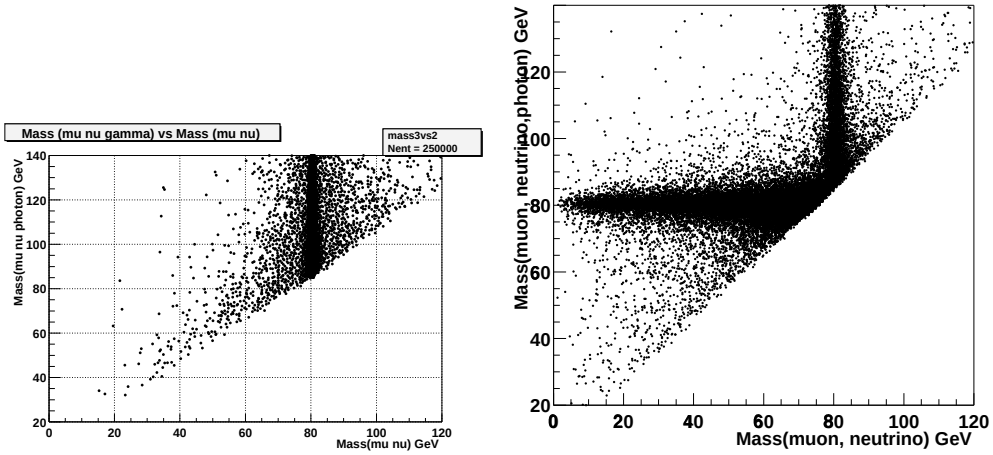

Figure 5.1: The invariant mass of three body system $M(\mu, \nu, \gamma)$ versus that of two body system $M(\mu, \nu)$ distributions using PYTHIA (left) and WGAMMA (right) $W + \gamma$ event generators. As the final state radiation is turned off in PYTHIA , there is no significant entries around W mass in three body mass.

2. WGRAD versus WGAMMA : Since WGRAD is an inclusive W production generator, not every event contains a photon. In order to compare WGRAD and WGAMMA , I select events which have (μ, ν, γ) in the final state for WGRAD Monte Carlo. This study will allow us to determine if the kinematical distribution using WGAMMA is sufficient for the photon E_T range above our experimental cut of 7 GeV.

   Figure 5.2 shows the muon p_T, transverse missing E_T, photon η and E_T, $\Delta R(\mu, \gamma)$, and two-body invariant mass of (μ, γ) system distributions in WGAMMA Monte Carlo overlayed with WGRAD Monte Carlo at the parton level comparison. ΔR distribution is peaked at low values due to the dominance of the Bremsstrahlung diagram. This is also seen in the invariant mass distribution in which the tail below 80 GeV arises from the Bremsstrahlung diagram while the peak at 90 GeV arises from the other processes. I find

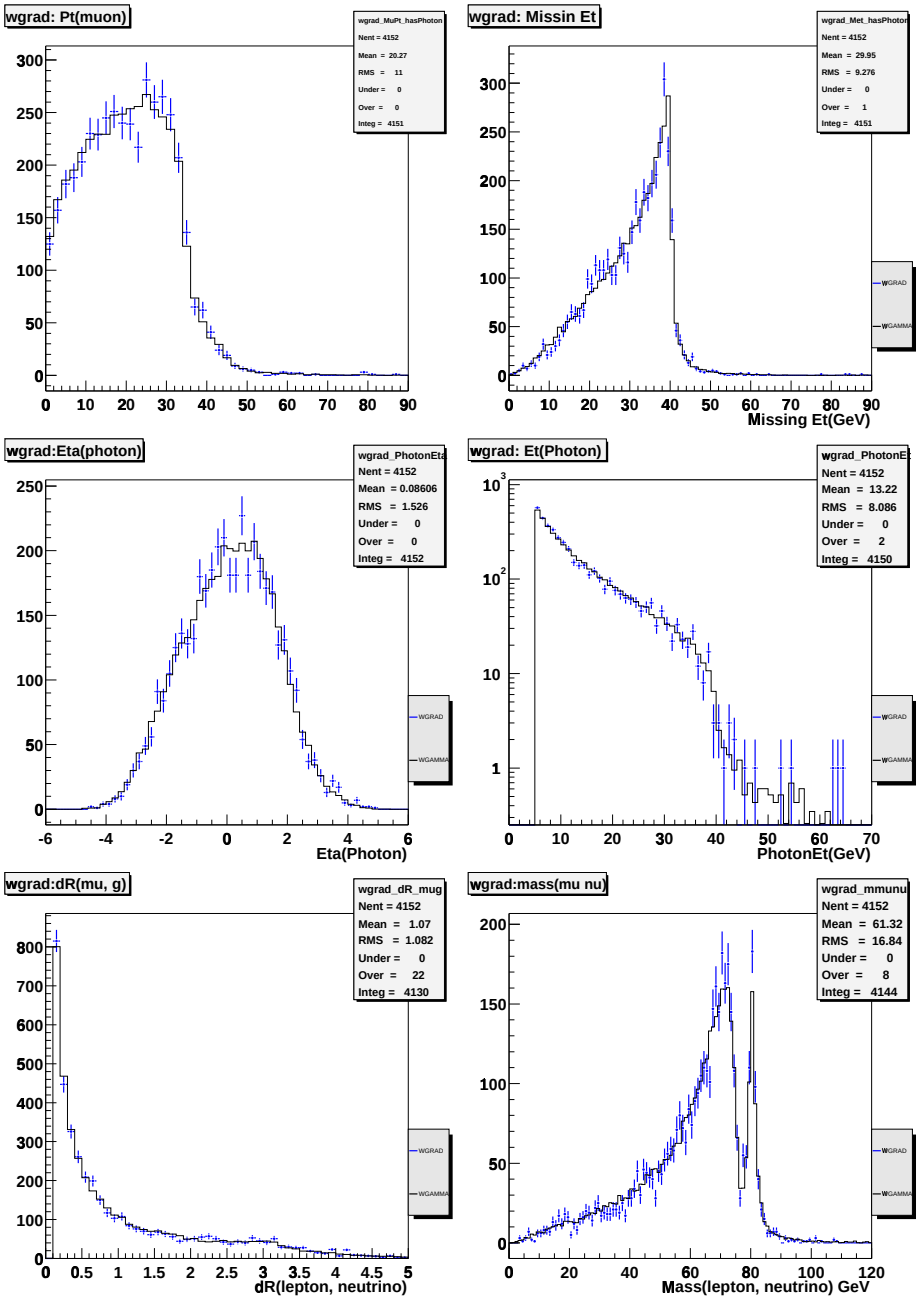

Figure 5.2: The muon p_T (upper left), $\not\!\!E_T$(upper right), photon η (middle left), photon E_T (middle right), $\Delta R(\mu, \gamma)$ (lower left), and two-body invariant mass of (μ, ν) system distributions at the parton level in `WGRAD` (blue) and `WGAMMA` (open histogram) Monte Carlo generators.

good agreement for all these distributions between WGRAD and WGAMMA . In the histograms all plots have been normalised to equal area. The matching distribution gives us confidence that the higher order electromagnetic corrections in WGRAD do not significantly change production in the regions of interest to our measurements, specifically low photon E_T and high ΔR. Having verified that WGAMMA is accurate for our purposes, and since WGRAD does not include the option of introducing anomalous couplings, we choose WGAMMA as our default generator.

3. Comparison of CompHEP and WGAMMA : As another check, I compared the predictions of the CompHEP and WGAMMA event generators. CompHEP contains all the terms for $W\gamma$ production in the Standard Model, and so a direct comparison between CompHEP and WGAMMA can be performed. Figure 5.3 show the photon E_T and η, two body invariant mass of (e, ν) system, $\Delta R(e, \gamma)$ distributions with WGAMMA and CompHEP at the generator level. There are in good agreement between the WGAMMA and CompHEP predictions.

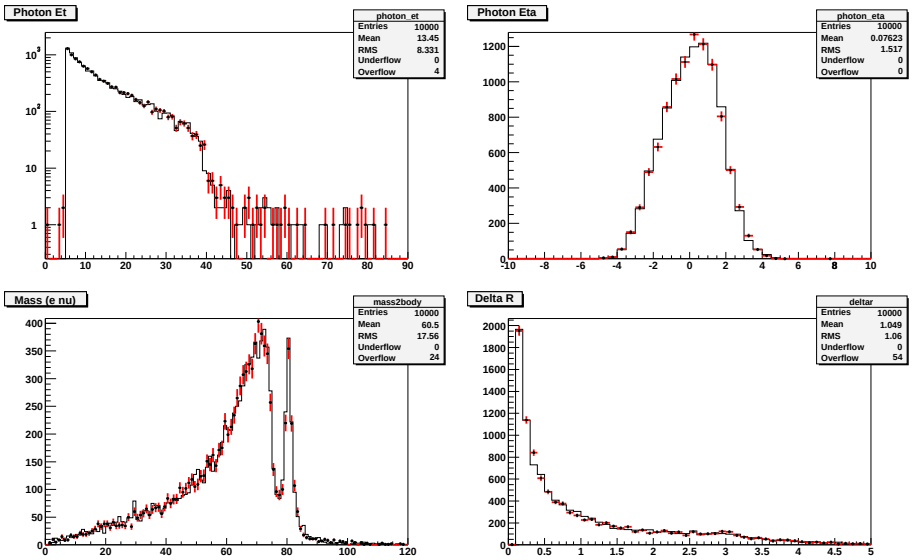

Figure 5.3: The photon E_T (upper left) and η (upper right), two body invariant mass of (e, ν) system (lower left), $\Delta R(e, \gamma)$ (lower right) distributions at the generator level with WGAMMA (open histogram) and CompHEP (red) Monte Carlo generators. I used $W\gamma \to e\nu\gamma$ channel as a comparison here, as it can be adopted to μ channel as it is very small difference between electron and muon channel.

I conclude that the WGAMMA event generator is the best options for the Standard Model predictions of $W + \gamma$ production. The parton level predictions for

$W+\gamma$ production have been cross-checked with WGRAD and CompHEP . In addition, WGAMMA can change the magnitude of the trilinear gauge couplings of photons to the W bosons. That is the reason we have chosen the Baur's WGAMMA generator as the $W+\gamma$ production generator in $p\bar{p}$ collisions.

5.2 Large Monte Carlo Sample Generation

$W+\gamma$ and $Z+\gamma$ events are generated with WGAMMA and ZGAMMA LO event generator. The electroweak parameters listed in Table 5.1 are selected for large sample generation. CTEQ5L is selected as the parton distribution function, Q_f^2 is the renormalization/factorization scale, and α_s is the fine structure constant. The value of $\sin^2\theta_W$ is fixed for both $W\gamma$ and $Z\gamma$ generation. While the mass of the $W(Z)$ boson is set to the PDG value for $W\gamma$ ($Z\gamma$) generation, the mass of the $W(Z)$ calculated from $\sin^2\theta_W = 1-(\mathrm{M}_W/\mathrm{M}_Z)^2$. This is why two values are listed for the mass of each vector boson. The Fermi constant, G_F, determined from the muon lifetime formula [84, 85].

Table 5.1: The electroweak parameters used for large Monte Carlo sample generation.

	WGAMMA ZGAMMA
Beam type	$p\bar{p}$
$\sqrt{s}$[TeV]	1.96
PDF	CTEQ5L
Q_f^2	$\hat{s}$ of parton collision
$\alpha_s(\mathrm{M}_Z)$	0.127
M(W) [GeV]	80.41 79.97
M(Z) [GeV]	91.625 91.1884
$\sin^2\theta_W$	0.231
$\alpha_{em}(\mathrm{M}(Z))$	1/127.51 1/128.96
$G_F[\mathrm{GeV}^{-2}]$	1.6637×10^{-5}
Γ_W [GeV]	2.103
Γ_Z [GeV]	2.514
M(top) [GeV]	175

$W+\gamma$ and $Z+\gamma$ events were generated requiring cuts listed in Table 5.2. These cuts are selected to well-cover the CDF detector acceptance and well below from the final cuts in Table 3.1 to avoid the colinear and infrared divergences. Since neither WGAMMA nor ZGAMMA contain any initial state gluon radiation in the calculation, a shower program must be incorporated to simulate this effect. They were therefore interfaced with PYTHIA 6.203 for gluon radiation, underlying event (See Section 7.4) and hadronization.

After the generation is performed, these samples are passed through the sim-

Table 5.2: Parton level cuts applied to WGAMMA and ZGAMMA generator. The transverse mass and cluster transverse mass cuts are applied to WGAMMA generator, and two-body and three-body invariant mass cuts are required to ZGAMMA generator.

Valuable	WGAMMA MC	ZGAMMA MC
$\|\eta(\gamma)\|$	<10.0	<10.0
$\|\eta(\mu)\|$	<10.0	<10.0
$\|\eta(\nu)\|$	<10.0	
$E_T(\gamma)$	> 5 GeV	> 5 GeV
$E_T(\mu)$	> 0 GeV	> 0 GeV
$E_T(\nu)$	> 0 GeV	> 0 GeV
$\Delta R(\mu, \gamma)$	> 0.2	> 0.2
Transverse mass $M_T(\mu, \nu)$	> 0 GeV	
Cluster transverse mass $M_T(\mu\nu; \not{E}_T)$	> 1 GeV	
Invariant mass $M(\mu^+, \mu^-)$		> 20 GeV
Invariant mass $M(\mu^+, \mu^-, \gamma)$		> 20 GeV

ulation program. This reproduces the physics of the interaction of the generated particles through the matter of the detector, their consequent decay and the amount of energy they deposit in each subdetector. In CDF a GEANT [86] parametrization of the detector is used, which contains all the information regarding the amount of material in the detector and the geometry of its components. The output of the simulation program has exactly the same structure as the actual data taken from real interactions.

5.3 Next to Leading Order Corrections

Since the WGAMMA and ZGAMMA event generators is based on leading order (LO) calculations, a next to leading order (NLO) correction factor must be applied to the generated events. In order to determine a correction factor, I used Baur's NLO programs [87] to calculate NLO QCD corrections (so-called k-factor) for LO $W+\gamma$ and $Z+\gamma$ processes. This calculate $\mathcal{O}(\alpha_s)$ for general CP-conserving $WW\gamma$ couplings.

The NLO calculation is done using narrow width approximation for the W decay. This simplifies the calculation to ignore Feynman diagrams in which the photon is radiated off the final state lepton line without violating electromagnetic gauge invariance. As a consequence, two corrections are applied based on the kinematics of the generated event. Using the three body invariant mass $M(l, \nu, \gamma)$ values, the generated events are separated into two groups, the inner bremsstrahlung diagrams ((d) in Figure 1.1) and initial state radiation and s-channels diagrams((a), (b) and (c) in Figure 1.1). The three body invariant

mass cut was chosen at 76 GeV/c^2 for $W\gamma$ events, and 86 GeV/c^2 for $Z\gamma$ events.

The inner bremsstrahlung term is corrected using the inclusive W or Z NLO correction, 1.36 for both of $W+\gamma$ and $Z+\gamma$ production. The initial state radiation and s-channel diagrams are corrected by taking the ratio of the NLO cross section to the LO cross section. The ratio of the binned cross sections for $W\gamma$ and $Z\gamma$ are shown in Figure 5.4. The ratios have been fitted with the

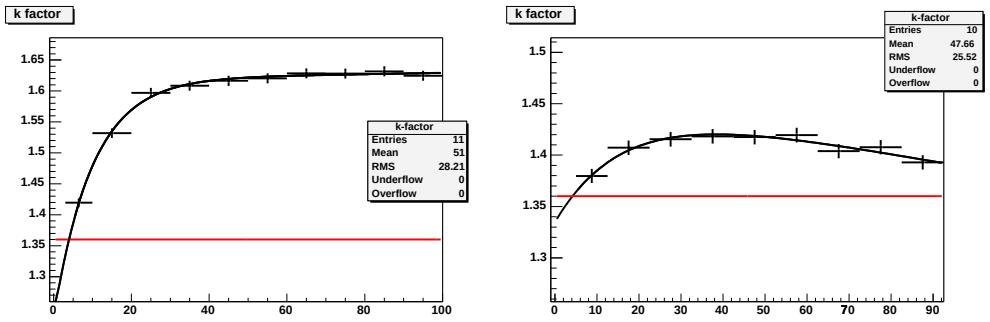

Figure 5.4: The k-factor distributions as a function of E_T^γ for $W\gamma$ (left) and $Z\gamma$ (right) Monte Carlo samples. The black line indicates the k-factor for the initial state radiation and s-channel diagrams ($W\gamma$ only). The red line indicates the k-factor for the inner bremsstrahlung terms in $W\gamma$ and $Z\gamma$ productions.

resulting functions,

$$k(E_T^\gamma; W\gamma) = 1.62 + 0.0001 \cdot E_T^\gamma - 0.386 \cdot \exp(-0.100 \cdot E_T^\gamma) \quad (5.2)$$

$$k(E_T^\gamma; Z\gamma) = 1.46 + 0.00073 \cdot E_T^\gamma - 0.125 \cdot \exp(-0.062 \cdot E_T^\gamma). \quad (5.3)$$

These k-factors are applied to LO events that have lepton invariant masses above the previously discussed cuts. The effective NLO corrections for events with photon $E_T > 7$ GeV and $\Delta R > 0.7$ are 1.38 for $W\gamma$ and 1.37 for $Z\gamma$.

The acceptance uncertainty due to unweighting events and k-factor measurements is 2% for $W\gamma$ muon channel and 2.5% for $Z\gamma$ muon channel. It is evaluated in the MC by looking at the effect on acceptance for my analysis cut at the parton level.

Chapter 6

Backgrounds

The main source of background in the $W\gamma \to \mu\nu\gamma$ process is the W+jet events which the jet is misidentified as an isolated photon. The rate of a jet to fake an isolated photon is measured in the jet data samples and cross checked with other samples detailed in Section 6.1.

Other source of backgrounds are the $Z+\gamma$ events where the Z is misidentified as a W and large missing E_T is observed due to the small coverage of the muon detector discussed in Section 6.2. Another small background is $W^+\gamma \to \tau^+\nu_\tau\gamma$, $\tau^+ \to \mu^+\nu_\mu\bar{\nu_\tau}$ process (W^- mode is charge conjugates of the mode). Due to the low p_T of the muons and small missing E_T, this background is expected to be very small (Section 6.3). These electroweak background contributions are estimated with Baur's `ZGAMMA` and `WGAMMA` Monte Carlos. The process which contain a real photon and jets faking as a W boson is considered as other source of background as well, discussed in Section 6.4.

6.1 Background from QCD

The contribution to the $W \to \mu\nu$ candidate sample from jets misidentified as an isolated photon is one of the most challenging to measure. Jets fragmenting into a hard π^0 or η mesons can be detected as an isolated photon in the CDF detector. In order for this background to be estimated in my candidates, the probability of a jet faking a photon is measured using jet triggered samples and other samples used to estimate the systematic uncertainties. In this study it is classified that any photons that is due to the decay products of a meson (*e.g.*, π^0, η or K_s^0) as "fake" and hard scattering process or radiated off a quark as "prompt", i.e., any photon candidates are categorized to either "fake" or "prompt".

6.1.1 Data Samples

The data samples used in this study are tagged `JET_20`, `JET_50`, `JET_70` and `JET_100`, which corresponding to 20, 50, 70 and 100 GeV of E_T triggered samples

respectively. These samples were processed and reconstructed with the same version of the production used $W\gamma$ analysis.

The jet having highest E_T in event is excluded from this study in order to avoid any trigger biases, thus at least two jets have $E_T > 7$ GeV. The jets are labeled according to their $E_T^{\rm jet}$. The "1st" jet refers to the highest E_T jet, the "2nd" jet refers to the 2nd highest E_T jet, and so on. The events where the jets are separated by $\Delta R(i_{\rm th}, j_{\rm th}) > 0.8$ from all other jets are used in this study in order to avoid the overlap of the jet cones each other.

The series of the photon selection cuts listed in Table 4.1 are required to the jet samples to estimate the fake rate discussed below.

6.1.2 Definition of Fake Rate

The number of background events from jets faking as photons in the $W\gamma$ candidates in given by

$$N_{BG}(E_T^\gamma) = \int_0^{N_W} P^W_{\rm jet\to\gamma}(E_T^{\rm jet}) \times dN_W/dE_T^{\rm jet} \times z(E_T^{\rm jet}, E_T^\gamma)\ dE_T^{\rm jet} \tag{6.1}$$

$$= \int_0^{N_W} P^{\rm jet}_{\rm jet\to\gamma}(E_T^{\rm jet}) \times \frac{dN_W/dE_T^{\rm jet}}{dN_{\rm jet}/dE_T^{\rm jet}} \cdot dN_{\rm jet}/dE_T^{\rm jet} \times z(E_T^{\rm jet}, E_T^\gamma)\ dE_T^{\rm jet} \tag{6.2}$$

where

- $P^W_{\rm jet\to\gamma}(E_T^{\rm jet})$ is the $E_T^{\rm jet}$ dependent probability of a jet faking a photon for jets in the W sample. Instead of directly measuring this probability, the fake rate in the inclusive jet samples $P^{\rm jet}_{\rm jet\to\gamma}(E_T^{\rm jet})$ is measured, detailed in Section 6.1.3. However, it is not a priori simple that this fake rate is the same in all physics samples, therefore the systematic error is assigned based on the relative fraction of quark and gluon jets in those samples discussed in Section 6.1.5.

- $dN_W/dE_T^{\rm jet}$ is the $E_T^{\rm jet}$ distribution in W events. The term $\dfrac{dN_W/dE_T^{\rm jet}}{dN_{\rm jet}/dE_T^{\rm jet}}$ cancels out if the $E_T^{\rm jet}$ distribution in jet sample is the same that in W sample. Figure 6.1 shows the $E_T^{\rm jet}$ distribution in W candidates, 2nd and sum of 3rd, 4th, 5th etc. ("345th") highest E_T jets in jet triggered samples. For the 345th jet in the jet samples, the $E_T^{\rm jet}$ distribution is very similar to that in the W sample, therefore the fake rate extracted with the 345th jet is used in this analysis, the 2nd is for the cross-check only. The detail is discussed in Section 6.1.5.

- $z(E_T^{\rm jet}, E_T^\gamma)$ is a function which gives the probability of a jet E_T to be measured as a photon E_T. This is measured in inclusive jet triggered samples as a function of $E_T^{\rm jet}$. The detail is discussed in Section 6.1.4.

The contributions are summed over all jets in inclusive W candidates used to select the $W\gamma$ candidate.

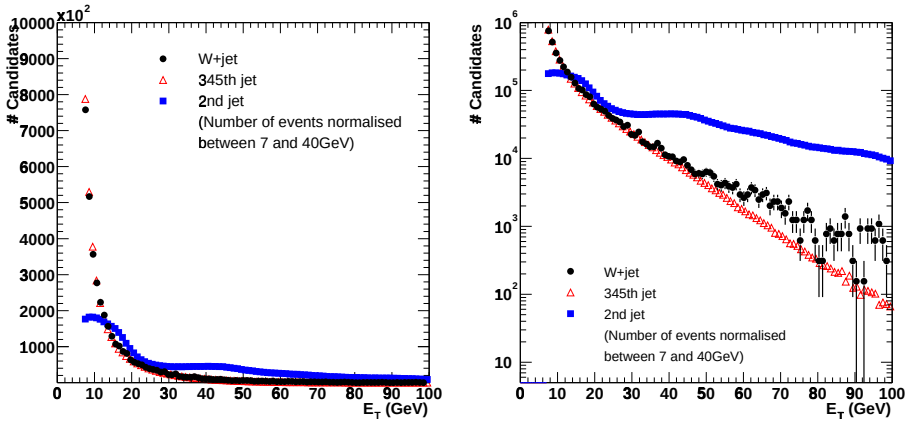

Figure 6.1: The E_T^{jet} distribution in the W sample (black points), the 2nd jet in the jet samples (blue squares) and the 345th jets in the jet samples (red open triangles).

6.1.3 Fake Probability

The measurement of $P_{\text{jet}\to\gamma}(E_T^{\text{jet}}) = N_{\text{jet}\to\gamma}/N_{\text{jet}}$ requires a sample which contains only jets and no prompt photons, but no such a dataset exists. The prompt photon contamination, F_γ, is estimated in the jet samples to be

$$F_\gamma = \frac{N_\gamma}{N_\gamma + N_{\text{jet}\to\gamma}} = \frac{N_\gamma}{N_{\gamma\ \text{candidate}}}, \tag{6.3}$$

where N_γ is the number of the prompt photons, $N_{\text{jet}\to\gamma}$ is the fake photons and $N_{\gamma\ \text{candidate}}$ is all photon candidates in event including prompt and fake photons. The fraction of the fake photons in the photon candidates is

$$F_{QCD} = \frac{N_{\text{jet}\to\gamma}}{N_{\gamma\ \text{candidate}}} = 1 - F_\gamma. \tag{6.4}$$

The fake probability of a jet is determined as

$$\begin{aligned} P_{\text{jet}\to\gamma}^{\text{jet}}(E_T^{\text{jet}}) &= \frac{N_{\text{jet}\to\gamma}}{N_{\text{jet}}} \\ &= \frac{N_{\gamma\ \text{candidate}}}{N_{\text{jet}}} \times \frac{N_{\text{jet}\to\gamma}}{N_{\gamma\ \text{candidate}}} \\ &= \frac{N_{\gamma\ \text{candidate}}}{N_{\text{jet}}} \times F_{QCD} \\ &= P_{\text{raw}}(E_T^{\text{jet}}) \times F_{QCD}, \end{aligned} \tag{6.5}$$

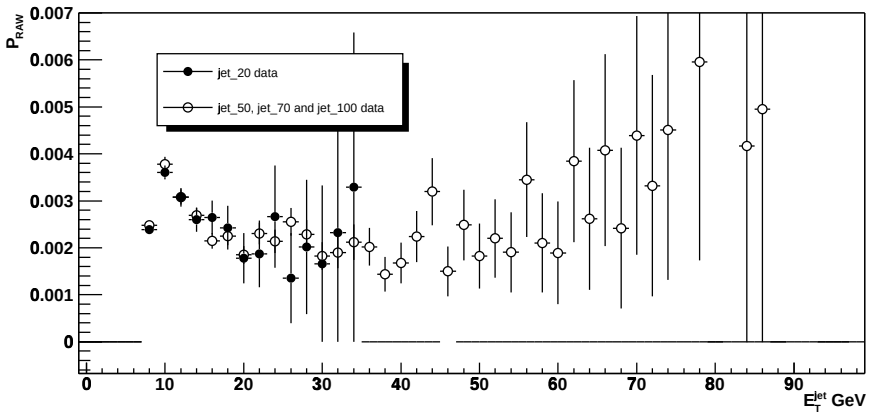

Figure 6.2: The fraction of photon candidates in jet samples, $P_{\rm raw}$, as a function of jet E_T comparing `JET_20` (full circle) and sum of `JET_50`, `JET_70` and `JET_100` (open circle) data samples. The 345th E_T jets are used.

where $P_{\rm raw}(E_T^{\rm jet})$ is the number of the photon candidates in jet samples, i.e. the fraction of photon candidates (including prompt and fake photons) in jet samples, called as 'raw fake rate'. $P_{{\rm jet}\to\gamma}(E_T^{\rm jet})$ is called as the 'true fake rate'. The distribution of $P_{\rm raw}(E_T^{\rm jet})$ is shown in Figure 6.2 for the `JET_20` and the sum of the `JET_50`, `JET_70` and `JET_100` jet samples. It's about 0.4% at the low $E_T^{\rm jet}$ and falls to 0.2% at $E_T^{\rm jet}$= 50 GeV. This raw fake rate can interprets as an absolute upper limit on the fake rate.

There are several methods which can measure the F_{QCD} as follows:

1. 'Transverse profile method' uses the transverse profile of each photon candidate in the CES detector, $\langle\chi^2_{\rm CES}\rangle$ (so-called CES method), that is compared to that measured for the electrons in a test beam in the same momentum range [88, 89], explicitly, $\langle\chi^2\rangle < 4/\langle\chi^2\rangle < 20$ fractions for both photons and neutral mesons are compared. This method has an advantage at low E_T where multiple photons from meson decays are more significantly separated at the CES radius.

2. Isolation versus $\langle\chi^2_{\rm CES}\rangle$ method : Calorimeter isolation and $\langle\chi^2_{\rm CES}\rangle$ are defined in Section 4.1. The background is usually produced as part of a jet and thus transverse energy around the photon candidate (i.e., the isolation) is typically higher for the background that for the signal. This method exploits the fact that there is no correlation between isolation and $\langle\chi^2_{\rm CES}\rangle$ for the background. This assumption has been verified in MC samples. In the isolation versus $\langle\chi^2_{\rm CES}\rangle$ parameter space, four regions is defined in Table 6.1 for $E_T^\gamma > 20$ GeV and $E_T^\gamma < 20$ GeV. Figure 6.3 shows the distribution using jet samples applying all the photon selection cuts

except for the isolation and $\langle\chi^2_{CES}\rangle$. Region C corresponds to the signal region and region D is a pure background region. Assuming that there is no signal in D and that the two observables are uncorrelated, the background in the signal region is predicted as

$$N_{BG} = \frac{N_B \cdot N_A}{N_D}, \tag{6.6}$$

and the fraction of the background F_{QCD} is

$$F_{QCD} = \frac{N_{BG}}{N_C} = \frac{N_B \cdot N_A}{N_D \cdot N_C}. \tag{6.7}$$

Table 6.1: Cut values to define the regions used for the Isolation versus $\langle\chi^2_{\mathrm{CES}}\rangle$ method for two regions in E_T^γ.

	$E_T^\gamma > 20$ GeV		$E_T^\gamma < 20$ GeV	
A	$(\mathrm{iso}-2)/(E_T^\gamma-20) < 0.02$	$\langle\chi^2_{\mathrm{CES}}\rangle > 20$	$\mathrm{iso}/E_T^\gamma < 0.1$	$\langle\chi^2_{\mathrm{CES}}\rangle > 20$
B	$(\mathrm{iso}-2)/(E_T^\gamma-20) > 0.06$	$\langle\chi^2_{\mathrm{CES}}\rangle < 20$	$\mathrm{iso}/E_T^\gamma > 0.2$	$\langle\chi^2_{\mathrm{CES}}\rangle < 20$
C	$(\mathrm{iso}-2)/(E_T^\gamma-20) < 0.02$	$\langle\chi^2_{\mathrm{CES}}\rangle < 20$	$\mathrm{iso}/E_T^\gamma < 0.1$	$\langle\chi^2_{\mathrm{CES}}\rangle < 20$
D	$(\mathrm{iso}-2)/(E_T^\gamma-20) > 0.06$	$\langle\chi^2_{\mathrm{CES}}\rangle > 20$	$\mathrm{iso}/E_T^\gamma > 0.2$	$\langle\chi^2_{\mathrm{CES}}\rangle > 20$

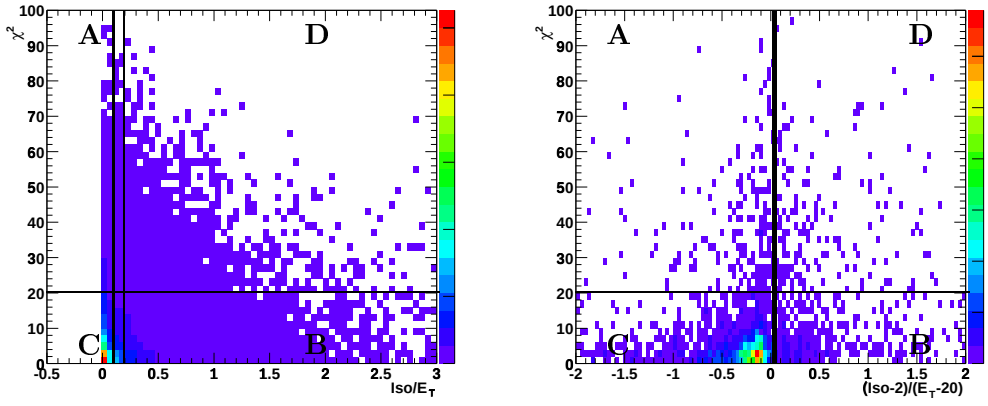

Figure 6.3: iso/E_T^γ (left) and $(\mathrm{iso}-2)/(E_T^\gamma-20)$ (right) versus $\langle\chi^2_{\mathrm{CES}}\rangle$ parameter space distribution in jet data samples.

3. 'Conversion method' detect the charge signal of photons converting in the solenoid coil by using the CPR detector (so-called CPR method) [88,90,91]. This relies on the fact that single photons have only one chance to pair produce, while multiple photons have more. The probability of conversion for a single, prompt photon is about P_γ^c=62% derived from the average radiator thickness, and probability of non-conversion is P_γ^{nc}=38%. If two photons resulting from a π^0 decay enter the same wedge, the probability that at least one of the converts is about $P_{\pi^0}^c = 1-(1-P_\gamma^c)^2$=86%, and probability of non-conversion is $P_{\pi^0}^{nc}$=14%. The number of observed photon candidates $N_{\gamma\ \text{candidate}}$ can be decomposed into the prompt photons (N_γ) and π^0 (N_{π^0}):

$$\text{Number of conversion} : N^c = P_\gamma^c \cdot N_\gamma + P_{\pi^0}^c \cdot N_{\pi^0} \tag{6.8}$$

$$\text{Number of non-conversion} : N^{nc} = P_\gamma^{nc} \cdot N_\gamma + P_{\pi^0}^{nc} \cdot N_{\pi^0}. \tag{6.9}$$

Inverting these relations gives us

$$N_\gamma = \frac{P_\gamma^c \cdot N_{nc} - P_{\pi^0}^{nc} \cdot N_c}{P_\gamma^{nc} - P_{\pi^0}^{nc}} \tag{6.10}$$

$$N_{\pi^0} = \frac{P_\gamma^{nc} \cdot N_c - P_\gamma^c \cdot N_{nc}}{P_\gamma^{nc} - P_{\pi^0}^{nc}}. \tag{6.11}$$

The prompt photon fraction is defined in Equation 6.3.

These three methods are compared and shown in Figure 6.4 and agree well within the statistical errors. At $E_T^\gamma > 40$ GeV only the CPR method is available. Between 15 and 20 GeV the CPR method gives an about 2-3 σ higher value than the other two methods. However, the CES method is well tested in this region and considered more reliable at low E_T^γ.

Whilst the CES and CPR method use the signal region and thus the same events, the Iso-CES method uses events outside the signal region to extrapolate into the signal region. For the final estimate we take the error weighted average of the CES and Iso-CES method for $E_T^\gamma < 40$ GeV and the CPR method for $E_T^\gamma > 40$ GeV. This combined F_{QCD} estimate is the fit with $\exp(-a \cdot x + b) + c$. The fit is shown in Figure 6.4 and the fitted parameters are $a = 0.161$, $b = 0.0668$ and $c = 0.124$. The data are seen to agree well with this fit.

The systematic error is taken to be the statistical error on the final fit. Figure 6.5 shows the difference of each F_{QCD} value to the final fit and the error on the final fit. All data are consistent within the statistical error on the fit. It ranges from about 5% at low E_T^γ to 15% at high E_T^γ. This corresponds to a fractional error on F_{QCD} of about 7% at low E_T^γ and 250% at high E_T^γ. This error is propagated to the total systematic error on F_{QCD}.

The ratio of the F_{QCD}'s to the average value and the systematic error of the individual methods are shown in Figure 6.5. The error is very large at high E_T^γ where there are no data available for the CES method and CPR method has a

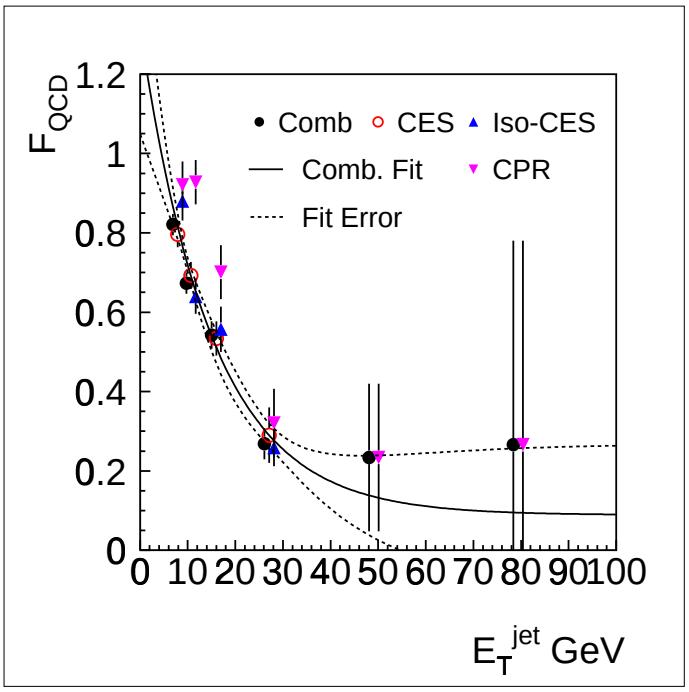

Figure 6.4: F_{QCD} as a function of $E_T^{\rm jet}$, as measured using the three independent methods for the 345th jets sample. "Comb" denotes the combination of the three methods as discussed in the text. The data are compared to the final fit (solid line) of the average of the "Iso-CES" and "CES" for $E_T^\gamma < 40$ GeV and the CPR for $E_T^\gamma > 40$ GeV. The upper and lower errors on the fit are aoso shown (dashed lines).

large statistical error. However, the fake rate is very small at high E_T^γ, this does not spoil the precision of the measurement.

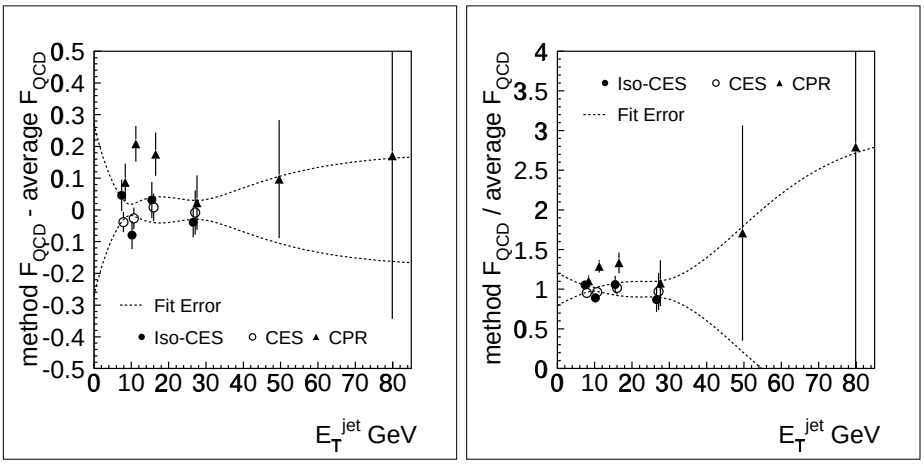

Figure 6.5: Shown is the difference (left) and ratio(right) of the F_{QCD} determinations (closed point: Iso vs CES, open points: CES, triangles: CPR) to the final value used and the statistical error (dashed lines) on the fit.

The final value of $P_{\mathrm{jet}\to\gamma}(E_T^{\mathrm{jet}}) = P_{\mathrm{raw}}(E_T^{\mathrm{jet}}) \times F_{QCD}$ is shown in Figure 6.6. The systematic uncertainties are discussed in Section 6.1.5.

6.1.4 Translation of $E_T^{\mathbf{jet}}$ to E_T^γ

The measured E_T^{jet} value must be translated into a E_T^γ value. In Equation 6.1 this function is called as $z(E_T^{\mathrm{jet}}, E_T^\gamma)$. Any photon candidate which passes the standard photon cuts, and is matched to a jet is selected in jet triggered sample, and the ratio of E_T^γ to E_T^{jet} is taken in Figure 6.7 a). E_T^{jet} is the energy in a cone of radius $\Delta R < 0.4$ around the jet cluster centroid. The distribution is fitted by Gaussian function. The E_T^γ dependence of the mean and resolution are shown in Figure 6.7 b) and c). z increases from 0.93 to 0.95 over the E_T^γ range of the measurement and the resolution decreases from 0.04 to 0.03. This slight E_T^γ dependence has a small effect on the final background prediction and is considered as a systematic error source.

As a consequence $z(E_T^{\mathrm{jet}}, E_T^\gamma)$ is a gaussian function with the average of the mean value of 0.934 and the resolution of 0.04.

6.1.5 Systematic Uncertainties on the Fake Rate

The following systematic uncertainties are taken into account:

1. The difference between the methods for the determination of the F_{QCD} detailed in Section 6.1.3.

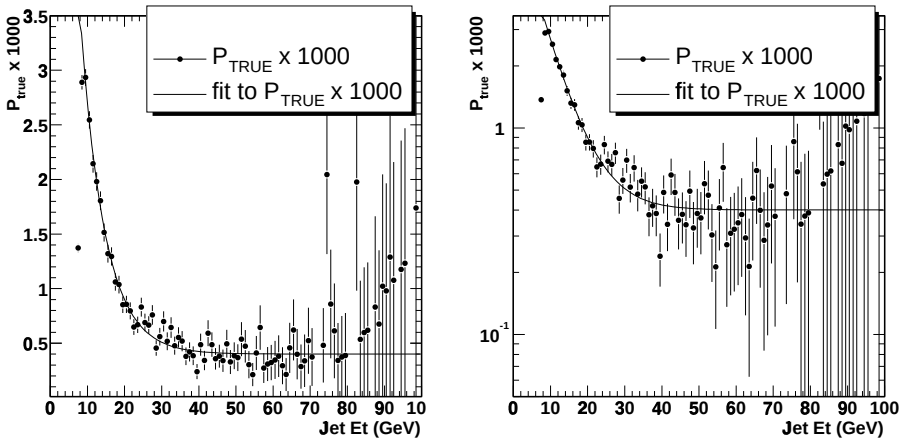

Figure 6.6: The true fake rate $P_{\mathrm{jet}\to\gamma}(E_T^{\mathrm{jet}})$ for the 345th jets sample in linear (left) and logarithmic (right) scale.

2. Quark-gluon mixture in W+jets compared to inclusive jets.

   One of the systematics would be canceled out if the E_T^{jet} distribution used to measure the fake rate is the same that in the inclusive W. However, jets are known to have different properties depending on whether they originate from a quark or a gluon: gluon have a softer fragmentation function, i.e., they tend to produce less hard particles than quarks in the hadronization [92]. Hence, the fake rate of a quark jet would be expected to be higher than that of a gluon jet naively.

   Figure 6.8 shows the fake rate of jets originating from quarks and gluons using a jet Monte Carlo sample. The fake rate for quark jets is an order of magnitude larger than that of gluons. It is important to ensure that the fraction of gluon jets is similar in the sample used to measure the fake rate and applied to. I compared the fraction of quark and gluon jets between '$W+1$ jet' and 'jet' Monte Carlo samples shown in Figure 6.9 as a function of E_T^{jet}. At low E_T^{jet} the two MC samples predict very similar gluon jet fractions, but quark jet fraction becomes dominant in the W+1 jet MC with increasing E_T^{jet}. At $E_T^{\mathrm{jet}} = 70$ GeV the fraction of quark jets is about 55% for the W+1 jet sample and only 35% for the jet sample. Beyond 70 GeV the W+1 jet sample behaves somewhat strange, but since there is no $W\gamma$ candidate at $E_T^{\gamma} > 70$ GeV I can neglect this issue.

   If I assume that the photon fake rate is indeed a factor of ten higher for quark jets than for gluon jets as the MC predicted, this difference causes a maximum difference of 20% at E_T^{jet}= 20 GeV. Higher (NLO) order process tend to increase the gluon fraction and would reduce the difference between the W+jet and the jet MC samples.

   At a consequence I do not apply any correction for this effect since the

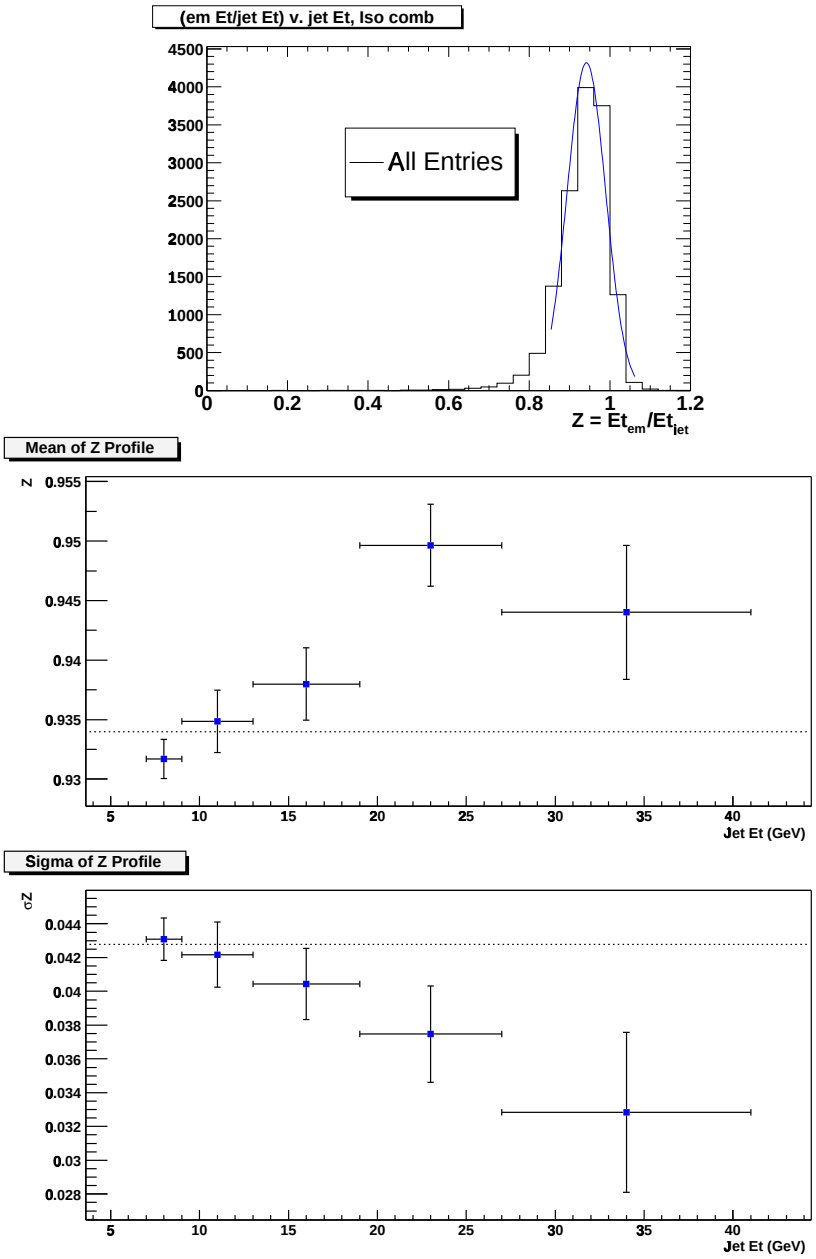

Figure 6.7: a) The distribution of $z = E_T^{\gamma}/E_T^{\text{jet}}$ for all events with Gaussian fit (upper). Dependence of b) the mean value and c) the resolution of z on Jet E_T (middle and lower). The dashed lines indicates the average values.

MC prediction on the individual quark and gluon fake rates unreliable, but include the full difference into the systematic uncertainties.

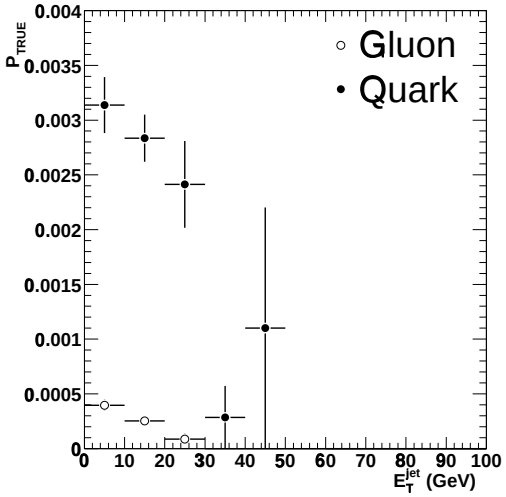

Figure 6.8: The fake rate of jets originating from quarks and gluons using a jet Monte Carlo sample.

3. The difference of the measurement of the true fake rate, $P_{\text{jet}\to\gamma}(E_T^{\text{jet}})$, between the 2nd and 345th jets.

   The 2nd jet has a different prompt photon fraction. The leading order diagrams for prompt photon production in $p\bar{p}$ collisions are indicated in Figure 6.10. In processes a) and b) photon is usually classified as 1st jet since the calorimeter response for photon is about 100% but 70% for jet, hence the 2nd jet will mostly not be photon. One of the next-to-leading order (NLO) QCD process for photon production is shown in Figure 6.10 c). In process c) the photon is radiated from one of the quark lines and will usually be the 3rd "jet", hence photons being classified as 2nd jet is suppressed. This causes a large difference in $P_{\text{raw}}(E_T^{\text{jet}})$ and F_{QCD} between the 2nd and 345th jets, but should not result in any significant difference for $P_{\text{jet}}(E_T^{\text{jet}}) = P_{\text{raw}}(E_T^{\text{jet}}) \times F_{QCD}$ if the procedure works properly. The measurements of $P_{\text{raw}}(E_T^{\text{jet}})$, F_{QCD} and $P_{\text{jet}}(E_T^{\text{jet}})$ are shown for the 2nd jet in Figure 6.11.

4. Measurement of the fake rate for an "EM object" rather than a Jet.

   One of the concerns in the fake rate measurement is the fragmentation of a jet into a photon candidate and how to translate E_T^{jet} to E_T^{γ}. This can be eliminated by using an electromagnetic object as denominator rather than a jet. Electrons are removed from the denominator to eliminate any sample

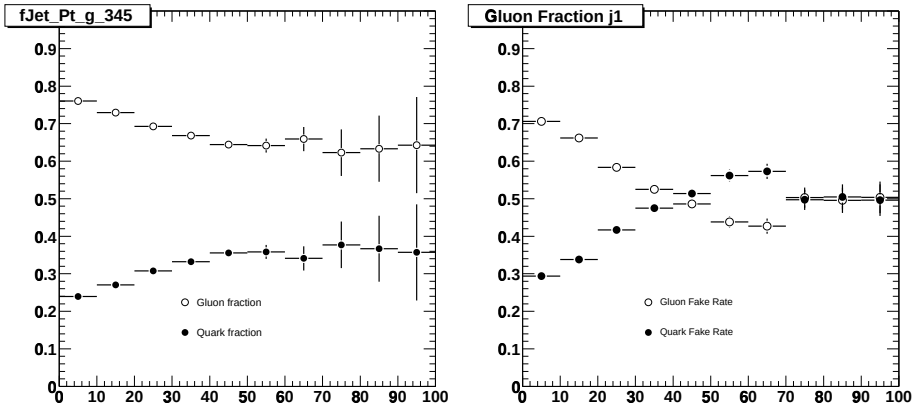

Figure 6.9: The fraction of quark and gluon originating jets compared between jet MC(left) and $W + 1$ jet MC(right) samples.

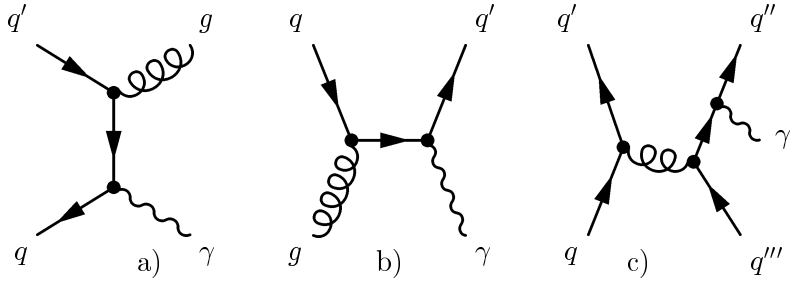

Figure 6.10: Typical Feynman diagrams for the photon production in $p\bar{p}$ collision. a) and b) shows the prompt photon production diagrams and c) a final state radiation example diagram.

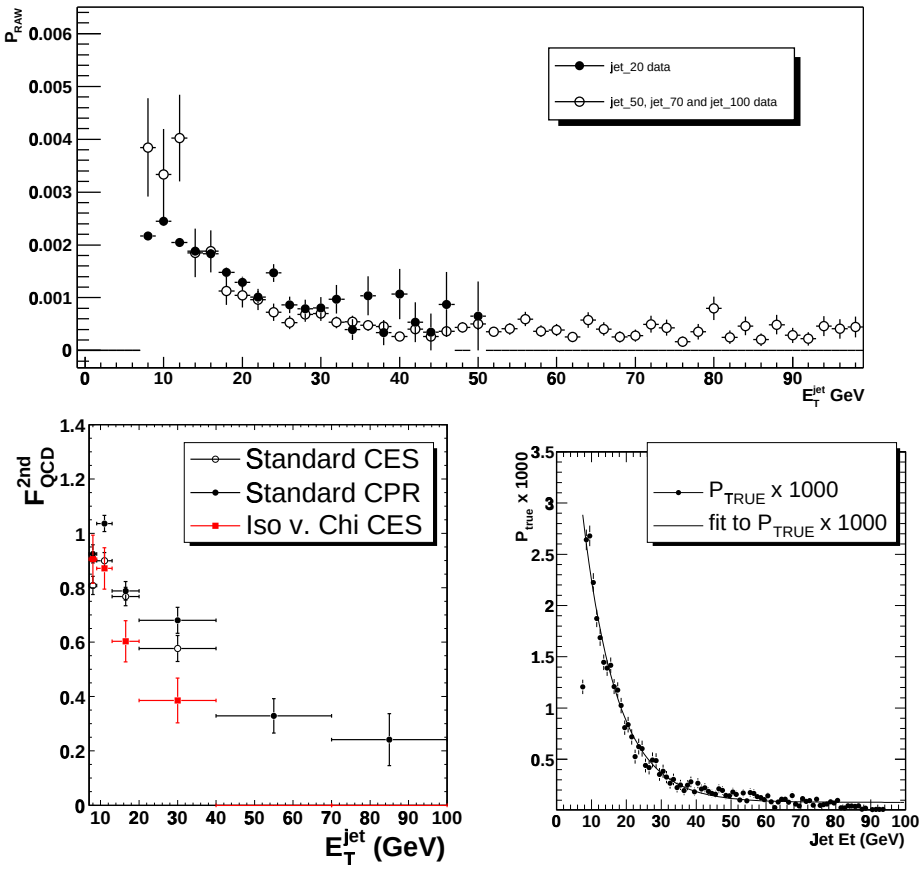

Figure 6.11: $P_{\rm raw}(E_T^{\rm jet})$(upper), F_{QCD}(lower left) and $P_{\rm jet}(E_T^{\rm jet})$ (lower right) as a function of $E_T^{\rm jet}$ for the 2nd jet.

dependence and highest E_T jets are excluded to avoid any trigger biases, then determined the corresponding quantities, $P_{\rm raw}(E_T^{\rm EM})$ and $P_{\rm EM}(E_T^{\rm EM})$. The results are shown in Figure 6.12. They are clearly different from the jet based fake rate, but not directly comparable since they are applied to the different object. F_{QCD} is basically the same as for the jet based method but it is determined as a function of E_T^{EM} instead of $E_T^{\rm jet}$.

I apply both fake rates to their respective samples, i.e., the jet fake rate is applied to every jet in the W sample and the EM fake rate is applied to any EM object in the W sample, then compare those final background predictions for the $W\gamma$ analysis shown in Figure 6.13.

The problem with the EM fake rate method is that it can be significantly contaminated by signal photons. Since the jet production rate is about three orders of magnitude larger than the photon production rate, the true photon component can be neglected when applying the fake rate to any jets. However, the contamination of photons into EM objects is significantly higher. I estimate this effect on the background in $W\gamma$ production. The resulting contribution is about 5 event at the $E_T^\gamma = 7$ GeV decreasing exponentially to about 0.03 events at the $E_T^\gamma = 40$ GeV for the $W\gamma$ candidates. Figure 6.13 shows the EM fake rate prediction after subtracting this ecpected contamination.

For the main result I use the fake rate method with jets since it has no problem of signal contamination and gives me higher statistical precision at high E_T^γ. The difference between the two methods is considered as an systematic uncertainty.

5. Effect of varying the fragmentation parameter.

   I changed the values of the mean and resolution of the translation, and it alter the fake rate by $\pm 3\%$.

The grand summary of the systematic error contributions is shown in Figure 6.14. Taking into account all above sources as uncorrelated, the systematic error is dominant by the F_{QCD} prediction about 30% at $E_T^{\rm jet} = 10$ GeV and 300% at the higher $E_T^{\rm jet}$. The true fake rate as a function of η and ϕ of jet is shown in Figure 6.15. Whilst the fake rate is independent of ϕ, I observe a significant dependence on η. This is explained by the photon geometrical requirement to be in the fiducial region of the CES.

6.2 Background from $Z\gamma$ Process

$Z + \gamma$ events where the Z is misidentified as a W (so-called one-legged Z) and large missing E_T is observed due to the small coverage of the muon detector. To estimate the contamination of this background, I generated $Z + \gamma \to \mu^+\mu^-\gamma$ process with Baur's `ZGAMMA` event generator with the electroweak parameters

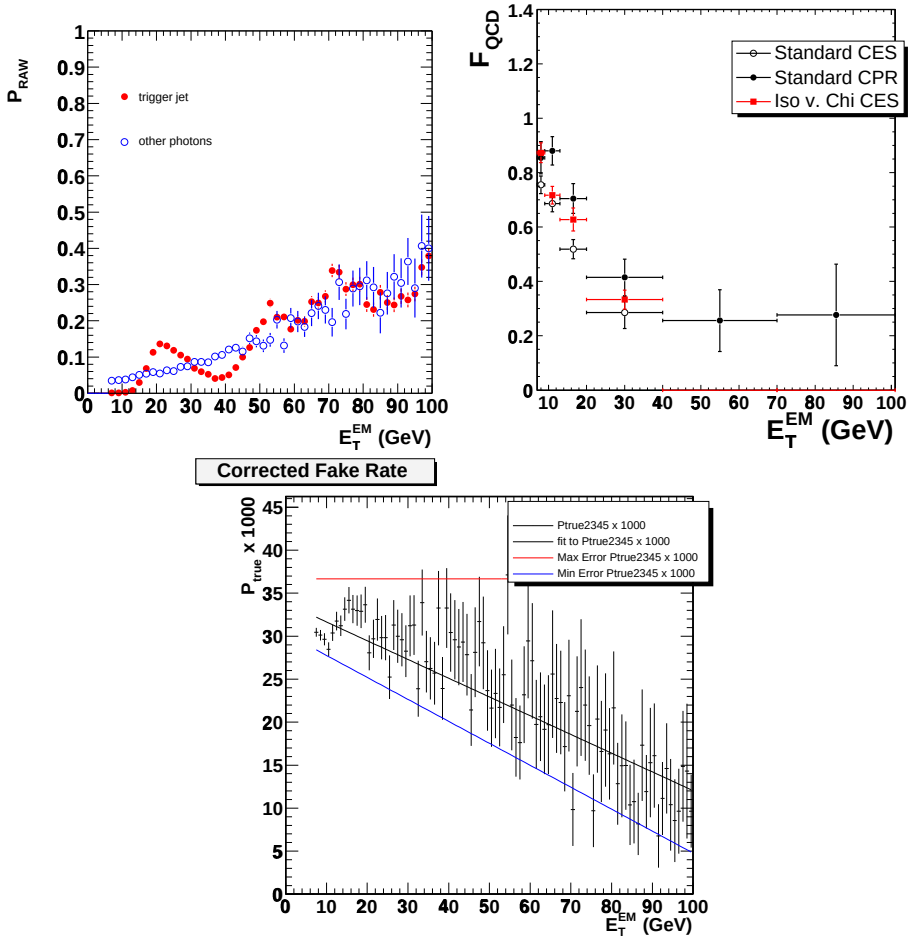

Figure 6.12: $P_{\rm raw}(E_T^{\rm EM})$ (upper left), F_{QCD} (upper right) and $P_{\rm EM\to\gamma}(E_T^{\rm EM})$ (lower) for the EM objects as a function of $E_T^{\rm EM}$.

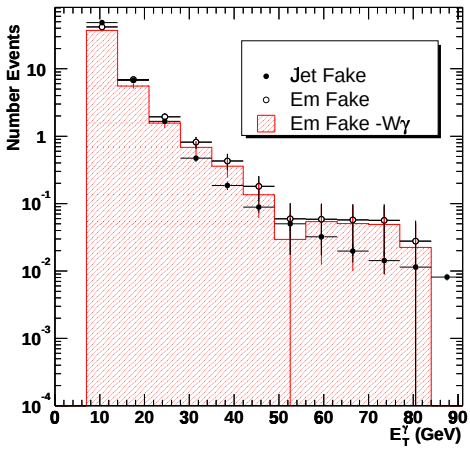

Figure 6.13: The QCD predicted background for the $W\gamma$ candidates using 345th jet method (closed points), the EM fake rate (open circle) and the EM fake rate prediction after subtracting the expected contaminations from $W\gamma$ signal (histogram).

used in WGAMMA Monte Carlo listed in Table 5.1 with initial parton level cuts listed in Table 5.2. I expect 11.74 $\pm$ 0.26 (stat.) $\pm$ 0.59 (sys.) CMUP muon one-legged $Z + \gamma$ and 5.63 $\pm$ 0.19 (stat.) $\pm$ 0.28 (sys.) CMX muon one-legged $Z + \gamma$ passing the $W\gamma$ cuts summarized in Table 8.1.

6.3 Background from $W\gamma, W \rightarrow \tau\nu, \tau \rightarrow \mu\nu\bar{\nu}$ Process

If the W of $W + \gamma$ decays to $\tau\nu$, the resulting particles are the charged lepton (electron or muon) from the τ decay and three neutrinos in leptonic decay channel of τ (two neutrinos from the τ decay and one neutrino from the W decay). The three neutrinos are observed as a single missing E_T and the signal of one charged muon along with missing E_T, which mimics the one of the W direct decay to the charged lepton.

Most of the τ background is removed when I utilize the fact that the charged muon and missing E_T coming from the τ decay are $soft$ (low energy ones). Also the W transverse mass in the τ events is significantly smaller than the one in the signal $W\gamma$ events.

To study this background I generate $W\gamma, W \rightarrow \tau\nu$ sample with Baur's WGAMMA generator following the same method as signal sample. The decay of τ lepton is performed by TAUOLA [93] which is interfaced to the PYTHIA showering.

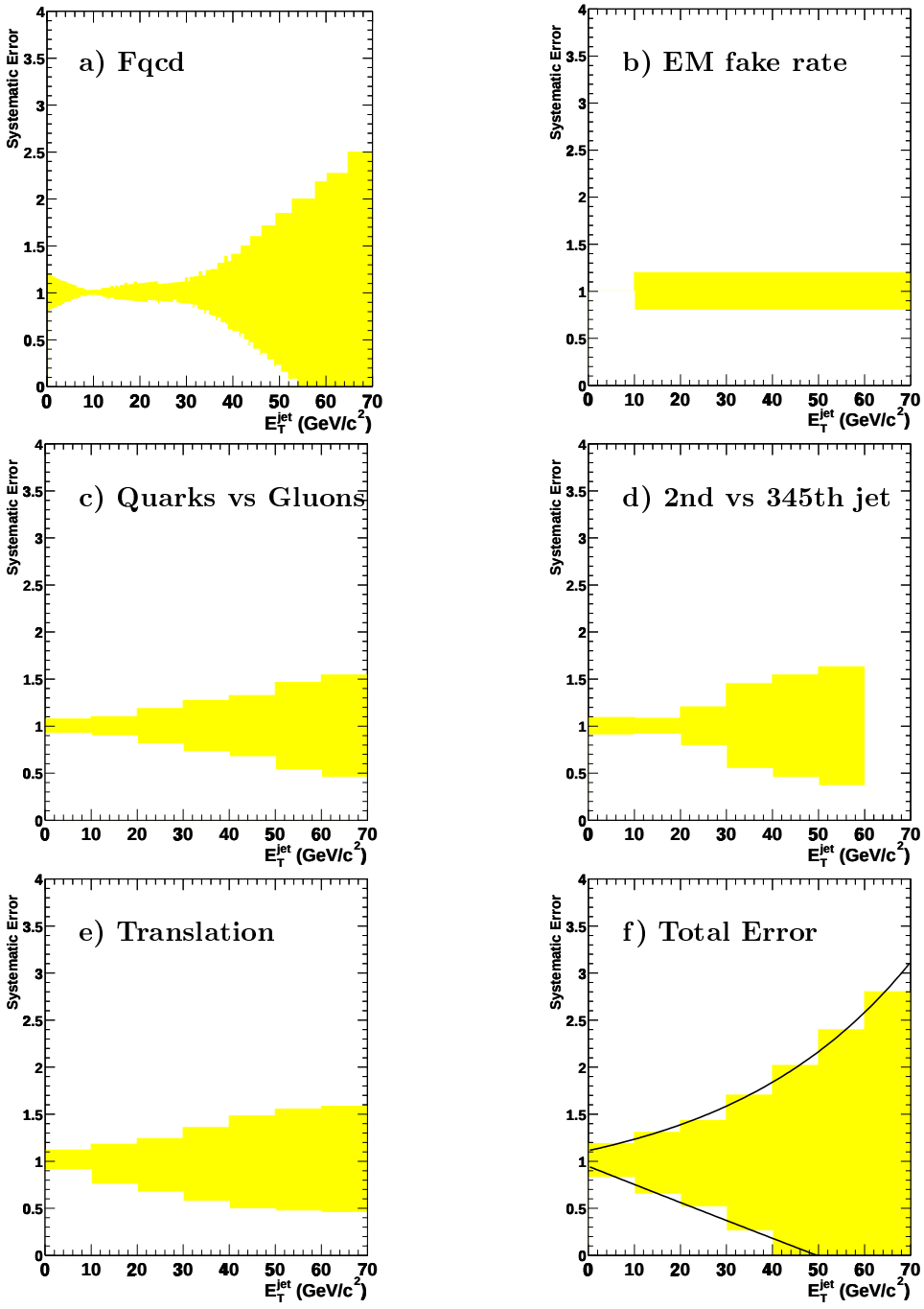

Figure 6.14: Fractional systematic error on the fake rate due to a) the method for determining F_{QCD}, b) using EM objects as denominator, c) the difference of between quark anbd gluon jets, d) the difference between the 2nd and 345th jet, e) varying the fragmentation and f) the quadratic sum of all those components as a function of $E_T^{\rm jet}$.

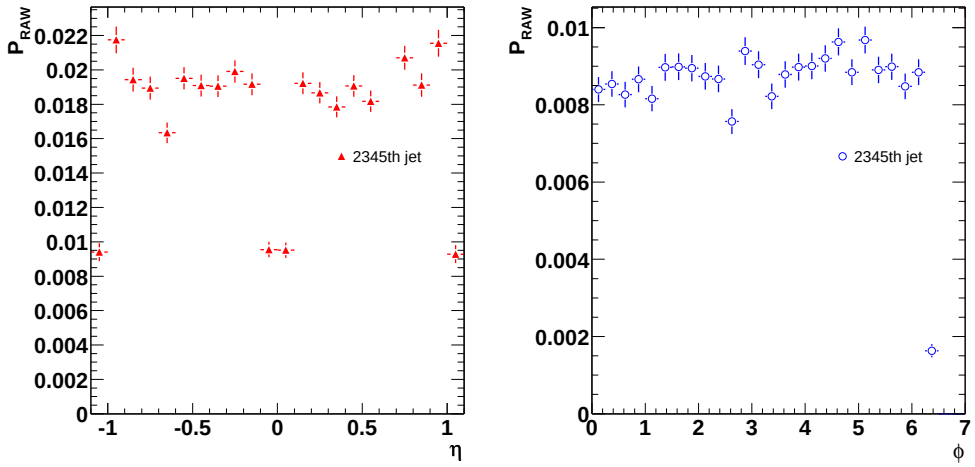

Figure 6.15: The fake rate as a function of η and ϕ of jets.

6.4 Background from Fake W

An additional background may arise from the mis-measurement of jets faking a W boson. In the inclusive W analysis, it was estimated to be $0.71 \pm 0.05(\%)$ for CMUP muon channel and $0.65 \pm 0.070(\%)$ for CMX muon channel using the $\not\!\!E_T$ versus muon isolation fraction method detailed in Section 3.4.2. In order to verify this background an new method based on the $\not\!\!E_T$ versus isolation method is used.

I can categorize $W\gamma$ events into four regions in terms of a 'fake' shown in Table 6.2. "Real W+real γ" means the "genuine $W\gamma$" candidates I seek for as a signal. "Fake W+real γ" is the amount of the background I am discussing here. "Real W+fake γ" is the background from QCD we have already discussed in Section 6.1 and "fake W+fake γ" background have already been taken into account in background from QCD.

Table 6.2: Four categories of the $W + \gamma$ candidate events in terms of a 'fake'. The sum of "real W+fake γ" and "fake W+fake γ" is estimated as $jet \rightarrow \gamma$ fake background discussed in Section 6.1.

real W + real γ	real W + fake γ
fake W + real γ	fake W + fake γ

I assume that the fake W background at low $\not\!\!E_T$, for example, $\not\!\!E_T < 10$ GeV, scales the same way for the W and $W\gamma$ analysis into the region of $\not\!\!E_T > 20$ GeV. Note that I subtracted the part of the background of $jet \rightarrow \gamma$ fake (denoted as QCD) background since that is already taken into account. Then the number

of background events due to the fake W's has a relationship of

$$\frac{\text{Number of fake '}W\text{' BG in } W\gamma}{\text{Number of fake '}W\text{' BG in inclusive } W} = \frac{\text{Number of } (W\gamma - (jet \to \gamma)) \text{ in low } \not\!\!E_T}{\text{Number of inclusive } W \text{ in low } \not\!\!E_T}. \tag{6.12}$$

The fake W background in $W\gamma$ candidates is given by

$$N_{\text{fake}W+\text{real}\gamma} = \frac{N_A - N_B}{N_C} \cdot N_D \tag{6.13}$$

where

- N_A : Events fulfilling $W\gamma$ event selection with $\not\!\!E_T < \not\!\!E_T{}^{\text{cut}}$ GeV
- N_B : Events fulfilling W+fake γ event selection with $\not\!\!E_T < \not\!\!E_T{}^{\text{cut}}$ GeV
- N_C : Events fulfilling inclusive W event selection with $\not\!\!E_T < \not\!\!E_T{}^{\text{cut}}$ GeV
- N_D : Fake "W" (QCD) Background events in inclusive W

The values of $\not\!\!E_T{}^{\text{cut}}$ is varied in 5 GeV steps between 5 - 15 GeV and the resulting number of the background events varies between -0.2 ± 2.3 and 1.5 ± 1.4 events. I have also repeated this study using muon isolation fraction instead of $\not\!\!E_T$ and got the background between -0.4 ± 0.7 and 2.2 ± 1.1 events for the variations of the isolation fraction cut value between 0.2 and 0.4.

Additionally I analyzed 220 pb^{-1} of inclusive photon Monte Carlo sample generated with E_T^γ, and found no signal event passing through the full $W\gamma$ event selection. Therefore I can place an upper limit of < 2.7 events at 95% C.L. for a luminosity of 200 pb^{-1}. All indications this background is indeed negligible, I therefore neglect it.

Chapter 7

Efficiencies and Systematic Uncertainties

In this analysis a series of event selection requirements were made in order to obtain nearly pure samples of $W+\gamma$ bosons. Making quality cuts has the effect of reducing background contributions in the event samples and therefore increases the signal to noise (S/N) ratio discussed in Chapter 6.

Now I ask the related questions of how many real events fail due to the quality requirements. Real events can fail these requirements because the energy loss mechanisms are statistical in nature. In order to calculate the cross section, it should be corrected for the efficiency of finding muon and photon, and know the real number of events that were produced. The cross section estimation has to be corrected for the efficiency of finding muon and photon. This includes the efficiency of the trigger finding a high p_T muon, the COT tracking efficiency, and the efficiencies of the criteria used to select the events as listed in Tables 3.1 and 4.1. The efficiencies for the reconstruction and identification of muons are discussed in Section 7.1 and W is detailed in Section 7.2.

The photon identification is one of the important object in the $W+\gamma$ analysis. An "excellent" photon with $E_T > 7$ GeV is identified by applying two kinds of selection: 1) the shape of energy deposit in the electromagnetic calorimeter and 2) the isolation from any other tracks or jets. The former is described in section 7.3 in which shows the results with high and low E_T datasets separately, and the latter is detailed in Section 7.4, then summarized in Section 7.5.

All the systematic uncertainties are summarized in Section 7.6.

7.1 Efficiencies for Selecting Muon

To accomplish this, I need to construct a sample of muons and then study their response to the selection requirements. This was obtained by looking at $Z \to \mu^+\mu^-$ events where both legs are linked to a CMUP or CMX muon stub with the following cuts:

- No events tagged as a cosmic.
- Both tracks have an attached stub (either CMUP or CMX).
- Z vertex of both tracks are within 60 cm, $|z_0| < 60$ cm.
- The difference of Z vertex of both tracks is within 4 cm, $|z_0(1) - z_0(2)| < 4$ cm.
- Tracks have opposite charge.
- Invariant mass of the two legs falls between $80 < \mathrm{M}(\mu^+, \mu^-) < 100$ GeV.

A triggered good quality muon (so-called biased leg) is then selection using the following cuts:

- A CMUP of CMX muons fired the muon trigger.
- Transverse momentum $p_T > 20$ GeV.
- E_{EM}, E_{HAD}, $|\Delta X_{\mathrm{CMU}}|$, $|\Delta X_{\mathrm{CMP}}|$, $|\Delta X_{\mathrm{CMX}}|$ and isolation cuts shown in Table 3.1.

These requirements actually create a fairly clean sample of Z events. Regardless of what efficiency is measured, the biased leg must always be reconstructed muon that triggered the event and passed all muon identification cuts. The unbiased leg must at least point to fiducial regions of both CMU and CMP muon chambers for CMUP muon and CMX muon chambers for CMX muon.

The muon reconstruction efficiency scale factor is the difference between the efficiency to reconstruct a muon in the data as compared to the simulation. It is used to correct an acceptance measured in the Monte Carlo, for the fact that the geometry description used in the Monte Carlo doesn't correspond exactly to the real muon geometry. To measure the reconstruction efficiency, I apply muon identification cuts to the unbiased leg for the stub matching requirements, then divide it be the number of biased legs,

$$\epsilon_{rec}^{\mathrm{CMUP}} = 0.945 \pm 0.006 \quad \text{and} \quad \epsilon_{rec}^{\mathrm{CMX}} = 0.993 \pm 0.003. \tag{7.1}$$

To measure the trigger efficiency the unbiased leg required to have stubs reconstructed and apply all muon identification cuts to the unbiased leg including the stub matching requirements. Then the efficiency is calculated by looking at the fraction of those events which also have a corresponding trigger,

$$\epsilon_{trig}^{\mathrm{CMUP}} = 0.887 \pm 0.007 \quad \text{and} \quad \epsilon_{trig}^{\mathrm{CMX}} = 0.954 \pm 0.006. \tag{7.2}$$

To measure the efficiency of muon identification cuts I require the unbiased leg to have stubs reconstructed and apply remaining muon identification cuts that are not measuring to the unbiased leg. As I require the biased leg to be

responsible for the trigger, the unbiased leg is independent of any trigger requirement. Therefore the efficiencies presented here are valid all CMUP and CMX muons independent of the trigger. The results for all data giving in Tables 7.1 and 7.2. The values using Monte Carlo samples are also given, along with the data/MC ratio ("scale factor").

Table 7.1: Results for the CMUP muon ID efficiency calculation.

	N_{events}	efficiency	N_{MC}	MC efficiency	scale factor
No cuts applied	2574	-	23121	-	-
d_0 cut	2565	0.996±0.001	23088	0.9986±0.0002	0.997±0.001
$\|\Delta X_{\text{CMU}}\|$	2455	0.954±0.004	23086	0.9985±0.0003	0.955±0.004
$\|\Delta X_{\text{CMP}}\|$	2523	0.980±0.003	22981	0.9939±0.0005	0.986±0.003
E_{EM} <2 GeV	2492	0.968±0.003	22188	0.9596±0.0013	1.009±0.003
E_{HAD} <6 GeV	2528	0.982±0.002	22573	0.9763±0.0010	1.006±0.002
COT segment	2513	0.976±0.003	23009	0.9952±0.0005	0.981±0.003
isolation < 0.1	2523	0.980±0.003	22625	0.9785±0.0010	1.002±0.003
All above	2190	0.850±0.007	20964	0.9067±0.0019	0.939±0.007

Table 7.2: Results for the CMX muon ID efficiency calculation.

	N_{events}	efficiency	N_{MC}	MC efficiency	scale factor
No cuts applied	1539	-	13797	-	-
d_0 cut	1526	0.992±0.002	13761	0.9974±0.0004	0.995±0.002
$\|\Delta X_{\text{CMX}}\|$	1531	0.995±0.002	13778	0.9986±0.0003	0.996±0.002
E_{EM} <2 GeV	1502	0.976±0.004	13278	0.9628±0.0016	1.014±0.004
E_{HAD} <6 GeV	1508	0.980±0.003	13309	0.9646±0.0016	1.016±0.003
COT segment	1494	0.971±0.004	13514	0.9795±0.0012	0.991±0.004
isolation < 0.1	1502	0.976±0.004	13481	0.9771±0.0013	0.999±0.004
All above	1386	0.901±0.008	12249	0.8878±0.0027	1.015±0.008

7.2 Efficiency for Selecting W

The efficiency scale factor of detecting the muon from W decay is defined to

$$\epsilon_W = \epsilon_{trig}\epsilon_{corr} = \epsilon_{z0}\epsilon_{trk}\epsilon_{cr}\epsilon_{zrej}\epsilon_{trig}\epsilon_{rec}\epsilon_{ID}. \tag{7.3}$$

The last three variables were described in the previous subsection.

ϵ_{z0} is the efficiency of the z_0 track cut, is the fraction of $p\bar{p}$ collisions that occur within ±60 cm of the center of CDF, $|z_0| < 60$ cm, limits the event acceptance to a portion of the full luminous region. Minimum bias data are used to measure the longitudinal profile of the $p\bar{p}$ luminous region, and the Tevatron $p\bar{p}$ longitudinal beam profile function is used to estimate the fraction of the luminous region at large z. The measured value is

$$\epsilon_{z0} = 0.950 \pm 0.004. \tag{7.4}$$

I removed all events with $|z_0| > 60$ cm before performing the acceptance calculation discussed in Section 3.6.

The tracking reconstruction efficiency is determined as the efficiency for the offline track reconstruction algorithm to reconstruct a track of a high p_T muon. To measure this quantity, decays of $W \to e\nu$ triggered and identified using only calorimeter information is used. The tracking efficiency is then the fraction of such events which have a COT track point to the "electron" cluster. This yields a tracking efficiency of $\epsilon_{trk}^{\rm data} = 0.9963^{+0.0035}_{-0.0040}$. There are two main sources of systematic uncertainties of considered: the selection of silicon stand-alone tracks which affects the silicon track fake rate, and the possibility of correlated failures of the COT and the silicon detector. Using a $W \to e\nu$ Monte Carlo sample, the MC tracking efficiency is determined as $\epsilon_{trk}^{\rm MC} = 0.9966^{+0.0015}_{-0.0024}$, consistent with the data estimate. The ratio of the COT tracking efficiencies in data and Monte Carlo is

$$\epsilon_{trk} = 1.000 \pm 0.004. \tag{7.5}$$

A small fraction of muon tracks originating from the W decay can be misidentified as a cosmic ray by the cosmic tagger discussed in Section 3.3.1. The overall efficiency of cosmic ray tagger ϵ_{cr} is measured using the electron W and Z samples. Since the electron samples are free of cosmic ray background, the fake number of tags observed in these samples is a reliable measure of the over efficiency of our algorithm for tagging real $W \to \mu\nu$ and $Z \to \mu\mu$ processes. The measured value is

$$\epsilon_{cr} = 0.9999 \pm 0.0001, \tag{7.6}$$

where the quoted error includes both statistical and systematic uncertainties.

The criteria for rejecting $Z \to \mu\mu$ events in my candidate is defined in Section 3.3. A small fraction of real $W \to \mu\nu$ signal events are also removed from $W \to \mu\nu$ via these criteria. This efficiency is measured for signal events to survive the Z rejection cuts directly from Monte Carlo. The measured value is

$$\epsilon_{zrej} = 0.9961 \pm 0.0017. \tag{7.7}$$

I used the efficiency scale factors from Table 7.1 - 7.2 and Equations 7.1-7.7 to calculate the efficiency scale factor for $W \to \mu\nu$ process:

$$\epsilon_{corr}^{\rm CMUP} = 0.841 \pm 0.012 \quad \text{and} \quad \epsilon_{corr}^{\rm CMX} = 0.955 \pm 0.012. \tag{7.8}$$

7.3 Photon ID Efficiencies : Shape of Energy Deposit in Calorimeter

In this section the photon identification in terms of the shape of the energy deposit is described. Since the photons and electrons behave similar in the electromagnetic calorimeter, I regarded electron candidates from the $Z \to ee$ decay or conversions as photon candidates. These different samples cover large E_T

region: Electron candidates from the $Z \to ee$ decay cover high E_T, and electrons from conversions cover low E_T regions. The series of the photon selection criteria used in $W\gamma$ production analysis shown in Table 4.1 are applied to above electrons, then photon ID efficiencies are determined.

7.3.1 Dataset and Definition of the Efficiency

In this study following data and MC samples were used:

- Photons from $W\gamma$ Monte Carlo.
- Electrons from $Z \to e^+e^-$ Data/Monte Carlo.
- Electrons from Conversion Data/Monte Carlo.

Additional requirements for each sample are described the following paragraph.

Photons from $W\gamma$ Monte Carlo

Events were generated by the `WGAMMA` generator described in Section 5.1. The photon selection was based upon Table 4.1. Following selections were required to extract pure photon from $W + \gamma$ Monte Carlo samples.

- Select central γ ($|\eta(\gamma)| < 1.1$) with $E_T(\gamma) > 7$ GeV at the generator level.
- Reconstruct a W requiring all inclusive W selection cuts, high p_T muon ($p_T > 20$ GeV), large missing E_T ($\not\!\!E_T > 20$ GeV) and transverse mass cuts ($30 < M_T < 120$ GeV). See detail about W selection in Section 3.
- Photons which convert in the material during the detector simulation is rejected.[1]
- If photon passes E_T^γ >7 GeV, $|X_{\rm CES}|$, $|Z_{\rm CES}|$ and Had/Em calorimeter cuts, it becomes part of base samples, N^{i-1}.
- Apply Isolation, $\langle\chi^2_{\rm CES}\rangle$, N3D, Track Isolation and 2nd CES strip/wire e-nergy cuts in this order. If it passes, it becomes part of N^i.
- The definition of the relative photon ID efficiency is,

$$\epsilon^i = \frac{N^i}{N^{i-1}}. \tag{7.9}$$

[1] If there is a photon whose related vertex with radius of < 42 cm (inside COT wall), the event is regarded as the conversion in the material.

Electrons from the $Z \to e^+e^-$ decays

Data samples are triggered by high E_T electron trigger `ELECTRON_CENTRAL_18`[2] and Drell-Yan process generated by `Pythia` [82] are used as the Monte Carlo sample. I selecte di-electron events and require the following selections to obtain the efficiencies.

- The invariant mass of di-electron pair is required to be within $85 < \mathrm{M}(e^+, e^-) < 95$ GeV, to extract pure $Z \to ee$ candidates.
- To avoid jet faking leptons, an event having more than 2 loose electron, is removed. "Loose electron" selection criteria is listed in Table 7.3.

Table 7.3: Loose electron selection criteria.

Loose electron criteria
Central region $\|\eta\| < 1.1$
$E_T > 25$ GeV
$p_T > 10$ GeV
$\|z_0\| < 60.0$ cm
Opposite charge
Fiduciality in the CEM detector
$85 < \mathrm{M}(e^+, e^-) < 95$ GeV

- Randomly an electron is selected and check if it passes the tight electron requirements as defined in Table 7.4. If it passes, the other electron from the Z decay is regarded as unbiased electron and uses for photon ID efficiency study.
- Unbiased electron should pass $0.9 < E/P < 1.1$ cut to suppress the radiative electron. If it passes, photon baseline cuts listed in Table 4.1 are applied.
- Since requirements shown in Table 4.1 is for electron not photon, some requirements need to be changed: $E_T > 25$ GeV, since it is required to be a good quality electron. N3D should be ≤ 2 instead of ≤ 1, because electron track has already counted as 1. Electron track (highest p_T track) has been subtracted from the track isolation requirement.
- QCD background and trident events subtraction are taken into account. Process which contain a real electron or which can fake one are included in the QCD background in $Z \to ee$ process. They are expected to be

[2]Central EM cluster with $E_T > 18$ GeV and COT track with $p_T > 9$ GeV pointing at the cluster is required.

Table 7.4: Tight electron selection criteria. Δx is the distance in the $r-\phi$ plane between the extrapolated track and the best matching CES cluster. Δz is the distance in the $r-z$ plane between the extrapolated track and the best matching CES cluster. COT track quality is requiring the track has been reconstructed in the COT in 3-axial and 3-stereo super layers with at least 7 hits in each.

Tight electron criteria
$\|\eta\| < 1.1$
$E_T > 25$ GeV
$p_T > 10$ GeV
Had/Em $< 0.055 + 0.00045*$ E
Lshr < 0.2
$E/P < 2.0$ (for $E_T < 100$ GeV only)
$\|z_0\| < 60.0$ cm
$\chi^2_{\rm strip} < 10$
-3.0 $<$ Charge $*\Delta x < 1.5$ cm
$\|\Delta z\| < 3.0$ cm
COT track quality
Isolation/$E_T < 0.2$
Fiduciality in CEM detector

charge symmetric, i.e. the number of opposite sign and same sign QCD background events should be the same. Thus, it is possible to use the number of same sign events to estimate the number of QCD background events in the opposite sign sample. The efficiency is defined by

$$\epsilon^i = \frac{N^i(\text{opp}) - N^i(\text{same})}{N^{i-1}(\text{opp}) - N^{i-1}(\text{same})}, \tag{7.10}$$

where, 'opp' means a pair of opposite sign charged electrons and 'same' means that of same sign charged electrons.

Electrons from conversion sample

The 4 GeV single electron triggered sample (`ELECTRON_CENTRAL_4` trigger path) are used as the conversion data sample. Single photon MC generated with $E_T^\gamma > 20$ GeV and $|\eta(\gamma)| < 1.1$ and diphoton MC with $E_T^\gamma > 10$ GeV are used as the conversion MC samples. Note that above photon MCs are used as the conversion MC dataset not photon MC samples.

I selected conversion events as follows:

- There are more than two electromagnetic objects in event.
- Having Oppositely charged tracks.

- The small separation in cotangent of their polar angles, $\Delta \cot\theta < 0.03$.
- The radial separation between the two tracks in the x-y plane at the point where they are parallel (ΔXY) is smaller 0.1cm.
- Conversion radius is required to be within $5 < r < 42$ cm, which is corresponding to be inside COT inner wall.

Following figures shows $\Delta \cot\theta$, separation in ΔXY, invariant mass of two tracks and conversion radius using data(Figure 7.1). $\Delta \cot\theta$ plot is fitted with double Gaussians and a second degree polynomial. As the background contamination in $\Delta \cot\theta$ distribution is quite small, it is not subtracted. The event if three tracks passes above cuts is rejected, because it is "trident" event.

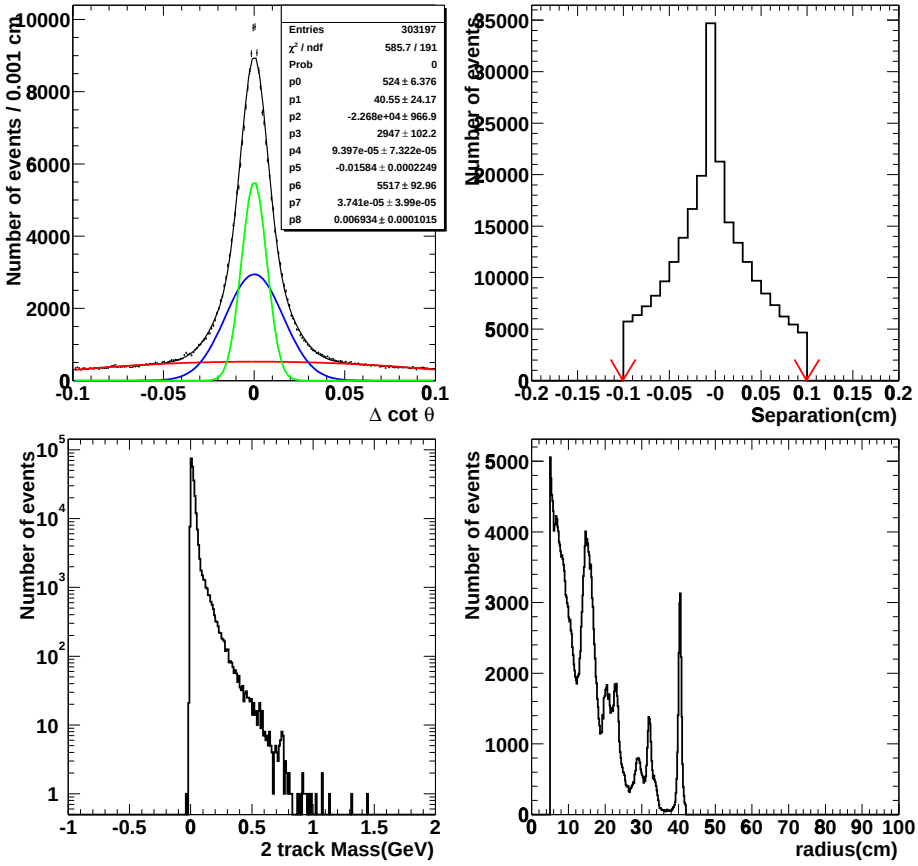

Figure 7.1: $\Delta \cot\theta$ (without $\Delta \cot\theta$ cut), ΔXY, invariant mass of two tracks, and conversion radius distributions for the pair of conversion tracks using 4 GeV triggered electron data.

- Two conversion legs are required to be extrapolated to the different CES wedges.

Table 7.5: Level 3 trigger requirements for ELECTRON_CENTRAL_4 dataset. L_{shr} (Lateral Shower Sharing variable) is the quantity to discriminate electrons and photons from hadronic showers faking these particles in the central electromagnetic calorimeter. This is done by comparing the observed sharing of energy deposition between towers in the CEM to that expected for a true electromagnetic shower, taken with test-beam data and recorded in the database. Δx is the distance in the $r-\phi$ plane between the extrapolated track and the best matching CES cluster. Δz is the distance in the $r-z$ plane between the extrapolated track and the best matching CES cluster.

ELECTRON_CENTRAL_4 trigger requirements
Track $p_T \geq 4$ GeV
Had/Em ≤ 0.08
$L_{shr} \leq 0.2$
$\chi^2_{\rm strip} \leq 10$
$\chi^2_{\rm wire} \leq 15$
$\Delta x \leq 2$
$\Delta z \leq 3$

- Look for a pair of EM Objects pointed by the two tracks.
- Randomly an EM Object is selected and check if it passes the Level 3 trigger cuts (Table 7.5). If it passes, the other leg from conversion i regarded as an unbiased electron and used for photon ID study.
- Unbiased electron should pass $0.9 < E/p < 1.1$ and criteria listed in Table 4.1. However, isolation, N3D and track isolation cuts aren't applied for conversions, because most of two conversion legs falls into the neighbor CES wedges, it becomes difficult to apply these cuts. Instead of the isolation cuts, the number of tracks in cone $\Delta R(=0.4) \leq 2$ cut is required in addition.
- The definition of the efficiency is,

$$\epsilon^i = \frac{N^i}{N^{i-1}}. \tag{7.11}$$

Summary of the event selection

I summarize the series of cuts and dataset in Table 7.6. I separate the set of cuts into two categories, applying the full set of photon ID cuts (Method(1)) and the reduced cuts for the conversion samples(Method(2)). Figure 7.2 shows the E_T distributions of each sample.

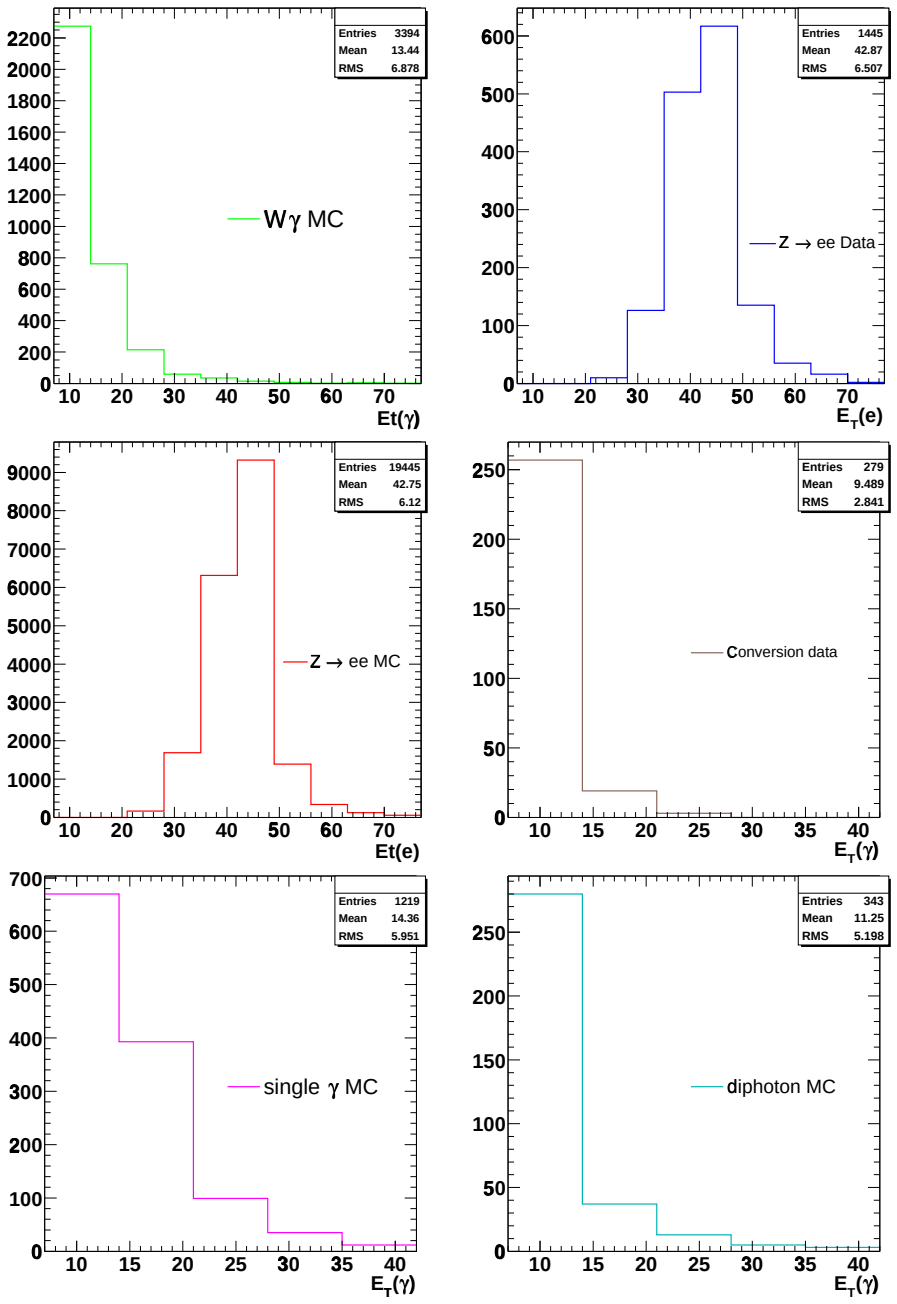

Figure 7.2: E_T^γ or E_T^e distributions in the $W\gamma$ MC, $Z \to ee$ data, $Z \to ee$ MC, conversion data, single photon MC and diphoton MC samples.

Table 7.6: The series of cuts and datasets to measure the photon ID efficiency. Method(1) covers high E_T photon ID efficiencies and Method(2) covers low E_T photon ID efficiencies, respectively.

Method	(1)	(2)
Dataset	$W\gamma$ MC $Z \rightarrow$ ee Data, MC	$W\gamma$ MC Conversion Data, MC $Z \rightarrow$ ee Data, MC
Had/Em, $\lvert X_{\rm CES}\rvert$, $\lvert Z_{\rm CES}\rvert$	$\surd$	$\surd$
E/p for electron	$\surd$	$\surd$
E_T	> 25 GeV	> 7 GeV
Number of tracks in $\Delta R(=0.4) \leq 2$		$\surd$
Isolation	$\surd$	
N3D	$\surd$	
Track Isolation	$\surd$	
$\langle\chi^2_{\rm CES}\rangle$	$\surd$	$\surd$
2nd strip E	$\surd$	$\surd$
2nd wire E	$\surd$	$\surd$

7.3.2 Results with High E_T Datasets

The efficiency and the their correction factor with high E_T datasets are shown. The number of events left after each cut using photons and electrion from $W\gamma$ and $Z \rightarrow ee$ samples (Method (1)) listed in Table 7.7. The relative photon ID efficiencies and the correction factor, the ratio of the efficiency using $Z \rightarrow ee$ Data to MC, are shown in Table 7.8.

Table 7.7: The number of events left after each photon ID cuts using $W\gamma$ and $Z \rightarrow ee$ samples (Method (1)).

	$W\gamma$ MC	$Z \rightarrow ee$ Data (same, opp)	$Z \rightarrow ee$ MC (same, opp)
Base	3394	1445, 6	19445, 66
Isolation	3133	1395, 4	18607, 62
N3D	3078	1330, 1	18186, 54
Track Isolation	3032	1287, 1	17811, 52
$\langle\chi^2_{\rm CES}\rangle$	3019	1258, 1	17768, 52
2nd Strip E	2965	1247, 1	17547, 52
2nd Wire E	2947	1223, 1	17382, 52

Figure 7.3 show the time dependency of overall photon ID efficiency using $Z \rightarrow ee$ data. It shows the efficiency as a function of run number splitted data into 7 run ranges which has approximately 30 pb^{-1} in each. It is clear there

Table 7.8: Photon ID efficiencies using $W\gamma$ and $Z \to ee$ samples. The correction factor is the ratio of the efficiency using $Z \to ee$ data to $Z \to ee$ MC. The statistical errors only are taken into account.

	$W\gamma$ MC	$Z \to ee$ Data	$Z \to ee$ MC	Corr. factor
Isolation	0.9231 $\pm$0.0046	0.9666 $\pm$0.0049	0.9570 $\pm$0.0015	1.01 $\pm$0.005
N3D	0.9824 $\pm$0.0023	0.9554 $\pm$0.0058	0.9777 $\pm$0.0011	0.977 $\pm$0.006
Track Iso	0.9851 $\pm$0.0022	0.9676 $\pm$0.0049	0.9794 $\pm$0.0011	0.988 $\pm$0.005
$\langle\chi^2_{\rm CES}\rangle$	0.9957 $\pm$0.0011	0.9774 $\pm$0.0041	0.9976 $\pm$0.0004	0.980 $\pm$0.004
2nd Strip E	0.9821 $\pm$0.0024	0.9912 $\pm$0.0026	0.9875 $\pm$0.0008	1.00 $\pm$0.003
2nd Wire E	0.9939 $\pm$0.0014	0.9807 $\pm$0.0039	0.9906 $\pm$0.0007	0.990 $\pm$0.004

is no time dependent effect. Figure 7.4 shows overall photon ID efficiency with electrons in $Z \to ee$ data and MC and photons in `WGAMMA` MC as a function of E_T, η and ϕ. The efficiency using $Z \to ee$ and $W\gamma$ MC doesn't match the low E_T region. So I checked the relative photon ID efficiencies as a function of E_T^γ

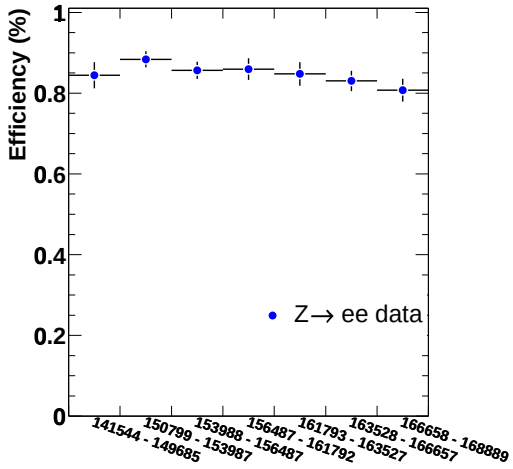

Figure 7.3: Time dependency of overall photon ID efficiency using $Z \to ee$ data. The histogram shows the efficiency splitted data into 7 run ranges which has approximately 30 pb^{-1} in each.

shown in Figure 7.5. It is obvious that this discrepancy is due to the difference of the efficiency of isolation.

Figure 7.6 shows the ratio of the efficiency between $Z \to ee$ MC and $W\gamma$ MC as a function of E_T^γ. This is for the cross-check whether electrons from $Z \to ee$ MC really represents the behavior of photons in the $W\gamma$ MC. They have some fluctuation due to the statistics, but are flat as a function of E_T. Figure 7.7 shows the correction factor, the ratio of the efficiency with $Z \to ee$

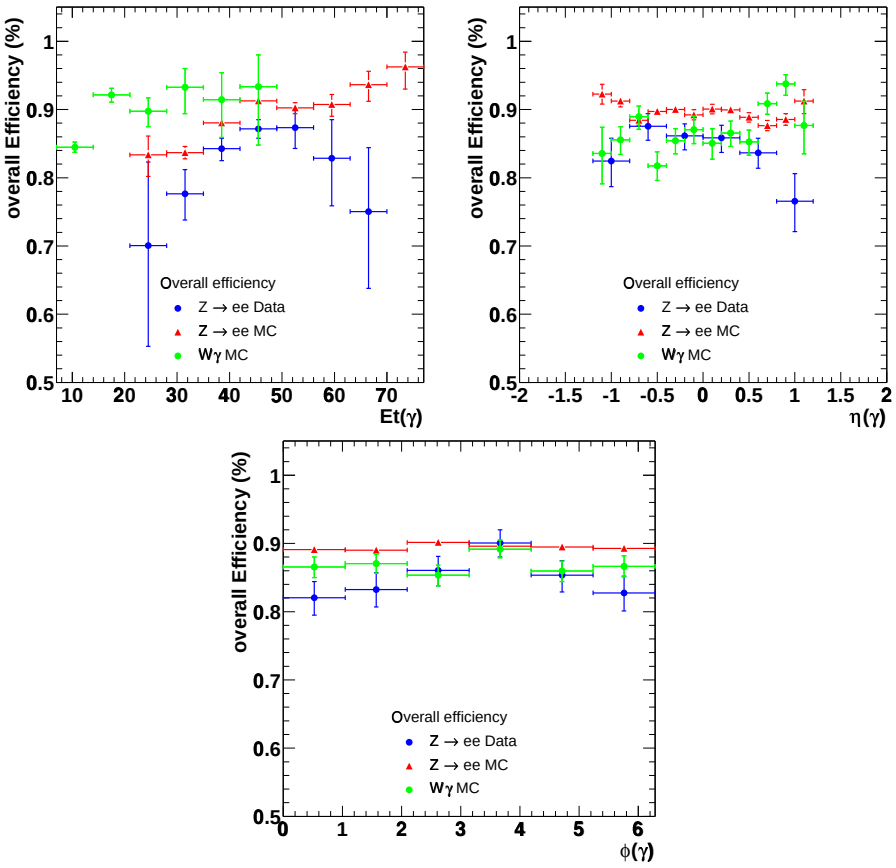

Figure 7.4: Overall photon ID efficiency using electrons in $Z \rightarrow ee$ data and MC and photons in `WGAMMA` MC as a function of E_T, η and ϕ.

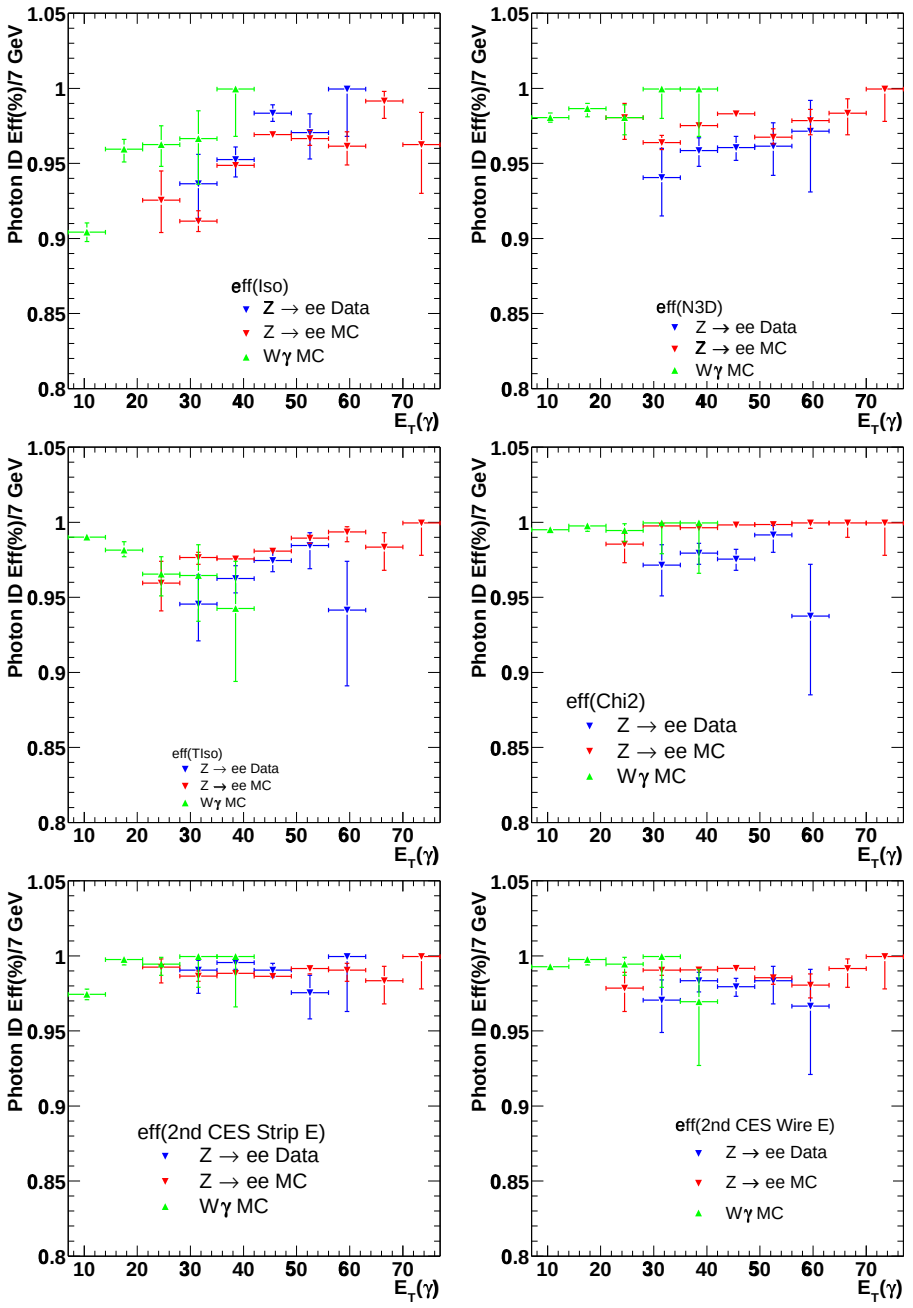

Figure 7.5: Photon ID efficiencies using photons and electrons in $W\gamma$ MC, $Z \rightarrow ee$ data and MC, for the isolation, N3D, track isolation, $\langle\chi^2_{\rm CES}\rangle$, 2nd CES strip and wire energy cuts as a function of E_T.

data to $Z \rightarrow ee$ MC. The distributions for the $\langle\chi^2_{\rm CES}\rangle$, strip and wire energy cuts are flat approximately 1.0, but the distribution for the isolation depends on E_T^γ. I will adopt the correction factor for the photon isolation as a function of E_T discussed later in Section 7.4.

7.3.3 Results with Low E_T Datasets

Table 7.9 shows the number of events left after the cuts using all samples(Method (2)). Table 7.10 and 7.11 shows the relative photon ID efficiencies and their correction factors. The correction factor defined as the ratio of the efficiency using conversion data to conversion MC. The statistical error only are taken into account. Figure 7.8 shows the overall photon ID efficiency using $W\gamma$

Table 7.9: The number of events left after each photon ID cut (Method (2)).

	$W\gamma$ MC	Z Data (same, opp)	Z MC (same, opp)	Conv Data	Conv(1) single-γMC	Conv(2) di-γMC
Base	3394	1445, 6	19445, 66	279	1219	343
$\langle\chi^2_{\rm CES}\rangle$	3374	1410, 5	19396, 65	275	1214	343
2nd St E	3311	1399, 5	19155, 65	273	1183	330
2nd Wi E	3280	1364, 5	18912, 62	265	1173	327

Table 7.10: The photon ID efficiencies using photons and electrons in $W\gamma$ MC, $Z \rightarrow ee$ data and MC, conversion data and MCs with the Method(2).

	$W\gamma$ MC	$Z \rightarrow ee$ Data	$Z \rightarrow ee$ MC
$\langle\chi^2_{\rm CES}\rangle$	0.9941 $\pm$0.0013	0.9764 $\pm$0.0041	0.9975 $\pm$0.0004
2nd Strip E	0.9813 $\pm$0.0023	0.9922 $\pm$0.0024	0.9875 $\pm$0.0008
2nd Wire E	0.9906 $\pm$0.0017	0.9749 $\pm$0.0042	0.9874 $\pm$0.0008

	Conv data	Conv MC(1)	Conv MC(2)
$\langle\chi^2_{\rm CES}\rangle$	0.986$\pm$0.007	0.996 $\pm$0.002	1.0$\pm$0.0
2nd Strip E	0.993$\pm$0.005	0.974 $\pm$0.005	0.962$\pm$0.010
2nd Wire E	0.971$\pm$0.010	0.992 $\pm$0.003	0.991$\pm$0.005

Table 7.11: The correction factors using $Z \rightarrow ee$ and conversion samples.

Corr. factor	$Z \rightarrow ee$	Conv(single-γ)MC	Conv(di-γ)MC
$\langle\chi^2_{\rm CES}\rangle$	0.979 $\pm$0.004	0.990$\pm$0.007	0.986 $\pm$0.007
2nd Strip E	1.00 $\pm$0.002	1.02 $\pm$0.007	1.03 $\pm$0.011
2nd Wire E	0.987 $\pm$0.004	0.979$\pm$0.010	0.980 $\pm$0.011

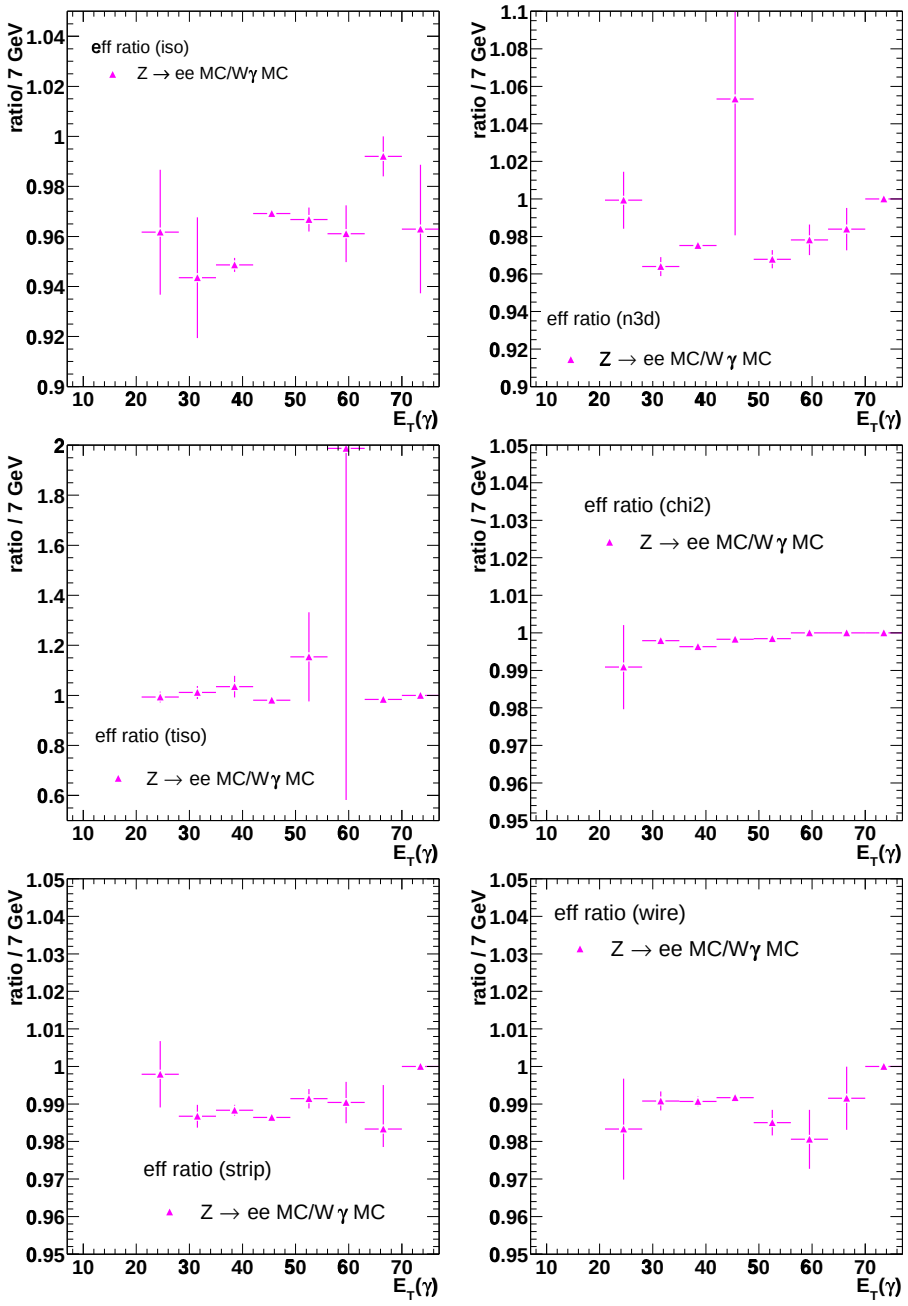

Figure 7.6: The ratio of the efficiency distributions between $Z \rightarrow ee$ MC and $W\gamma$ MC as a function of E_T^{γ} for isolation, N3D, track isolation, $\langle \chi^2_{\rm CES} \rangle$, 2nd CES strip and wire energy.

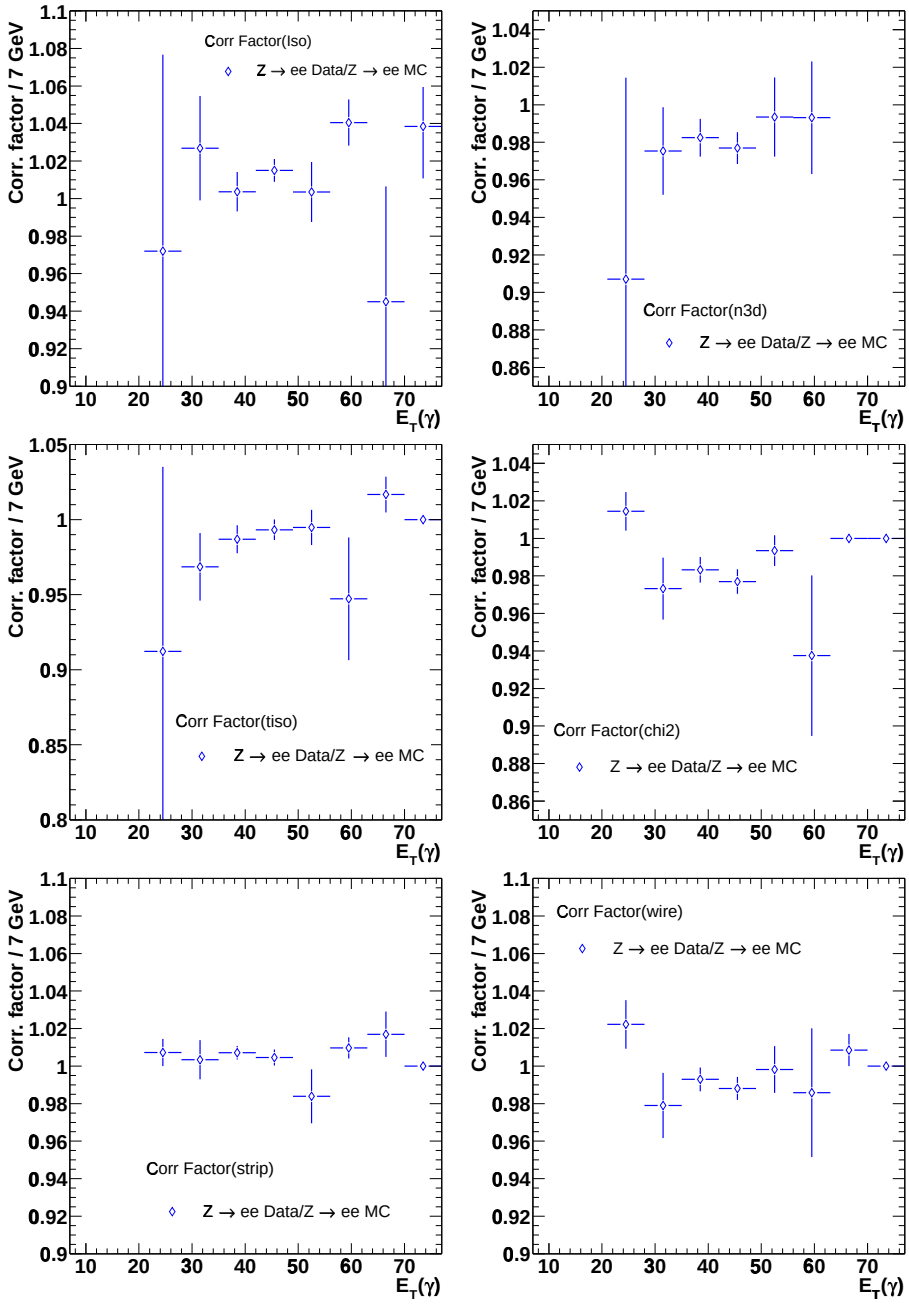

Figure 7.7: Correction factor as a function of E_T^γ, for isolation, N3D, track isolation, $\langle\chi^2_{\rm CES}\rangle$, 2nd CES strip and wire energy.

MC, $Z \rightarrow ee$ data and MC, conversion data and MCs as a function of E_T, η and ϕ. Figure 7.9 shows the photon ID efficiencies for each cut as a function of $E_T(\gamma)$. Figure 7.10 shows the ratio of the efficiencies with conversion and $Z \rightarrow ee$ MC to $W\gamma$ MC. These MCs well represent the behavior of the $W\gamma$ Monte Carlo. Figure 7.11 shows the correction factor, which is defined the ratio of the efficiency between conversion data and conversion MC.

Summary of the correction factors is discussed in Section 7.5.

7.4 Photon ID Efficiencies : Isolation

In this section photon identification efficiencies in terms of the isolation from any other tracks or jets are discussed. A clean photon itself is well-isolated but may be smeared by jets and underlying energy activities. In order to measure the efficiency, a random cone technique were applied: A virtual cone of radius ΔR =0.4 is randomly thrown in the spherical of detector, cluster(s) of the energies are constructed inside the cone, then the isolation cuts is applied to the cluster. The necessity for this technique arises since there is no way to gather a pure photon sample without first applying isolation cuts.

The high E_T electron data, jet and minimum bias sample [3] are used for this study. After making the W selection cuts which requires a high E_T electron and a large missing E_T in the electron sample, a virtual cone is thrown in the detector. To avoid to overlap the electron cluster and a virtual cone, the ϕ of the cone is set to $\phi_e + 90^\circ$ and the η set to a random value in the fiducial region (-1.1 $< \eta <$ 1.1). Figure 7.12 shows the schematic view of the random cone method using $W \rightarrow e\nu$ sample. The same technique is applied in the jet sample. Since there is no trigger object in the minimum bias sample, both a random η and ϕ are chosen. The cone itself has no E_T, an arbitrary E_T are chosen for the cone in order to apply the cuts that are ratios or sliding between 7 to 50 GeV. The cuts are then applied in the order listed in Table 4.1 and the efficiency defined as the simple ratio in Equation 7.12,

$$\epsilon = \frac{\text{Number of cones passed}}{\text{Number of total cones thrown}}. \tag{7.12}$$

As the fiducial cuts are solely geometric, they have an efficiency of 100%. There is no requirement that the cone chosen not point at an object. Thus the effect of a jet "clobbering" a photon is measured along with the effect of underlying event.

[3] In hadron collision there is an underlying event resulting from spectator parton interactions in addition to the hard scatter. Minimum bias events are the samples collected in order to measure such an additional underlying energy activity in event. The underlying energy is usually very soft.

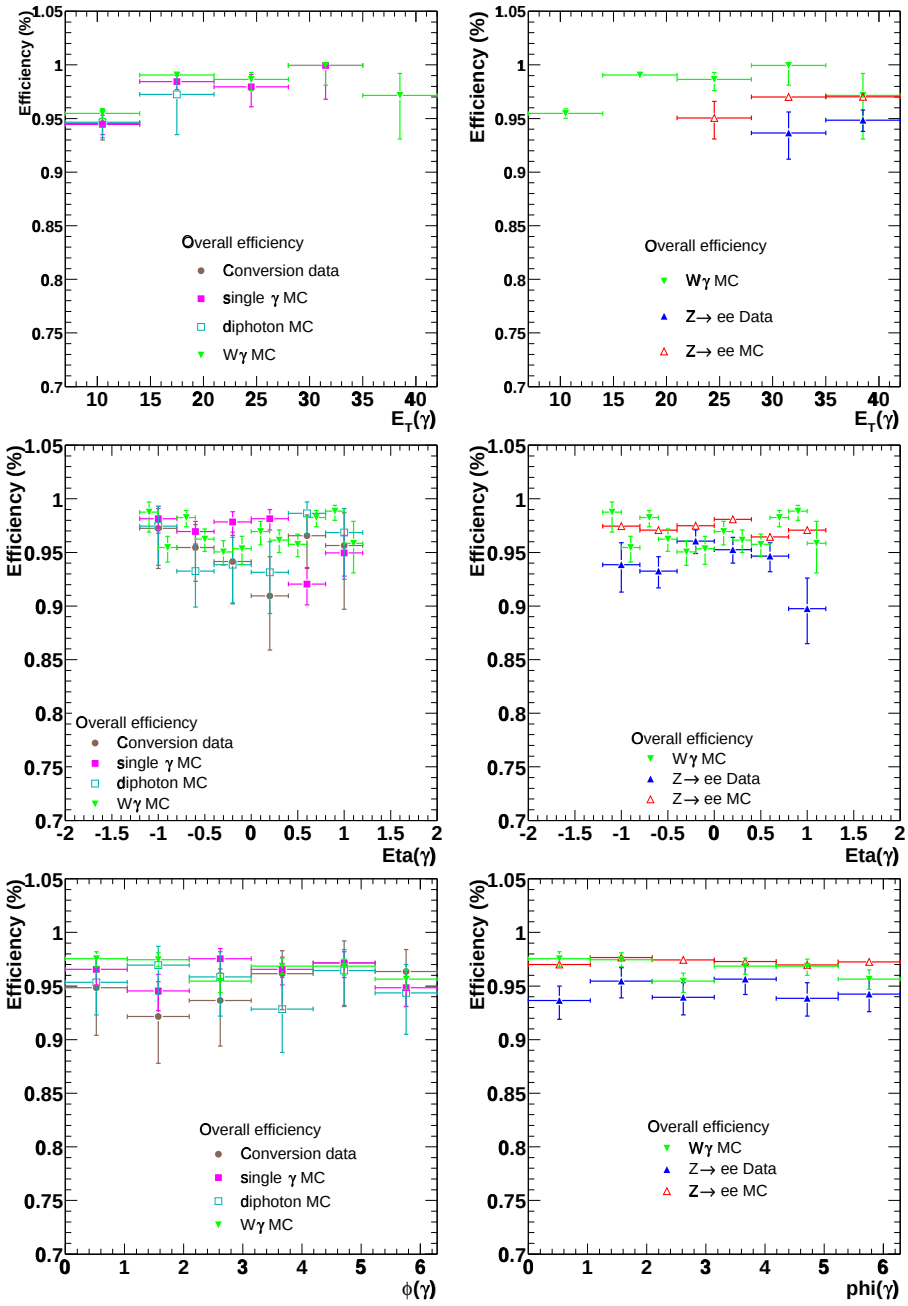

Figure 7.8: The overall photon ID efficiency using photons and electrons in the $W\gamma$ MC, $Z \rightarrow ee$ data and MC, conversion data and MCs as a function of E_T, η and ϕ.

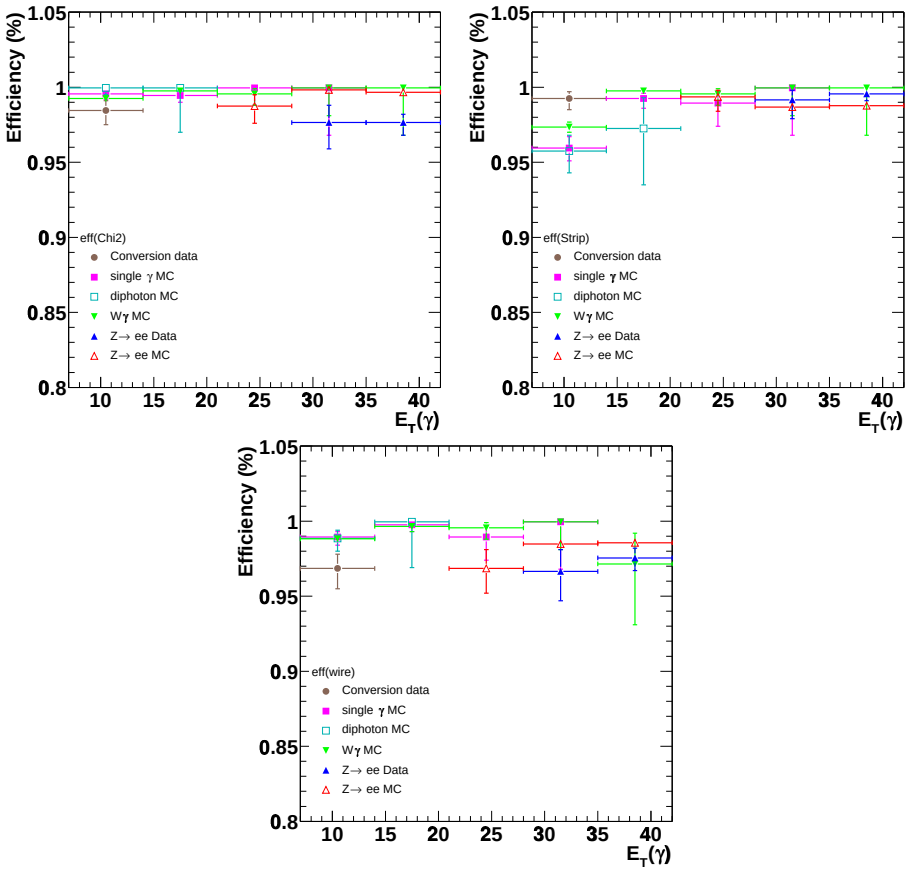

Figure 7.9: The photon ID efficiency using photons in the $W\gamma$ MC, electrons in $Z \rightarrow ee$ data and MC, conversion data and MCs as a function of E_T.

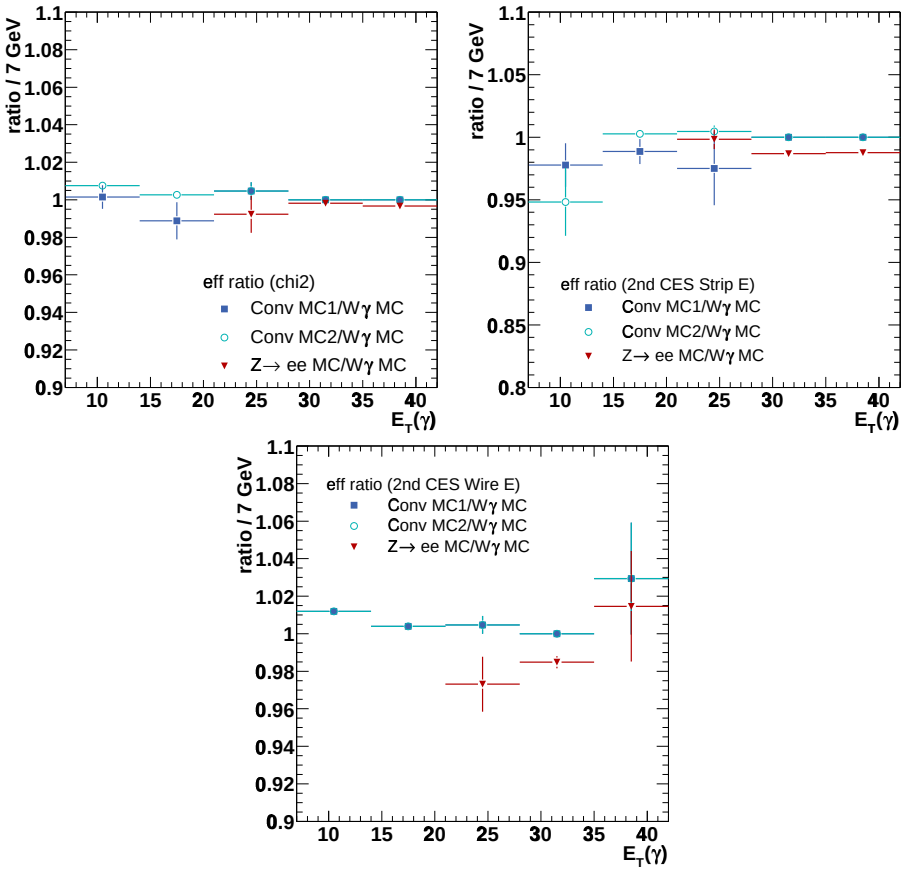

Figure 7.10: The ratio of the efficiencies between conversion and $Z \rightarrow ee$ MC samples to $W\gamma$ MC.

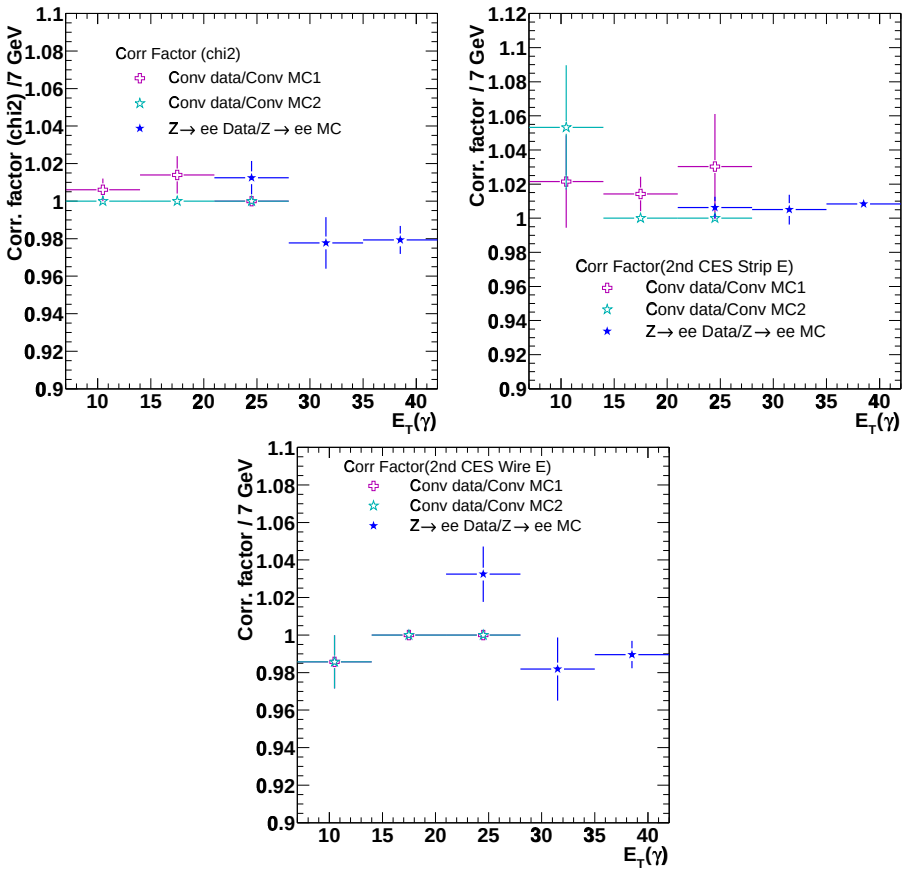

Figure 7.11: Correction factor as a function of E_T^{γ}.

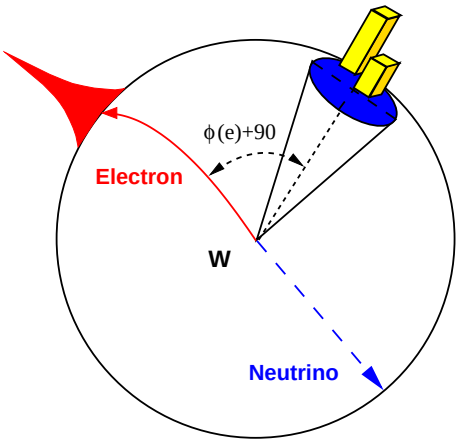

Figure 7.12: Schematic draw of the random cone method. After making W selection, the ϕ of the cone is chosen to $\phi(e) + 90°$ and the η of the cone is set a random value in the fiducial region. Then isolation cuts are applied the cluster of energy in a cone of radius ΔR =0.4.

7.4.1 Event Vertex and Underlying Energy Correction

The isolation cuts have several corrections that are applied to the cone based upon the topology of the event. The largest and most important correction is additional underlying event energy from multiple interactions. The correction depends on the number of reconstructed vertices in the event, because the multiple interaction event have additional vertices.

The event vertex in W events was selected as the z_0 of the track, while in the other samples as the highest sum of the p_T of the tracks which construct the vertex with a good quality. For a small fraction of the W events, no 'good quality' vertex is reconstructed containing the high p_T track of the electron. This is due to a cut in the vertexing algorithm on the minimal number of tracks. Looking at the distribution of ΔZ_0 between the z vertex of the electron associated track and events with only one good quality vertex shown in Figure 7.13. The reconstruction resolution appears to be less than 3.0 cm. So for counting vertices, the z_0 of the electron is one vertex, and every additional good quality vertex more than 3.0 cm away from this z_0 is an additional vertex. Using this counting convention, the total energy in the cone as a function of the number of vertices was fitted to a linear function using $W \to e\nu$ data shown in Figure 7.14. The fitted function in W events is,

$$E_{\text{Corr}} = 0.28 \cdot (N_{\text{vertices}} - 1)\,. \tag{7.13}$$

This E_{Corr} is additionally subtracted from the energy found in the cone of 0.4 surrounding the photon.

To check the consistency the same technique was applied to jet sample and minimum bias events shown in Figure 7.14. Jet sample gave an equivalent fit and the resulting slope is within errors by ± 0.01. While the fit in the minimum bias data was lower by 0.03. This is expected due to the fact that the minimum bias data is not luminosity weighted, while the W data is biased towards higher luminosity. All of the energies measured in the calorimeter were calculated adjusting for the event vertex. The correction shown above was then used in all of the studies that follow.

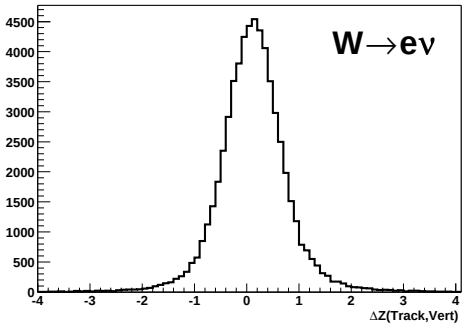

Figure 7.13: ΔZ_0 distribution between the z vertex of the electron associated track and the closest good quality vertex in $W \rightarrow e\nu$ event.

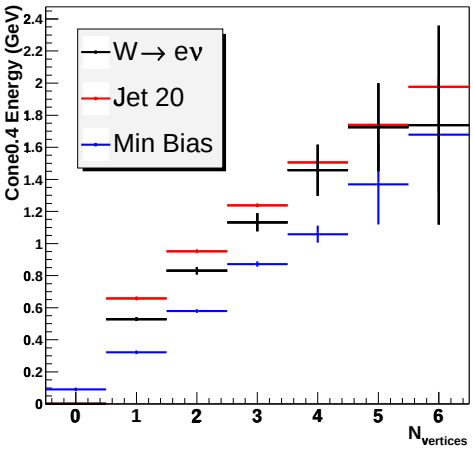

Figure 7.14: Isolation Energy in a cone of 0.4 as a function of the number of vertices in event for $W \rightarrow e\nu$, jet, and minimum bias data samples.

7.4.2 Efficiencies with Random Cone Method

The efficiency of **the calorimeter isolation** in data and Monte Carlo are shown in Figure 7.15. If the events are separated by the number of vertices in the event, a strong dependence on the number of vertices is apparent. This is shown in Figure 7.16. While the correction for underlying event from multiple interactions corrects some of this difference, it is not expected to completely correct it. This effect is due to the fact that with more than one interaction in an event, there will be more final state objects crossing the detector. A photon will then have less vacant space in the detector to deposit its energy, and thus the photon will be smeared more often. Since there were no additional interactions in the generation or simulation, no such effect occurs in Monte Carlo.

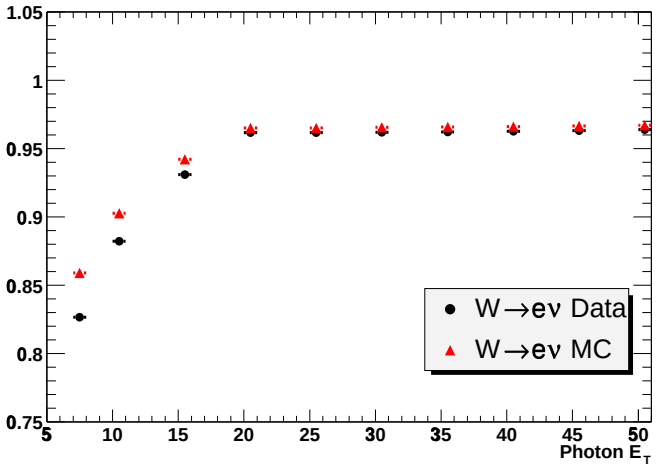

Figure 7.15: The isolation efficiency is shown with the assumed photon energy in $W \rightarrow e\nu$ data and Monte Carlo events. The data is for any number of vertices, while the Monte Carlo has only one vertex.

Depending on the instantaneous luminosity during a run period, there will be a different rate of multiple interactions. Such changes will affect the efficiency of the calorimeter isolation, and the profile of instantaneous luminosity must be accounted for by weighting the different distributions in Figure 7.16. Since the efficiency is measured in the data sample itself, it is done by taking the single data curve shown in Figure 7.15. This curve has the appropriate luminosity profile, and therefore the correct weighting of events with multiple interactions. The ratio of the two efficiency curves in Figure 7.15 was fitted with a third order polynomial to give the correction to the MC efficiency as a function of photon E_T. The ratio and fit are shown in Figure 7.17 with the fitted function up to 20

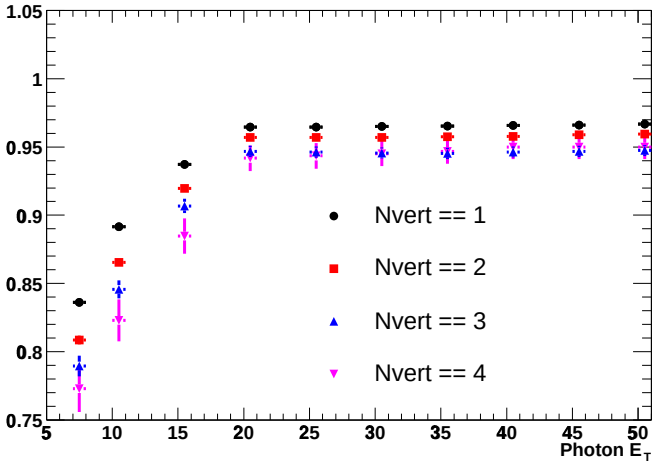

Figure 7.16: The isolation efficiency is plotted versus the assumed photon energy in $W \rightarrow e\nu$ events. The data are separated based upon the number of vertices in the event, and it can be seen that the efficiency falls as the number of multiple interactions increases.

GeV is

$$\epsilon(E_T^\gamma) = 0.89 + 0.0175 \times E_T^\gamma - 0.00104 \times (E_T^\gamma)^2 + 2 \times 10^{-5} \times (E_T^\gamma)^3, \quad (7.14)$$

and $\epsilon(E_T^\gamma) = 0.994$ for above 20 GeV. The error of the fit was measured to be 1% on the calorimeter isolation correction.

After applying the calorimeter isolation cut to the random cone, the number of 3-D tracks pointing at the cone was counted (**N3D**). For a track to be counted, it was required to point at either the central tower, or one of the two shoulder towers in the center of the cone. If only one track matched to the cluster towers, a p_T cut is applied. The efficiency of the cut was found to be very high shown in Figure 7.18 for data and MC, that is due to the strong correlation between calorimeter isolation and the number of final state particles traversing that area of the detector. Since the agreement was so good, no correction for the N3D cut was made to the MC efficiency.

After cutting on N3D, **Track Isolation** cut on the random cone was studied. The sum all of the tracks within the cone was calculated. The cut is found to be very efficient and the measured values in data and MC match within errors shown in Figure 7.19.

2nd CES cluster energiy cut is applied to the cone after requiring track isolation cut. Since the random cone is not supposed to be pointing at any object in the calorimeter, there is no first CES cluster. Thus, the highest energy cluster in the wedge is considered as the second cluster using the assumption that the

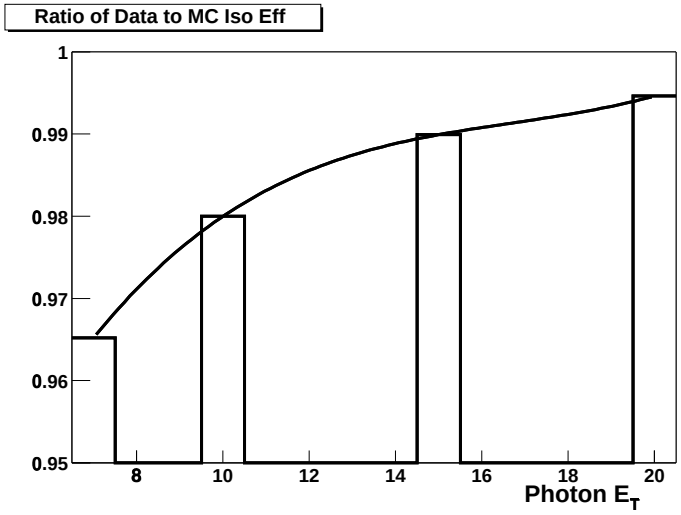

Figure 7.17: The ratio of the calorimeter isolation efficiency in W data to that in the Monte Carlo sample.

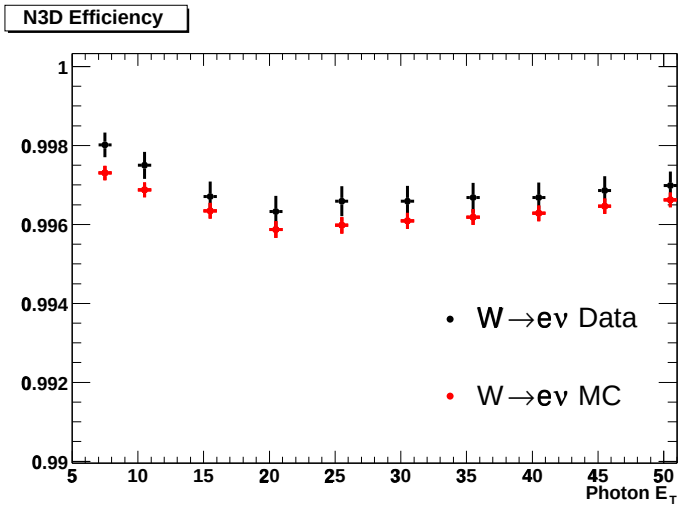

Figure 7.18: The efficiency of the N3D cut for data and MC as a function of photon E_T with the random cone method.

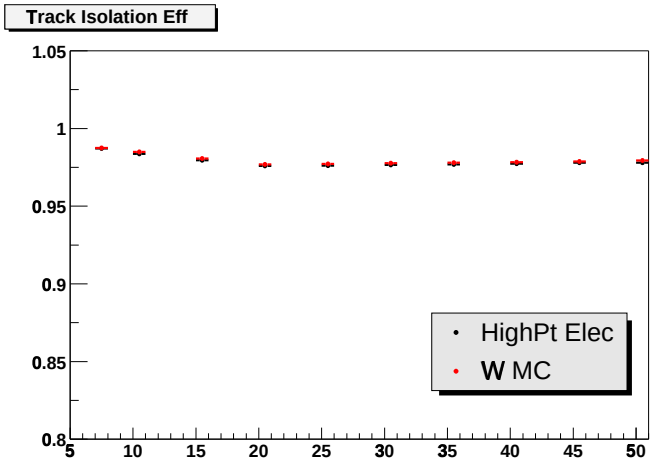

Figure 7.19: The efficiency of the track isolation cut for data and MC as a function of photon E_T.

photon always generates an electromagnetic cluster. The efficiency of this cut only considers additional clusters from underlying event and has no sensitivity of photon conversion. Figure 7.20 shows the efficiency of the 2nd CES cluster energy for data and MC. Since there is no dependence on photon E_T, a simple correction of 1% was applied to the MC efficiency.

In summary it was determined that only the calorimeter isolation and the second CES cluster energy cuts needed to be corrected. Table 7.12 shows the measured correction factor of each cut using random cone method.

Table 7.12: Correction factors to scale the MC in data. The calorimeter isolation depends on E_T^{γ} : $f(E_T) = 0.89 + 0.0175 \times E_T - 0.00104 \times E_T^2 + 2 \times 10^{-5} \times E_T^3$ for $E_T < 20$ GeV, and $f(E_T) = 0.98$ for $E_T > 20$ GeV.

Cut	Correction Factor	Error
Calorimeter Isolation	f(E_T)	$\pm$1.0%
N3D	1.0	$\pm$0.3%
Track Isolation	1.0	$\pm$0.3%
2nd CES Energy	0.995	$\pm$1.0%

7.5 Summary of the Photon ID Efficiencies

I measured the photon ID efficiencies for each photon ID cuts using two methods: 1) applying photon ID cuts to electron candidates regarding as photon candidates, 2) throwing a virtual cone randomly in the detector and measured the underlying energy activity, then derived the correction factor to scale the

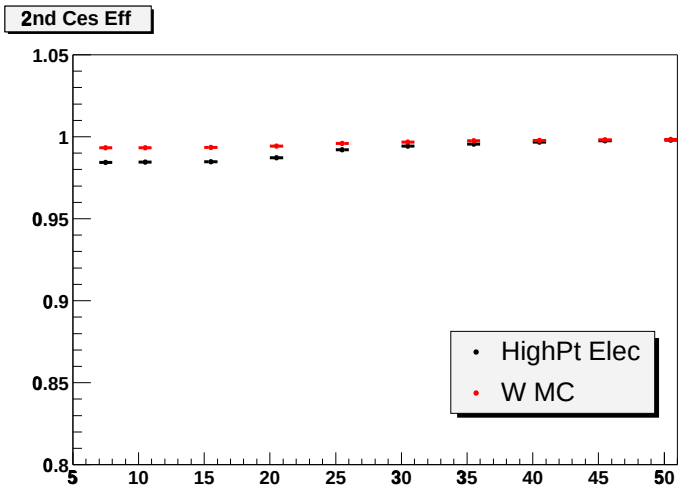

Figure 7.20: The efficiency of the cut for data and MC as a function of photon E_T.

$W\gamma$ MC shown in Table 7.13. I took the average of these correction factors and applied it to the photon in the MC. The errors in "Used in analysis" column are the systematic errors. Since the correction factor using single photon MC and diphoton MC are agree within statistical errors, I didn't use diphoton MC for "Used" value because it has smaller statistics.

The correction factor on the efficiency of the calorimeter isolation depends on E_T^γ:

$$f(E_T^\gamma) = 0.89 + 0.0175 \times E_T^\gamma - 0.00104 \times (E_T^\gamma)^2 + 2 \times 10^{-5} \times (E_T^\gamma)^3 \quad (7.15)$$
$$\text{for } E_T^\gamma < 20 \text{ GeV},$$
$$f(E_T^\gamma) = 0.98$$
$$\text{for } E_T^\gamma \geq 20 \text{ GeV}.$$

The square of quadratic sum of the other photon efficiency correction factors are 0.96 with a systematic uncertainty of 2.3%.

7.6 Summary of the Systematic Uncertainties

The following sources of systematic uncertainties are taken into account :

- 30 - 80% uncertainty on the photon fake rate is assigned depending on E_T^γ, detailed in Section 6.1.
- 0.4% uncertainty for the $|z_0| < 60$ cm cut in Equation 7.4.

Table 7.13: The summary of the correction factor of the photon ID efficiencies to scale the $W\gamma$ MC. Detail of $f(E_T^\gamma)$ is in Equation 7.15.

Cut	random cone	$Z \to ee(1)$	$Z \to ee(2)$	conv(γ)	conv(di-γ)
Iso	f(E_T)$\pm$0.01	1.01$\pm$0.005	–	–	–
N3D	1.0 $\pm$0.003	0.977$\pm$0.006	–	–	–
Trk Iso	1.0 $\pm$0.003	0.988$\pm$0.005	–	–	–
$\langle\chi^2_{\rm CES}\rangle$	–	0.980$\pm$0.004	0.979$\pm$0.004	1.01 $\pm$0.005	0.990$\pm$0.007
2nd strip	0.995$\pm$0.01	1.00 $\pm$0.003	1.00 $\pm$0.002	1.01 $\pm$0.019	1.02 $\pm$0.007
2nd wire	–	0.990$\pm$0.004	0.987$\pm$0.004	0.987$\pm$0.013	0.979$\pm$0.010

Cut	Used in analysis
Iso	f(E_T)$\pm$0.01
N3D	0.99$\pm$0.01
Trk Iso	0.99$\pm$0.005
$\langle\chi^2_{\rm CES}\rangle$	0.98$\pm$0.01
2nd strip	1.01$\pm$0.01
2nd wire	0.99$\pm$0.01

- The uncertainty on the muon trigger efficiencies for the CMUP is 0.7% and CMX is 0.6% (detailed in Section 3.4.3).

- 0.6% uncertainty due to the cosmic rejection in Equation 7.6.

- 0.7% (0.8%) uncertainty for the CMUP (CMX) muon identification shown in Table 7.1 and 7.2.

- 0.6% (0.3%) uncertainty for the CMUP (CMX) muon reconstruction shown in Equation 7.1.

- 2% due to the muon momentum scale uncertainty. The acceptance of the muon track p_T requirement is taken directly from Monte Carlo simulation. Therefore, it is also important to tune the scale and resolution of the track p_T in the Monte Carlo simulation to match those observed in the data. The muon track p_T enters into the acceptance calculation via both of the the muon p_T and $\not\!\!E_T$ selection.

  The muon track p_T scale and resolution are tuned using the $Z \to \mu\mu$ candidate events. The fraction of background events in this sample is well below $\sim$ 1%, so it is possible to make a direct comparison of the $Z \to \mu\mu$ invariant mass spectrum using data and Monte Carlo simulation. In order to determine the best value for the scaling factor, I performed χ^2 fits between them over a range of potential values. Figure 4.3 shows the invariant mass of different Z decay channels using data and Monte Carlo. Lower left is the $Z \to \mu\mu$ decay channel using the CMUP detector and lower right using the CMX detector.

- The photon energy scale uncertainty is 3%, shown in Section 4.2.

- The systematic uncertainty of the photon ID requirements is 2.3% detailed in Section 7.5.

- The uncertainty on the conversion rate is 1.5%. The series of the photon selection cuts successfully reject conversions because of the veto of the tracks towardd the EM tower discussed in Section 4.1. I estimated the efficiency of the photon originating from the $W\gamma$ production converting in the detector material using Monte Carlo, and found to be $10.21\pm0.25(\%)$. However, the material in the simulation is known to be underestimated by 30% [94]. The amount of materials in the inner tracking volume at conversion radius $r < 42$ cm is $15X_0(\%)$ and this indicates another extra $4.5\pm1.5X_0(\%)$ materials are present in data. Therefore the conversion probability in data is estimated to be $13.3\pm1.0X_0(\%)$. I applied the correction factor of (100.-13.3)/(100.-10.2)=0.97 to the Monte Carlo and assign the systematic uncertainty of 1.5%.

- The acceptance uncertainty is determined to be 2% for $W\gamma$ muon channel and 2.5% for $Z\gamma$ muon channel discussed in Section 5.3.

- The uncertainty in the luminosity is 6% (See Section 3.1.3).

- The systematics from the NLO k-factor are described in Section 5.3. This variation corresponds to a change of $\delta\mathrm{A}_{k\mathrm{factor}} = 2\%$ in acceptance and $\delta\sigma_{k\mathrm{factor}} = 3\%$ in the $W\gamma$ theoretical cross section prediction.

- The uncertainty of the $W\gamma$ cross section from the Parton Distribution Functions (PDF) is $\delta\mathrm{A}_{\mathrm{PDF}} = 0\%$ on acceptance and $\delta\sigma_{\mathrm{PDF}} = 5\%$ on the $W\gamma$ theoretical cross section calculation. The choice of the PDF in the MC has an effect on the acceptance since it changes the angular distributions of particles. Both of `WGAMMA` and `ZGAMMA` generators are the leading-order MC, therefore I chose the CTEQ5L [95] to model the initial state parton momentum distributions. Another five leading order MRST [96] PDF sets are chosen, but have no variation seen in acceptance of $W\gamma$. The 5% of the uncertainty is assigned to the theoretical cross section uncertainty.

- Systematics from the selection of Factorization scale is $\delta\mathrm{A}_F = 0\%$ on acceptance, and $\delta\sigma_{\mathrm{F}} = 2\%$ on the cross section prediction discussed in Section 5.2. The factorization scale is the minimum q^2 value calculated for photon emission with the `WGAMMA` and `ZGAMMA` programs. This is important as it also defines the maximum q^2 value for the `PYTHIA` fragmentation. By default, the factorization scale is set to the collision $\hat{s}$ and used for large sample generation. To study the effect of the factorization scale on the acceptance and the cross section, the q^2 scale was varied by $2\hat{s}$, $1.5\hat{s}$, $2/3\hat{s}$,

and $1/2\hat{s}$. The variation in the five cross sections was taken as the systematic uncertainty from the factorization scale and is 2%. No variation has seen on the acceptance.

Chapter 8

Results

In this Chapter all the elements detailed in the previous sections are combined in the calculation of the $W\gamma$ yields and the cross section in Section 8.1. The kinematical distributions for $W\gamma$ candidates are shown. The cross section for $p\bar{p} \to W\gamma$, $W \to \mu\nu$ calculated and compared to the Standard Model prediction in Section 8.2.

8.1 $W\gamma$ Events Yields

In the muon channel 128 events are observed compared to the Standard Model expectation of $142.4 \pm 1.51(\text{stat.}) \pm 9.35(\text{sys.})$. Note that the error on the luminosity and the Standard Model expectation affect to the Monte Carlo predictions but not to the QCD background. Figures 8.1-8.3 show the kinematical distributions for the data, the signal and background expectation for the $W\gamma \to \mu\nu\gamma$ channel using CMUP, CMX and CMUP+CMX muons. The photon E_T, $\Delta R(\mu, \gamma)$, transverse mass and cluster transverse mass distributions are shown, respectively.

Table 8.1: Expected and observed numbers of events in the $W\gamma \to \mu\nu\gamma$ analysis for CMUP and CMX muons. The statistical and experimental systematic errors are shown.

	CMUP	CMX
$W\gamma \to \mu\nu\gamma$	$63.58 \pm 1.17(\text{stat.}) \pm 3.17(\text{sys.})$	$31.60 \pm 0.88(\text{stat.}) \pm 1.57(\text{sys.})$
QCD background	$17.89 \pm 0.00(\text{stat.}) \pm 4.90(\text{sys.})$	$9.69 \pm 0.00(\text{stat.}) \pm 2.63(\text{sys.})$
$W\gamma \to \tau\nu\gamma$	$1.44 \pm 0.17(\text{stat.}) \pm 0.07(\text{sys.})$	$0.86 \pm 0.14(\text{stat.}) \pm 0.04(\text{sys.})$
$Z\gamma \to \mu\mu\gamma$	$11.74 \pm 0.26(\text{stat.}) \pm 0.59(\text{sys.})$	$5.63 \pm 0.19(\text{stat.}) \pm 0.28(\text{sys.})$
total SM+BG	$94.66 \pm 1.21(\text{stat.}) \pm 6.17(\text{sys.})$	$47.78 \pm 0.91(\text{stat.}) \pm 2.75(\text{sys.})$
Data	93	35

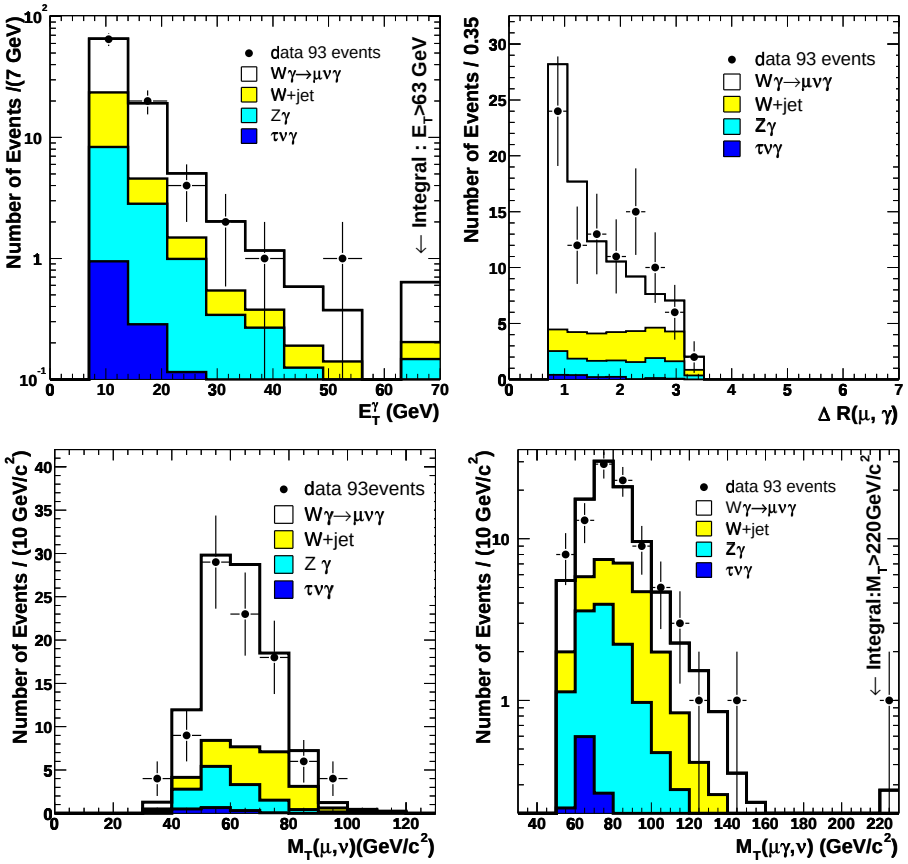

Figure 8.1: Several kinematic distributions for the data (points), the signal and background expectations for the $W\gamma \to \mu\nu\gamma$ channel using CMUP muons. The open histogram is for the $W\gamma \to \mu\nu\gamma$ signal expectation, the solid yellow is for the QCD background, the turquoise is for the $Z\gamma \to \mu\mu\gamma$ background and the dark blue histogram is for $W\gamma \to \tau\nu\gamma \to \bar{\nu}\nu\nu\mu\gamma$ background.

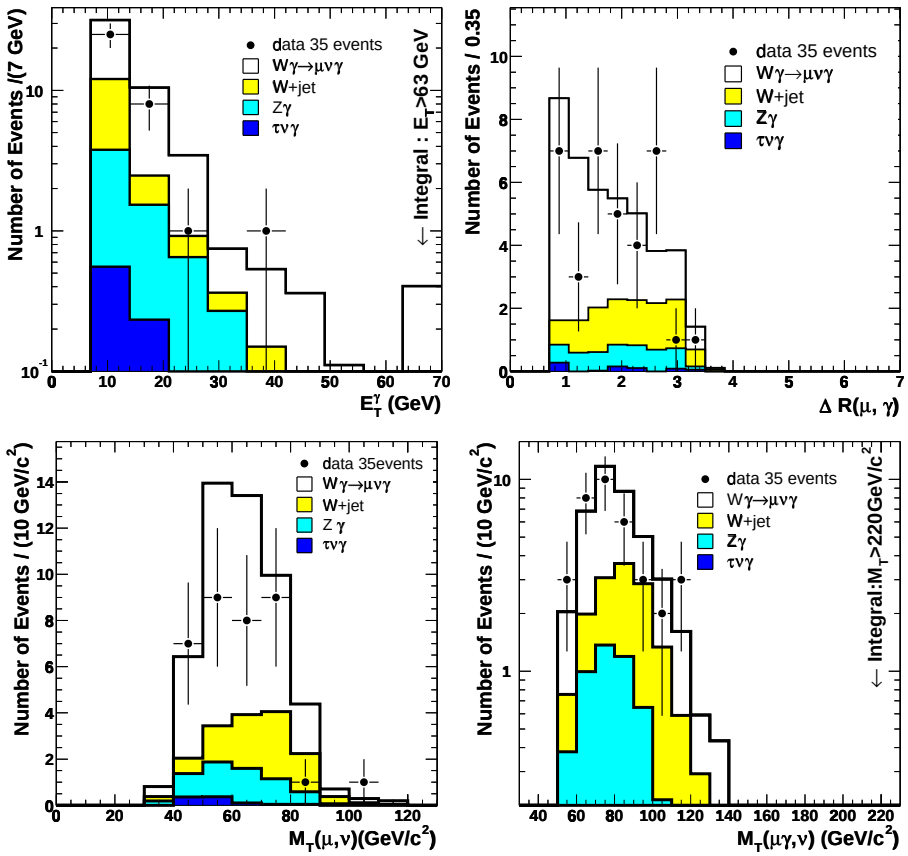

Figure 8.2: Several kinematic distributions for the data (points), the signal and background expectations for the $W\gamma \rightarrow \mu\nu\gamma$ channel using CMX muons. The open histogram is for the $W\gamma \rightarrow \mu\nu\gamma$ signal expectation, the solid yellow is for the QCD background, the turquoise is for the $Z\gamma \rightarrow \mu\mu\gamma$ background and the dark blue histogram is for $W\gamma \rightarrow \tau\nu\gamma \rightarrow \bar{\nu}\nu\nu\mu\gamma$ background.

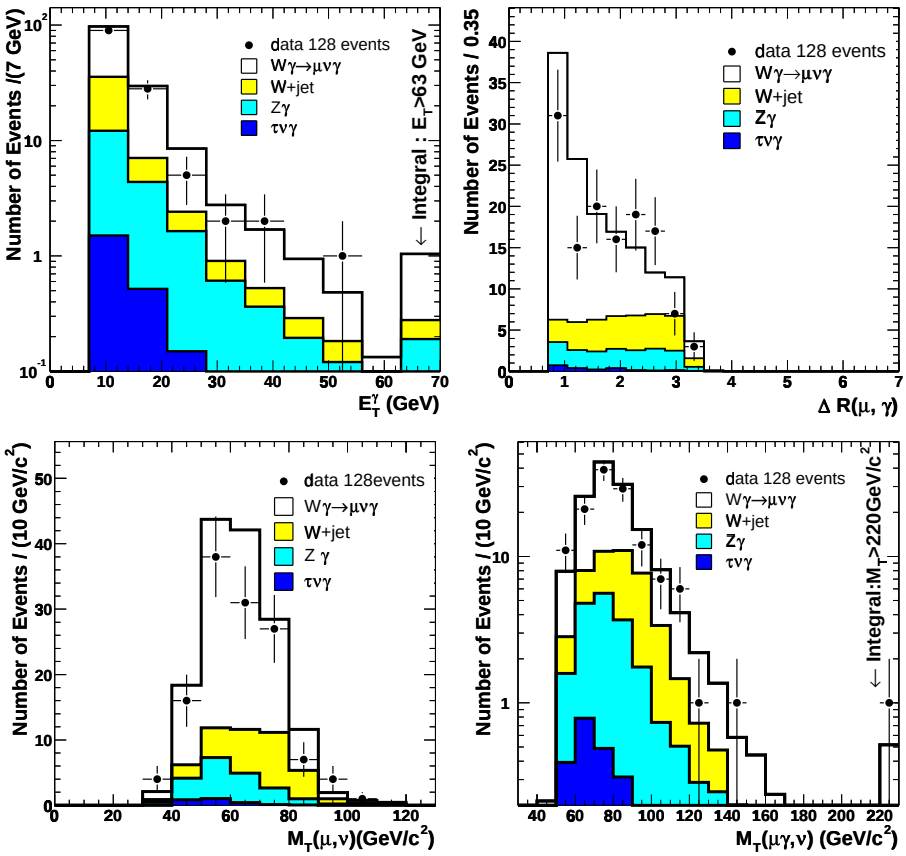

Figure 8.3: Several kinematic distributions for the data (points), the signal and background expectations for the $W\gamma \to \mu\nu\gamma$ channel. The open histogram is for the $W\gamma \to \mu\nu\gamma$ signal expectation, the solid yellow is for the QCD background, the turquoise is for the $Z\gamma \to \mu\mu\gamma$ background and the dark blue histogram is for $W\gamma \to \tau\nu\gamma \to \bar{\nu}\nu\nu\mu\gamma$ background.

In this thesis I focused on the study of $W\gamma$ production with the $W \to \mu\nu$ decay. To minimize the statistical uncertainties possible with the CDF data, the result of the electron channelof the $W\gamma$ production [97] is combined with the results of the muon channel. Electron from W decay is required to be $E_T >$ 25 GeV, which is detected in the central and plug electromagnetic calorimeters, and a large $\not\!\!E_T > 25$ GeV to form a W boson. Then an isolated photon with $E_T > 7$ GeV is required in the event. 195 event candidates from the $W\gamma$ electron channel were observed compared to the Standard Model expectation of 194.1 ± 1.51(stat.) $\pm$ 19.0(sys.). The electron and muon results are given in Table 8.2. separately. The combined electron and muon results is given in Table 8.3. Figure 8.4 shows the kinematical distributions for the $W\gamma \to l\nu\gamma$ production combining overall electron and muon channel candidate events.

Table 8.2: Expected and observed numbers of events combining the central and plug electron, and CMUP and CMX muon in $W\gamma \to l\nu\gamma$ analysis. The statistical and the experimental systematic errors are shown.

	Electron	Muon
$W\gamma \to l\nu\gamma$	126.8 ± 1.49(stat.) ± 5.60(sys.)	95.18 ± 1.46(stat.) ± 4.69(sys.)
QCD background	59.53 ± 0.0(stat.) ± 18.05(sys.)	27.59 ± 0.0(stat.) ± 7.53(sys.)
$W\gamma \to \tau\nu\gamma$	1.50 ± 0.16(stat.) ± 0.07(sys.)	2.30 ± 0.22(stat.) ± 0.11(sys.)
$Z\gamma \to ll\gamma$	6.30 ± 0.18(stat.) ± 0.28(sys.)	17.37 ± 0.32(stat.) ± 0.90(sys.)
total SM+BG	194.1 ± 1.51(stat.) ± 19.0(sys.)	142.4 ± 1.51(stat.) ± 9.35(sys.)
Data	195	128

Table 8.3: Expected and observed numbers of events combining the electron and muon $W\gamma \to l\nu\gamma$ analysis. The statistical and the experimental systematic errors are shown.

$W\gamma \to l\nu\gamma$	221.9 ± 2.09(stat.) ± 9.45(sys.)
QCD background	87.12 ± 0.0(stat.) ± 25.58(sys.)
$W\gamma \to \tau\nu\gamma$	3.80 ± 0.27(stat.) ± 0.17(sys.)
$Z\gamma \to ll\gamma$	23.67 ± 0.37(stat.) ± 1.10(sys.)
total SM+BG	336.5 ± 2.14(stat.) ± 27.66(sys.)
Data	323

8.2 $W\gamma$ Cross Section Measurement

I extract the cross section for $W\gamma$ production times the branching ratio of $W \to l\nu$ in the kinematic range of $\Delta R(l,\gamma) > 0.7$ and $E_T^\gamma > 7$ GeV using photons

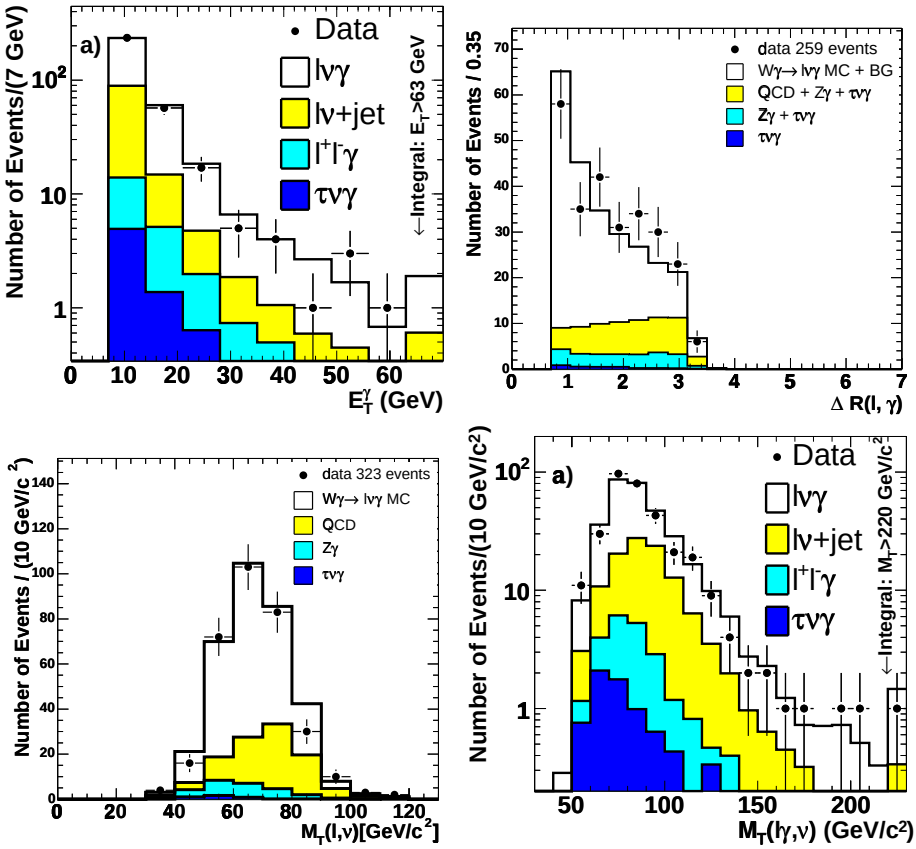

Figure 8.4: Several kinematic distributions for the data (points), the signal and background expectations for the $W\gamma \rightarrow l\nu\gamma$ channels in the central and plug electrons, CMUP and CMX muons. The open histogram is for the $W\gamma \rightarrow l\nu\gamma$ signal expectation, the solid yellow is for the QCD background, the turquoise is for the $Z\gamma \rightarrow ll\gamma$ background and the dark blue histogram is for $W\gamma \rightarrow \tau\nu\gamma \rightarrow \bar{\nu}\nu\nu l\gamma$ background.

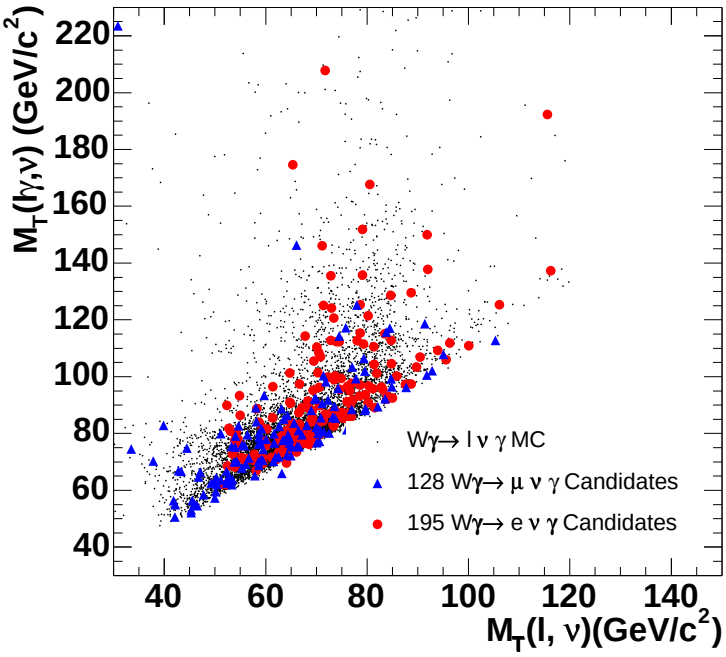

Figure 8.5: The cluster transverse mass versus the transverse mass for the electron (red circle) and muon (blue triangle) channels of the $W\gamma$ candidates. The small black circle shows the Standard Model expectations.

within $|\eta_\gamma| < 1.0$. The cross section is given by

$$\sigma = \frac{N_{Data} - N_{BG}}{(A \cdot \epsilon)_{W\gamma} \cdot \epsilon_{trig} \cdot \epsilon_{corr} \cdot \int \mathcal{L}\, dt}, \tag{8.1}$$

where N_{Data} is the number of observed events, N_{BG} the number of background events, $(A \cdot \epsilon)_{W\gamma}$ is the acceptance times efficiency for this kinematic range in MC and ϵ_{corr} the correction to reproduce the data efficiency detailed in Section 7.1. With $N^{exp}_{W\gamma MC} = \sigma^{W\gamma MC}_{E_T>5,\Delta R>0.2} \cdot (A \cdot \epsilon)_{W\gamma} \cdot \epsilon_{trig} \cdot \epsilon_{corr} \cdot \int \mathcal{L}\, dt$ being the expected number of $W\gamma$ events, this simplifies to

$$\sigma = \frac{N_{Data} - N_{BG}}{N^{exp}_{W\gamma MC}} \cdot \sigma^{W\gamma MC}_{E_T>5,\Delta R>0.2} \tag{8.2}$$

for the kinematic range of the `WGAMMA` MC. In order to correct the kinematic range of the measurement we can simply scale this by the ratio of the theoretical cross section in the two kinematic regions,

$$\frac{\sigma^{W\gamma MC}_{E_T>7,\Delta R>0.7}}{\sigma^{W\gamma MC}_{E_T>5,\Delta R>0.2}} = \frac{19.3 \text{ pb}}{44.7 \text{ pb}} = 0.432. \tag{8.3}$$

The cross section in the kinematic range $\Delta R > 0.7$ and $E_T^\gamma > 7$ GeV is given simply by

$$\begin{aligned} \sigma &= \frac{N_{Data} - N_{BG}}{N^{exp}_{W\gamma MC}} \cdot \sigma^{W\gamma MC}_{E_T>5,\Delta R>0.2} \cdot \frac{\sigma^{W\gamma MC}_{E_T>7,\Delta R>0.7}}{\sigma^{W\gamma MC}_{E_T>5,\Delta R>0.2}} \\ &= \frac{N_{Data} - N_{BG}}{N^{exp}_{W\gamma MC}} \cdot \sigma^{W\gamma MC}_{E_T>7,\Delta R>0.7}. \end{aligned} \tag{8.4}$$

The cross sections results for $W\gamma$ are

$$\begin{aligned} \sigma(p\bar{p} \to \mu\nu\gamma)_{\text{CMUP}} &= 18.8 \pm 2.9(\text{stat.}) \pm 1.8(\text{syst.}) \pm 1.4(\text{lum.}) \text{ pb} \\ \sigma(p\bar{p} \to \mu\nu\gamma)_{\text{CMX}} &= 11.5 \pm 3.6(\text{stat.}) \pm 1.8(\text{syst.}) \pm 0.9(\text{lum.}) \text{ pb}. \end{aligned} \tag{8.5}$$

Summing up CMUP and CMX muons and taking into account the correlations of the systematic uncertainties, the $W\gamma$ muon channel cross section is

$$\sigma(p\bar{p} \to \mu\nu\gamma) = 16.3 \pm 2.3(\text{stat.}) \pm 1.8(\text{syst.}) \pm 1.2(\text{lum.}) \text{ pb}. \tag{8.6}$$

Combining the electron and muon decay channels, assuming lepton universality, and taking into account the correlations of the systematic uncertainties, combined cross section yields

$$\sigma(p\bar{p} \to l\nu\gamma) = 18.1 \pm 1.6(\text{stat.}) \pm 2.4(\text{syst.}) \pm 1.2(\text{lum.}) \text{ pb}. \tag{8.7}$$

The NLO theoretical prediction for the cross section is 19.3 ± 1.4(th.) pb. The measured cross section is consistent with the Standard Model expectation.

Chapter 9

Conclusion

The cross section of $W + \gamma$ production with the W boson decaying into a muon and neutrino from $p\bar{p}$ collider at $\sqrt{s} = 1.96$ TeV has been measured. The data were collected from March 2002 through September 2003, and correspond to an integrated luminosity of about 200pb^{-1}. I have observed 128 candidate events with the Standard Model expection of 142.4 ± 1.51(stat.) ± 9.35(sys.). The cross section with $E_T(\gamma) > 7$ GeV and $\Delta R(l, \gamma) > 0.7$ is measured to be

$$\sigma(p\bar{p} \to \mu\nu\gamma) = 16.3 \pm 2.3(\text{stat.}) \pm 1.8(\text{syst.}) \pm 1.2(\text{lum.}) \text{ [pb]} \quad (9.1)$$

The combined cross section from the W boson electron and muon decay channel is

$$\sigma(p\bar{p} \to l\nu\gamma) = 18.1 \pm 1.6(\text{stat.}) \pm 2.4(\text{syst.}) \pm 1.2(\text{lum.}) \text{ [pb]}. \quad (9.2)$$

They agree well with the theoretical prediction of 19.3 ± 1.4(th.) [pb].

In addition to the cross section measurements, I compared the SM predictions for several kinematic varuables with data for $E_T(\gamma) > 7$ GeV and $\Delta R(l, \gamma) > 0.7$. The data are in good agreement with the SM expectation.

Electroweak cross section measurements from the CDF and DØ are summarized in Figure 9.1 [74, 98]. The electroweak sector has been successfully tested using data from the Tevatron.

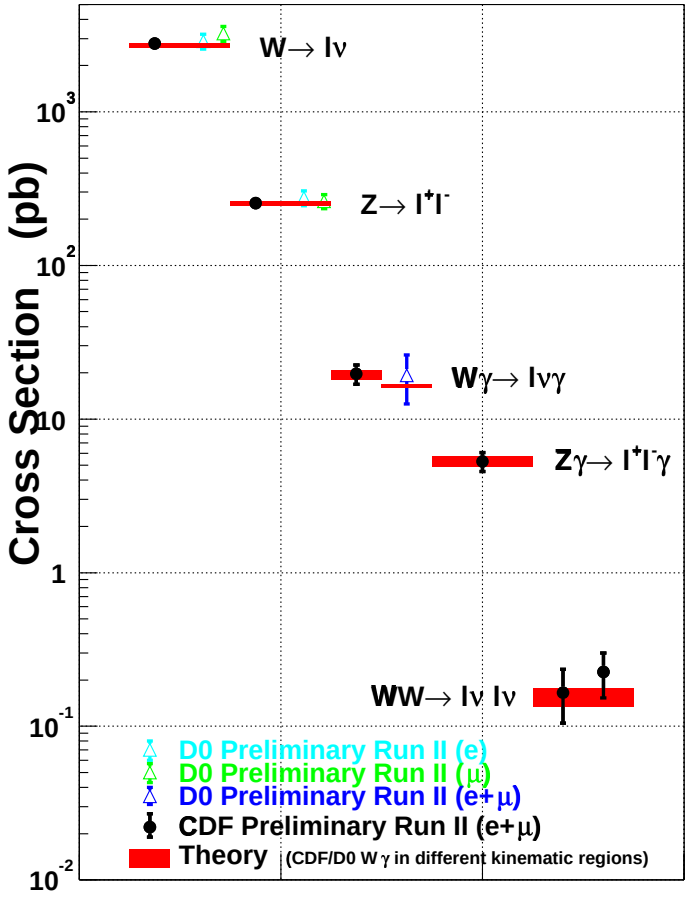

Figure 9.1: Electroweak cross section measurements from the CDF and DØ. For $W\gamma$ cross section measurements, CDF requires $E_T^\gamma > 7$ GeV and $\Delta R(l,\nu) > 0.7$ and DØ requires $E_T^\gamma > 8$ GeV and $\Delta R(l,\nu) > 0.7$.

Bibliography

[1] S. Weinberg, "A Model of Leptons", Phys. Rev. Lett. **19** (1967) 1264.

[2] A. Salam, P. 367 of "Elementary Particle Theory", ed N. Svartholm, 1961.

[3] S.L. Glashow, J. Iliopoulos, and L. Maiani, "Weak Interactions with Lepton-Hadron Symmetry", Phys. Rev. **D2** (1970) 1285.

[4] Super-Kamiokande Collaboration, S. Fukuda *et al.*, "Determination of Solar Neutrino Oscillation Parameters using 1496 Days of Super-Kamiokande-I Data", Phys. Lett. B **539** (2002) 179.

[5] KamLAND Collaboration, T. Araki *et al.*, "Measurement of Neutrino Oscillation with KamLAND: Evidence of Spectral Distortion", hep-ex/0406035, *Submitted to Phys. Rev. Lett.*

[6] SNO Collaboration, S.N. Ahmed *et al.*, "Measurement of the Total Active ^{8}B Solar Neutrino Flux at the Sudbury Neutrino Observatory with Enhanced Neutral Current Sensitivity", Phys. Rev. Lett. **92** (2004) 181301.

[7] S. Eidelman *et al.*, "Particle Data Group", Phys. Lett. B **592** (2004) 1.

[8] M. Veltman, "Perturbation Theory of Massive Yang-Mills fields", Nucl. Phys. B **35** (1968) 637.

[9] G. 'tHooft, "Renormalizable Lagrangians for Massive Yang-Mills Fields", Nucl. Phys. B **35** (1971) 167.

[10] G. 'tHooft and M. Veltman, "Combinatorics of Gauge Fields", Nucl. Phys. B **50** (1972) 318.

[11] M. Kobayashi and T. Maskawa, Prog. Theor. Phys. **49** (1973) 652.

[12] N. Cabibbo, Phys. Rev. Lett. **10** (1963) 531.

[13] K. Hagiwara, R.D. Peccei, D. Zeppenfeld and K. Hikasa, "Probing the weak boson sector in $e^+e^- \to W^+W^-$", Nucl. Phys. B **282** (1987) 253.

[14] U. Baur and D. Zeppenfeld, "Probing the $WW\gamma$ vertex at future hadron colliders", Nucl. Phys. B **308** (1988) 127.

[15] K. Gaemers and G. Gounaris, Z. Phys. C **1** (1979) 259.

[16] U. Baur and E.L. Berger, "Probing the $WW\gamma$ vertex at the Fermilab Tevatron Collider", Phys. Rev. D **41** (1990) 1476.

[17] J. Cortés, K. Hagiwara and F. Herzog, "Testing the $WW\gamma$ coupling of the standard model at $p\bar{p}$ colliders", Nucl. Phys. B **278** (1986) 26.

[18] U. Baur, S. Errede and G. Landsberg, "Rapidity correlations in $W\gamma$ production at hadron colliders", Phys. Rev. D **50** (1994) 1917.

[19] OPAL Collaboration, K. Ackerstaff *et al.*, "Measurement of the triple gauge boson coupling $\alpha = W\phi$ from W^+W^- production in e^+e^- collisions at $\sqrt{s} = 161$ GeV", Phys. Lett. B **397** (1997) 147.

[20] OPAL Collaboration, K. Ackerstaff *et al.*, "Measurement of triple gauge boson couplings from W^+W^- production at $\sqrt{s} = 172$ GeV", Eur. Phys. J. C **2** (1998) 597.

[21] OPAL Collaboration, K. Ackerstaff *et al.*, "W^+W^- production and triple gauge boson couplings at LEP energies up to 183 GeV", Eur. Phys. J. C **8** (1999) 191.

[22] OPAL Collaboration, K. Ackerstaff *et al.*, "Measurement of triple gauge boson couplings from W^+W^- production at LEP energies up to 189 GeV", Eur. Phys. J. C **19** (2001) 1.

[23] DELPHI Collaboration, P. Abreu *et al.*, "Measurement and interpretation of the W-pair cross-section in e^+e^- interactions at 161 GeV", Phys. Lett. B **397** (1997) 158.

[24] L3 Collaboration, M. Acciarri *et al.*, "Pair-production of W bosons in e^+e^- interactions at $\sqrt{s}$ =161 GeV", Phys. Lett. B **398** (1997) 223.

[25] L3 Collaboration, M. Acciarri *et al.*, "Measurements of mass, width and gauge couplings of the W boson at LEP", Phys. Lett. B 413 (1997) 176.

[26] ALEPH Collaboration, R. Barate *et al.*, "Measurement of triple gauge-boson couplings at 172 GeV", Phys. Lett. B **422** (1998) 369.

[27] DELPHI Collaboration, P. Abreu *et al.*, "Measurement of trilinear gauge couplings in e^+e^- collisions at 161 GeV and 172 GeV", Phys. Lett. B **423** (1998) 194.

[28] DELPHI Collaboration, P. Abreu *et al.*, "Measurements of the trilinear gauge boson couplings WWV ($V \equiv \gamma, Z$) in e^+e^- collisions at 183 GeV", Phys. Lett. B **459** (1999) 382.

[29] DELPHI Collaboration, P. Abreu *et al.*, "Measurement of triple-gauge-boson couplings of the W boson at LEP", Phys. Lett. B **467** (1999) 171.

[30] DELPHI Collaboration, P. Abreu *et al.*, "Measurement of trilinear gauge boson couplings WWV, $(V \equiv \gamma, Z)$ in e^+e^- collisions at 189 GeV", Phys. Lett. B **502** (2001) 9.

[31] ALEPH Collaboration, A. Heister *et al.*, "Measurement of triple gauge-boson couplings at LEP energies up to 189 GeV", Eur. Phys. J. C **21** (2001) 423.

[32] OPAL Collaboration, G. Abbiendi *et al.*, "Measurement of charged current triple gauge boson couplings using W pairs at LEP", Eur. Phys. J. C **33** (2004) 463.

[33] L3 Collaboration, M. Acciarri *et al.*, "Measurement of triple-gauge-boson couplings of the W boson at LEP", Phys. Lett. B **467** (1999) 171.

[34] L3 Collaboration, M. Acciarri *et al.*, "Production of single W bosons at LEP", Phys. Lett. B **403** (1997) 168.

[35] L3 Collaboration, M. Acciarri *et al.*, "Production of single W bosons in e^+e^- interactions at $130 \leq \sqrt{s} \leq 183$ GeV and limits on anomalous $WW\gamma$ couplings", Phys. Lett. B **436** (1998) 417.

[36] ALEPH Collaboration, R. Barate *et al.*, "A study of single W production in e^+e^- collisions at $\sqrt{s}$= 161 - 183 GeV", Phys. Lett. B **462** (1999) 389.

[37] L3 Collaboration, M. Acciarri *et al.*, "Production of single W bosons at $\sqrt{s}$=189 GeV and measurement of $WW\gamma$ gauge conplings", Phys. Lett. B **487** (2000) 229.

[38] L3 Collaboration, P. Achard *et al.*, "Production of single W bosons at LEP and measurement of $WW\gamma$ gauge coupling parameters", Phys. Lett. B **547** (2002) 151.

[39] ALEPH Collaboration, R. Barate *et al.*, "Measurement of triple gauge WW couplings at LEP2 using photonic events", Phys. Lett. B **445** (1998) 239.

[40] G. Gounaris, J.-L. Kneur, D. Zeppenfeld *et al.*, "Triple Gauge Boson Couplings", CERN 96-01 (1996), hep-ph/9601233.

[41] LEP Collaborations ALEPH, DELPHI, L3, OPAL., LEP Electroweak Working Group, and SLD Electroweak and Heavy Flavour Groups. "A Combination of Preliminary Electroweak Measurements and Constraints on the Standard Model", `http://lepewwg.web.cern.ch/LEPEWWG/stanmod/`, CERN-EP/2003-091, hep-ex/0312023.

[42] CDF Collaboration, F. Abe *et al.*, "Measurement of W-Photon Couplngs in $p-\bar{p}$ Collisions at $\sqrt{s} = 1.8$ TeV", Phys. Rev. Lett. **74** (1995) 1936.

[43] CDF Collaboration, F. Abe *et al.*, "Limits on WWZ and $WW\gamma$ Couplings from WW and WZ Production in $p\bar{p}$ Collisions at $\sqrt{s} = 1.8$ TeV", Phys. Rev. Lett. **75** (1995) 1017.

[44] DØ Collaboration, B. Abbott *et al.*, "Limits on anomalous $WW\gamma$ and WWZ couplings", Phys. Rev. D **58** (1998) 031102.

[45] DØ Collaboration, B. Abbott *et al.*, "Limits on $WW\gamma$ and WWZ couplings from W boson pair production", Phys. Rev. D **58** (1998) 051101.

[46] DØ Collaboration, B. Abbott *et al.*, "Studies of WW and WZ production and limits on anomalous $WW\gamma$ and WWZ couplints ", Phys. Rev. D **60** (1999) 072002.

[47] DØ Collaboration, B. Abbott *et al.*, "Limits on anomalous $WW\gamma$ and WWZ couplings from $WW/WZ \to e\nu jj$ production", Phys. Rev. D **62** (2000) 052005.

[48] C.W. Smith and C.D. Curtis, "Operation of the Fermilab H^- Magnetron Source", Proc. 4th Int. Symp. on the Production and Neutralization of Negative Ions and Beams, Brookhaven, US, AIP Conf. Proc. No. 158 (1986) 425.

[49] D.A. Finley, J. Marriner and N.V. Mokhov, "Tevatron Status and Future Plans", Fermilab Technical Report, Fermilab-Conf-96/408, 1996.

[50] S.D. Holmes *et al.*, "The Fermilab Upgrade", Proc. of IEEE Part. Accel. Conf., pp. 436-468, vol. 1, Chicago, 1989.

[51] J.A. MacLachlan, "400 MeV Upgrade for the Fermilab Linac", Proc. of IEEE Part. Accel. Conf., pp. 950-952, vol. 2, Chicago, 1989.

[52] D.E. Young and R.J. Noble, "400-MeV Upgrade for the Fermilab Linac", Fermilab Technical Report, Fermilab-Conf-89/198, 1989.

[53] E. Hubbard *et al.*, "Booster Synchrotron", Fermilab Technical Report, TM-405, 1973.

[54] M. Popovic and C. Akenbrandt, "Performance and Measurement of the Fermilab Booster", Fermilab Technical Design Report, Fermilab-Conf-98/198, 1998.

[55] R.C. Webber, "Fermilab Booster Low Level RF System Upgrades", Proc. of IEEE Part. Accel. Conf., pp. 2687-2689, vol 4, Dallas, 1995.

[56] M.D. Church and J.P. Marriner, "The Antiproton Sources: Design and Operation", Ann. Rev. Nucl. Part. Sci. 43 (1993) 253.

[57] A. Ruggiero, "The Fermilab Tevatron I Debuncher Ring", IEEE Trans. Nucl. Sci. **30** (1983) 2478.

[58] B. Austin *et al.*, "Fast Betatron Cooling in the Debuncher Ring for the Fermilab Tevatron I Project", IEEE Trans. Nucl. Sci. **30** (1983) 2593.

[59] J. Marriner, "Stochastic Cooling Overview", Fermilab-Conf-03-158, 2003.

[60] H. Edwards, "The Tevatron Energy Doubler: A Superconducting Accelerator", Ann. Rev. Nucl. Part. Sci. **35** (1985) 605.

[61] CDF Collaboration, "The CDF II Detector Technical Design Report", FERMILAB-96-390-E.

[62] CDF Collaboration, F. Abe *et al.*, "Proposal for Enhancement of the CDF II Detector: An Inner Silicon Layer and A Time of Flight Detector", Fermilab-Proposal-909.

[63] CDF Collaboration, P. Markel *et al.*, "CDF Run IIb Silicon: The new innermost layer", Proc. of IEEE-NSS-2003, FERMILAB-CONF-03/374-E.

[64] CDF Collaboration, T.K. Nelson, "The CDF-II silicon tracking system", Nucl. Instrum. Methods A **360** (1995) 137.

[65] CDF Collaboration, T. Affolder *et al.*, "CDF Central Outer Tracker", Fermilab-Pub-03-355-E (2003), Submitted to Nucl. Instrum. Methods.

[66] L. Balka *et al.*, "The CDF Central Electromagnetic Calorimeter", Fermilab-Pub-87-172-E, Nucl. Instrum. Methods, A **267** (1988) 272.

[67] G. Ascoli *et al.*, "CDF Central Muon Detector", FERMILAB-PUB-87/181-E, Nucl. Instrum. Methods A **268** (1988) 33.

[68] J. Elias *et al.*, "Liminosity Monitor Based on Cherenkov Counters for $p\bar{p}$ Colliders", Fermilab-Pub-99/191, Nucl. Instrum. Meth. A **441** (2000) 366.

[69] D. Acosta *et al.*, "The CDF Cherenkov Luminosity monitor", Fermilab-Pub-01-031-E, Nucl. Instrum. Meth. A **461** (2001) 540.

[70] D. Acosta *et al.*, "The performance of the CDF Luminosity Monitor", Nucl. Instrum. Meth. A **494** (2002) 57.

[71] R.J. Yarema *et al.*, "A fast, wide range charge integrator and encorder ASIC for photomultiplier tubes", IEEE Trans. on Nuclear Science, Vol 4 (1993) 750; R.J. Yarema *et al.*, "A high speed, wide dynamic range digitizer

for photomultiplier tubes", Ptoceedings 6th Pisa Meeting on Advanced Detectors, La Biodola, Isola d'Elba, Italy, May 22-28, 1994.

[72] A. Aldarese *et al.*, "SVT: an online Silicon Vertex Tracker for the CDF upgrade", Proceedings 7th Pisa Meeting on Advanced Detectors, La Biodola, Isola d'Elba, Italy, May 25-31, 1997. FERMILAB-CONF-97/244-E.

[73] S. Klimenko, J. Konigsberg and T.M. Liss, "Averaging of the Inelastic Cross Sections Measured by the CDF and the E811 Experiments", FERMILAB-FN-0741.

[74] CDF Collaboration, "First Measurements of Inclusive W and Z Cross Sections from Run II of the Tevatron Collider", *Accepted for the publication of Phys. Rev. Lett.*

[75] P.J. Sutton, A.D. Martin, R.G. Roberts and W.J. Stirling, "Parton distributions for the pion extracted from Drell-Yan and prompt photon experiments", Phys. Rev. D **45** (1992) 2349; P.J. Rijken and W.L. van Neervan, "Order α_s^2 contributions to the Drell-Yan cross section at fixed target energies", Phys. Rev. D **51** (1995) 44; R. Hamberg, W.L. can Neervan and W.B. Kilgore, "A complete calculation of the order α_s^2 correction to the Drell-Yan K-factor", Nucl. Phys. B**359** (1991) 343; R.V. Harlander and W.B. Kilgore, "Next-to-Next-to-Leading Order Higgs Production at Hadron Colliders", Phys. Rev. Lett. **88** (2002) 201801.

[76] E.L. Berger, D. DiBitonto, M. Jacob and W.J. Stirling, "The minimum invariant mass - A Technique for heavy quark searches at collider energy", Phys. Lett. **140B** (259) 1984.; V. Berger, A.D. Martin and R.J.N. Phillips, "Evidence for the t-quark in $p\bar{p}$ collider data?" Phys. Lett. **125B** (1983) 339.

[77] U. Baur and E.L. Berger, "Probing the weak-boson sector in $Z\gamma$ production at hadron colliders", Phys. Rev. D **47** (1993) 4889.

[78] G.P. Lepage, "A New Algorithm for Adaptive Multidimensional Integration", J. Comput. Phys. **27** (1978) 192.

[79] V.D. Berger, R.J.N. Phillips, "Collider Physics", Section 11.

[80] U. Baur, S. Keller and D. Wackeroth, "Electroweak Radiative Corrections to W Boson Production in Hadronic Collisions", Phys. Rev. D **59** (1999) 013002.

[81] M. Lancaster and D. Waters, "A Monte Carlo Program for W Production with Electroweak Radiative Corrections", CDF-Note 5240.

[82] T. Sjöstrand, L. Lönnblad, S. Mrenna, P. Skands, "Pythia 6.2, Physics and Manual", hep-ph/0108264, LU-TP 01-21.

[83] A. Pukhov, E. Boos, M. Dubinin, V. Edneral, V. Ilyin, D. Kovalenko, A. Kryukov, V. Savrin, S. Shichanin, A. Semenov, "CompHEP - a package for evaluation of Feynman diagrams and integration over multi-particle phase space", hep-ph/9908288.

[84] W.J. Marciano and A. Stirlin, "Electroweak radiative corrections to tau decay", Phys. Rev. Lett. **61** (1988) 1815.

[85] T. van Ritbergen and R.G. Stuart, "Complete 2-Loop Quantum Electrodynamic Contributions to the Muon Lifetime in the Fermi Model", Phys. Rev. Lett. **82** (1999) 488.

[86] Apprication Software Group, Compution and Network Division, CERN, Geneva, "GEANT : Detector Description and Simulation Tool", CERN Program Library Long Writeup W5013.

[87] U. Baur, T. Han and J. Ohnemus, "QCD corrections to hadronic $W\gamma$ production with nonstandard $WW\gamma$ couplings," Phys. Rev. D **48** (1993) 5140.

[88] CDF Collaboration, F. Abe *et al.*, "Prompt photon cross section measurement in $p\bar{p}$ collisions at $\sqrt{s}$=1.8 TeV", Phys. Rev. D **48** (1993) 2998.

[89] CDF Collaboration, D. Acosta *et al.*, "Measurement of the Cross Section for Prompt Diphoton Production in $p\bar{p}$ Collisions at $\sqrt{s} = 1.96$ TeV", *Submitted to Phys. Rev. Lett.*

[90] CDF Collaboration, D. Acosta *et al.*, "Search for Excited or Exotic Electrons in the $e\gamma$ Channel in $p\bar{p}$ Collisions at $\sqrt{s} = 1.96$ TeV", *To be submitted to Phys. Rev. Lett.*

[91] H. Gerberich and A. Kotwal, "Jet→Photon Fake Rate Measurement using the CPR Detector", CDF note 6368.

[92] CDF Collaboration, D. Acosta *et al.*, "Measurement of charged particle multiplicities in gluon and quark jets in $p\bar{p}$ collisions", *Submitted to Phys. Rev. Lett.*

[93] S. Jadach, Z. Was, "The tau decay library TAUOLA:version 2.4 O(α) QED corrections in $\tau \to \mu e \nu \bar{\nu}$ decay modes", Comp. Phys. Commun. **76** (1993) 361. (CERN TH-6793 preprint)

[94] S. Chuang *et al.*, "Measurement of the Material in the CDF Run II Tracking Volume using high-p_T Electrons", CDF note 6573.

[95] J. Pumplin, D.R. Stump, J. Huston, H.L. Lai, P. Nadolsky, W.K. Tung, "New Generation of Parton Distributions with Uncertainties from Global QCD Analysis." JHEP **07** (2002) 012.

[96] A. D. Martin, R.G. Roberts, W. J. Stirling, R. S. Thorne, "Parton distributions: a new global analysis", Eur. Phys. J. **C4** (1998) 463; A. D. Martin, R.G. Roberts, W. J. Stirling, R. S. Thorne, "Uncertainties of predictions from parton distributions. I: experimental errors", Eur. Phys. J. **C23** (2002) 73.

[97] M. Kirby, Ph.D. thesis, Duke University, Durham, North Carolina, 2004.

[98] CDF and DØ Collaboration, A. Robson, "Diboson Production Cross sections at $\sqrt{s} = 1.96$ TeV", Proceedings of XXXIXth Rencontres de Moriond: QCD and Hadronic Interactions, La Thuile, 28 March - 4 April 2004, CDF note 6994.